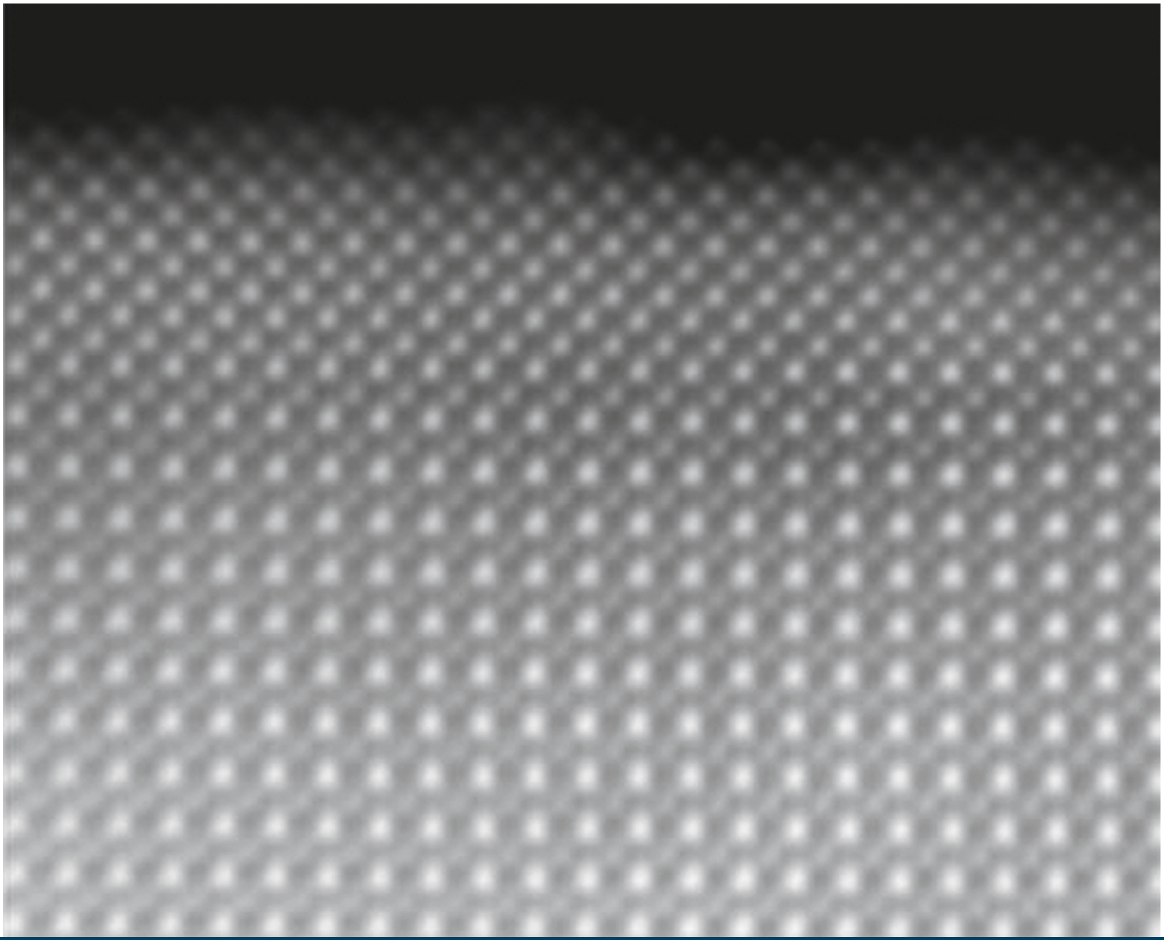

Operando Chemistry and Electronic Structure of Electrode / Ferroelectric Interfaces

Sara Gonzalez

Schlüsseltechnologien / Key Technologies
Band / Volume 175
ISBN 978-3-95806-341-9

Mitglied der Helmholtz-Gemeinschaft

JÜLICH
Forschungszentrum

Schriften des Forschungszentrums Jülich
Reihe Schlüsseltechnologien / Key Technologies Band / Volume 175

Forschungszentrum Jülich GmbH
Peter Grünberg Institut (PGI)
Elektronische Eigenschaften (PGI-6)

Operando Chemistry and Electronic Structure of Electrode / Ferroelectric Interfaces

Sara Gonzalez

Schriften des Forschungszentrums Jülich
Reihe Schlüsseltechnologien / Key Technologies Band / Volume 175

ISSN 1866-1807 ISBN 978-3-95806-341-9

Bibliografische Information der Deutschen Nationalbibliothek.
Die Deutsche Nationalbibliothek verzeichnet diese Publikation in der
Deutschen Nationalbibliografie; detaillierte Bibliografische Daten
sind im Internet über http://dnb.d-nb.de abrufbar.

Herausgeber und Vertrieb: Forschungszentrum Jülich GmbH
Zentralbibliothek, Verlag
52425 Jülich
Tel.: +49 2461 61-5368
Fax: +49 2461 61-6103
zb-publikation@fz-juelich.de
www.fz-juelich.de/zb

Umschlaggestaltung: Grafische Medien, Forschungszentrum Jülich GmbH

Druck: Grafische Medien, Forschungszentrum Jülich GmbH

Schriften des Forschungszentrums Jülich
Reihe Schlüsseltechnologien / Key Technologies, Band / Volume 175

D 464 (Diss. Cotutelle, Univ. Duisburg und Université Paris-Orsay, 2016)

ISSN 1866-1807
ISBN 978-3-95806-341-9

Acknowledgements

Je tiens tout d'abord à remercier Serge PALACIN, chef de l'ancien *Service de Physique Chimie Surfaces et Interfaces*, et François DAVIAUD, chef du *Service de Physique de l'Etat Condensé* du CEA-Saclay pour m'avoir permis de travailler durant trois ans en tant que doctorante dans ces deux laboratoires.

Je suis très reconnaissante envers Nathalie JEDRECY et Lucian PINTILIE pour avoir accepté la position de rapporteurs de thèse et pour les commentaires très utiles qu'ils ont apportés sur mon travail, ainsi que les autres membres de mon comité de défense de thèse : Peter KRATZER et Heiko WENDE.

J'aimerais ensuite remercier mes co-directeurs de thèse, Nick BARRETT et Claus SCHNEIDER, qui m'ont accordé leur confiance, dans un contexte où un financement de thèse n'est pas une chose que l'on accorde à la légère. Nick m'a accompagnée au jour le jour. Je le remercie pour tout ce qu'il m'a appris, et pour la très grande charge de travail qu'il a investi pour me permettre de réaliser mon doctorat dans les meilleures conditions. Bien qu'ayant passé moins de temps au quotidien avec Claus SCHNEIDER, celui-ci a toujours su se rendre disponible pour m'aider.

Je remercie Claire MATHIEU, qui a été présente pour moi tout au long de ces trois années. J'ai toujours pu compter sur elle, notamment dans les moments les plus difficiles. Son accompagnement dans le travail, la formation qu'elle m'a fournie, ses qualités humaines ont été une aide précieuse, et elle est sans aucun doute la personne grâce à laquelle j'ai été jusqu'au bout de cette thèse.

Je remercie Julien RAULT, qui est le premier thésard que j'ai pu voir travailler et le meilleur exemple que j'aurais pu espérer. Même après son départ du CEA, Julien n'a cessé d'être présent et disponible pour m'apporter ses précieux conseils.

Je remercie les membres du groupe LENSIS : Claire et Nick déjà cités ; Christoph LUBIN et Bruno DELOMEZ pour m'avoir autant appris et avoir été toujours disponibles pour répondre à mes (nombreuses) questions ; mes co-thésards, Jelle DIONOT et Guillaume NATAF ; Olivier

COPIE, Daniel GOTTLOB. Je remercie l'ensemble des collègues qui ont rendu le quotidien au laboratoire si agréable : Catherine et Christine pour leur aide quotidienne, Sylvain, Ludo, Bruno L., Jocelyne, Jean-Baptiste, Jacques, Dominique, Fred, François, Sylvain F., Yannick, Fabien, Luc. Un merci particulier à Jean-Louis GRECO qui m'a sauvé de la tragédie lorsque je ne réussissais pas à imprimer ma thèse. Merci aux thésards et stagiaires du labo, et ceux rencontrés au cours des conférences et manips : Qirong, Marina, Vincent, Jérémy, Jérôme, Dana, Avishek, Mattia, Gabrielle, Innocent, David, Héloïse, Debora, Giovanni…

Je remercie l'ensemble des chercheurs et thésards du laboratoire de Jülich PGI-6. Même si mes séjours en Allemagne ont été de courte durée, je me suis toujours sentie la bienvenue grâce à leur accueil. Merci à Christoph, Markus, Marten, Pika, Fabian, Michael, Patrick, Ewa, Timm, Carsten, Lukasz, Roman, Stefan, Margret…

Je remercie les chercheurs avec qui j'ai eu le privilège de pouvoir travailler, Thomas MAROUTIAN, Guillaume AGNUS, Valérie PILLARD et Philippe LECOEUR de l'*Institut d'Electronique Fondamentale* d'Orsay ; Stéphane FUSIL, Manuel BIBES et Agnès BARTHELEMY de l'UMR *CRNS/Thales* ; Brahim DHKIL de l'*Ecole Centrale Paris* ; ainsi que ceux rencontrés sur les lignes de lumière, qui ont rendu le travail en synchrotron plaisant, même quand les nuits étaient courtes et que les résultats peinaient à arriver : Mathieu SILLY (à qui je dois toujours un tableau), Azzedine BENDOUNAN et Fausto SIROTTI de TEMPO, SOLEIL ; Vitaliy FEYER, Onur MENTES et Andrea LOCATELLI d'ELETTRA ; Denis CEOLIN et Jean-Pascal RUEFF de GALAXIES, SOLEIL ; Slavomir NEMSAK et Stefan CRAMM de BESSY.

Je remercie mes professeurs, qui m'ont transmis, tout au long de ma scolarité, l'amour des sciences, et en particulier Jean-Jacques GALLET, qui m'a initiée à la technique de photoémission et au travail en synchrotron lors de mon stage de M1. Il est le premier à m'avoir fait entrer dans cette communauté à laquelle je suis aujourd'hui fière d'appartenir.

Merci encore à ceux qui, durant ces trois dernières années m'ont apporté de précieux conseils sur le milieu de la recherche au cours de longues discussions : Claire, Olivier, Julien, Mathieu, Sylvain, Slavo, Onur, Brahim…

Sur une note plus personelle, j'aimerais remercier mes amis : Lola, la plus ancienne, qui depuis mes 3 ans m'a toujours regardée comme la personne que j'espère un jour devenir ; les Quimiacais : ma cousine Lou, mon cousin Simon, Céline, Marine, François, Jean-Phi ; les Polytech, même s'ils croient encore que je fais de la chimie : Vivien, Marianne, Neji, Maxime, Bertrand, Anyel, Gui, Florence…

Je remercie mes grands-parents, Françoise et Michel, qui m'ont emmenée toute petite découvrir la science au Palais de la découverte et à la Cité des sciences. Merci à eux d'avoir fait le voyage en Allemagne pour assister à ma soutenance de thèse. Merci aussi à mon Abuela qui, j'en suis sûre, aurait elle aussi fait le voyage.

Merci à Quentin. Pour tout.

Je remercie mon grand frère, Victor, qui a commencé cette expérience de la recherche avant moi. Ce n'est pas un hasard si j'ai suivi ses traces durant toutes mes études. Je l'ai toujours admiré.

Je remercie enfin mes parents, qui m'ont donné la possibilité de choisir. Ils m'ont toujours poussée à faire ce que je voulais de ma vie et m'en ont donné tous les moyens. Pour les remercier, mon frère et moi les laissons avec deux enfants chercheurs…

Zusamenfassung

Oxidbasierte Heterostrukturen besitzen Vielfältiges Potential für Anwendungen in der Nanoelektronik, weswegen sie gegenwärtig weitreichend untersucht werden. Unter diesen funktionalen Oxiden befindet sich die Gruppe der Ferroelektrika. Ihre spontane elektrische Polarisation kann mittels eines elektrischen Feldes umgekehrt werden. Wird dieses lokal angelegt, ergibt sich ein neuer Funktionsmechanismus auf dem die Herstellung von permanenten Datenspeichern basieren kann. Das Anlegen eines elektrischen Feldes erfordert eine metallische Elektrode an dem Ferroelektrikum. An der Grenzfläche zwischen den beiden Materialien sind freie Ladungsträger im Metall dafür verantwortlich, dass die Oberflächenladung des Ferroelektrikums abgeschirmt wird, um die Polarisation zu erhalten. Im Falle von Metalloxidelektroden wird die Abschirmung durch ionische Verschiebung erreicht. Der Hauptschauplatz des Abschirmungsprozesses befindet sich somit in beiden Fällen an der Grenzfläche zwischen Elektrode und Ferroelektrikum. Trotz wichtiger theoretischer Entdeckungen sind direkte experimentelle Untersuchungen jedoch rar und das tatsächliche Verhalten an der Grenzfläche entbehrt eines tiefgreifenden Verständnisses. Dies ist jedoch entscheidend für die erfolgreiche Integration von ferroelektrischen Filmen in Speicherzellen mit Abmessungen auf der Nanometerskala.

Als Hauptwerkzeug wurden in dieser Doktorarbeit Techniken der Photoemissionsspektroskopie benutzt. Mit ihnen wurde die verdeckte Grenzfläche im Heteroschichtsystem Elektrode / $BaTiO_3$ / Elektrode untersucht. Dazu wurden zwei Materialien als Deckelektrode ausgewählt: das Metalloxid $SrRuO_3$ und das Metall Co. Mit einer Kombination von operando Hartröntgen-Photoemissionsspektroskopie, Hartröntgen-Photoemissionsmikroskopie und zeitauflösenden Experimenten haben wir die Charakteristika der Grenzfläche und ihre Reaktion auf den elektrischen Polarisationswechsel untersucht. Diese Untersuchungen sind ein neuer Schritt im Verständnis des Verhaltens der Grenzfläche zwischen Elektroden und ferroelektrischem Material, und Einblicke in die elektronischen Eigenschaften, die Kinetik und Alterungserscheinungen konnten gewonnen werden. Durch die Experimente an der Grenze des technisch Machbaren konnten neue Ergebnisse errungen werden, besonders ausgezeichnet durch die Untersuchung von verdeckten Grenzflächen und zeitaufgelösten Umpolvorgängen an funktionierenden Speicherbausteinen.

Abstract

In the past decade, oxide-based heterostructures have been studied extensively as potentially attractive systems for applications in nanoelectronics. Among them, ferroelectric materials raised interest as potential support for those technological applications. Indeed, their spontaneous electric polarization easily switched by applying an electric field makes them a good basis for non-volatile data storage. Switching the polarization requires a metallic contact with an electrode, thus heterostructures of ferroelectric thin films with metallic electrodes have been widely studied. At the interface between those two materials, free charges of the electrode help screening the polarization induced surface charges detrimental to maintaining proper polarization in the ferroelectric thin film. With metallic oxide electrodes, an ionic displacement at the electrode/ferroelectric interface will help the screening, bringing this interface at the core of the screening process. However, despite important theoretical discoveries, direct experimental data is scarce and the behavior of the electrode/ferroelectric interface is still only partially understood. Further understanding is crucial for a proper integration of ferroelectric films in functioning nanometer-sized devices.

In this thesis, photoemission spectroscopy based techniques are used to probe the buried interface of an electrode/$BaTiO_3$/electrode heterostructure, for two different top electrodes: the metallic oxide $SrRuO_3$ and the Co metal. Combining operando hard X-ray photoemission spectroscopy, hard X-ray photoemission electron microscopy and time-resolved experiments, we acquired information on the behavior of the interface and its response to polarization switching. The work presented is a new step towards a complete understanding on the behavior of the interface between electrodes and ferroelectric materials, in the case of electrode / $BaTiO_3$ / electrode heterostructures, in terms of electronic properties, kinetic, and fatigue. The three experiments presented combined state of the art characterization techniques, where the use of hard X-rays and in situ bias application made it possible to resolve the difficult task of probing buried interfaces in working conditions.

Table of contents

Introduction

Ferroelectricity based devices are particularly interesting for a wide range of applications in nanoelectronics. Indeed, their nonlinear nature can be used to make tunable capacitors with a very high permittivity in absolute value, especially when close to the phase transition temperature, making ferroelectric capacitors small in size. Their spontaneous polarization implies a hysteresis effect which can be used as a memory function, and such capacitors are used to make ferroelectric Random Access Memories (RAM) [1]. For thin films, the electric field required to switch the ferroelectric polarization can be achieved with a moderate voltage. Another recent interest is the ferroelectric tunnel junction in which a contact is made up by a nanometer-thick ferroelectric film placed between metal electrodes [2]. The thickness of the ferroelectric layer is low enough to allow tunneling of electrons. The interface effects as well as the depolarization field may lead to a giant electroresistance switching effect.

However, when using thin films a great deal of attention needs to be paid to the interfaces, electrodes and sample quality for devices to work reliably [3]. Switching the polarization in such films requires a metallic contact, raising fundamental issues on the behavior of the interface between the ferroelectric layer and the electrode. This makes it necessary to probe the interface between the two layers, while switching the polarization, to learn about the effect of polarization on the interface properties, such as its barrier height, its thickness etc. Operando experiments, where the polarization is switched *in situ* during measurement are possible for such studies, but pose a technical challenge.

This thesis comprises the study of ferroelectric $BaTiO_3$ perovskite thin films, using photoemission-based techniques. The core of the thesis lies on the study of the chemical and electronic structure of the electrode/ferroelectric interface in heterostructures. Further understanding of this interface is crucial for a proper integration in functioning nanometer-sized devices. The free charges of the electrode help screening the polarization-induced surface charges which are detrimental to maintaining proper polarization in the ferroelectric thin film. With metallic oxide electrodes, an ionic displacement at the electrode/ferroelectric interface will also screen this depolarizaing field.

Operando hard X-ray photoemission spectroscopy was used to probe the polarization-dependent properties of the electrode/ferroelectric interface with metallic oxide $SrRuO_3$ electrodes. *In situ* bias was applied to switch the polarization on a connected $SrRuO_3$/FE/$SrRuO_3$ heterostructure. Special care was taken in designing a connected sample allowing for operando experiments. Time resolved photoemission spectroscopy with *in situ* bias allowed investigation of the dynamical properties of the polarization switching process in such heterostructures. Finally, photoelectron emission microscopy was used to probe Co/$BaTiO_3$ interfaces on smaller scaled capacitors previously switched *ex situ* using Piezo Force Microscopy.

This thesis was done in collaboration between the French Atomic Energy Authority (CEA) in the *Service de Physique de l'Etat Condensé* (SPEC), part of the Institut Rayonnement Matiére de Saclay, and the Peter Grünberg Institut - 6 of the Research Center Jülich (Germany). This work also involved many different collaborations. The development of the micro-fabrication processes and growth of pulsed laser deposition samples have been done jointly with the *Institut d'Electronique Fondamentale* (Orsay, France). The preparation of the electrodes of the heterostructure studied by photoelectron emission spectroscopy, and their polarization switching using Piezo Force Microscopy was done by the group of the *Unité Mixte de Physique CNRS/Thales* (Palaiseau, France). Photoemission spectroscopy with *in situ* bias experiments have been conducted at Synchrotron SOLEIL (Saint-Aubin, France) on the TEMPO and GALAXIES beamlines and Hard X-Ray Photoemission Microscopy experiments have been conducted on the P09 beamline at PETRA III (Hambourg, Germany).

The thesis is divided in five chapters:

- In Chapter 1, the main concepts of ferroelectricity are introduced. The principal properties are illustrated using a typical ferroelectric, the single crystal perovskite oxide $BaTiO_3$. The different theories of polarization (the Modern theory, Landau theory) are described. As the search for new device-like structures brings the desire to reduce sizes to the nm scale, new issues arise, and we explore the concept of screening of the depolarizing field to maintain polarization in thin films. Finally, a state of the art of several considerations on electrode / ferroelectric / electrode heterostructures is presented.

- In Chapter 2, the different experimental characterization techniques are described. First, a selection of classic experimental techniques designed for measuring ferroelectric materials properties are discussed. Then the basics of photoemission spectroscopy are presented, along with hard X-ray photoemission spectroscopy. A description of photoelectron emission microscopy and hard X-ray photoelectron emission microscopy is then given.

- In Chapter 3, the challenge of photoemission spectroscopy while applying a bias on the sample is introduced and our experimental solution is reported, with a thorough description of the samples design and fabrication. Hard X- ray photoemission spectroscopy is then applied on a $SrRuO_3/BaTiO_3/SrRuO_3$ heterostructure. We measure, depending on the polarization state, how the interface chemical and electronic properties are affected, and we use our results along with Transmission Electron Microscopy to estimate the thickness of the affected interface.

- In Chapter 4, we studied a similar $SrRuO_3/BaTiO_3/SrRuO_3$ heterostructure, using time-resolved X-ray photoemission spectroscopy and *in situ* bias, to study the dynamic of the polarization switching process. The sample was exposed to a "Positive Up Negative Down" pulse train while core levels for the $BaTiO_3$ at and below the interface were measured. This study provided a new angle from which the issue of the apparition of fatigue in such devices may also be studied.

- In Chapter 5, we used X-ray photoelectron emission microscopy on a second electrode/ferroelectric interface. Several capacitor of the $Au/Co/BaTiO_3/SrRuO_3$ heterostructure were switched *ex situ*, in order to study the effect of the polarization state on the $Co/BaTiO_3$ interface.

Chapter 1

Introduction to Ferroelectricity and the Electrode / Ferroelectric interface

1.1 General aspects of ferroelectric materials

1.1.1 Ferroelectricity

In 1920, J. Valasek described for the first time the hysteresis behavior of electric polarization in Rochelle Salt ($KNaC_4H_4O_6 \cdot 4H_2O$) [4]. Figure 1.1 shows the hysteresis loop presented in Valasek's study. From this, a new class of material was proposed and called ferroelectric (FE) by analogy with ferromagnetism. Indeed, ferroelectric materials exhibit a typical Polarization - Electric Field loop, with a hysteresis behavior similar in shape to the Magnetization - Magnetic Field loop of ferromagnetic materials.

A FE is an ionic insulator which has at least one low-symmetry phase, with two or more discrete stable states of opposite nonzero macroscopic electric polarization under zero applied electric field, referred to as spontaneous polarization. The other necessary defining property is the possibility to switch between these states with the application of an external electric field. The FE state is linked to the creation of an electric dipole, induced by the relative displacement of the positive and the negative ions. This definition is schematized in Figure 1.2: the free energy of the FE material can be described by a double-well (blue curve). The polarization can be switched from one ground state to the other (red curve), when an electric field of a value high enough is applied. The coercive field, E_C is the minimum value needed to switch the polarization. Again, in similarity to ferromagnetism, FE breaks down above a critical temperature, above which the material becomes paraelectric.

There are two concepts to describe the FE (low symmetry) to paraelectric (high symmetry)

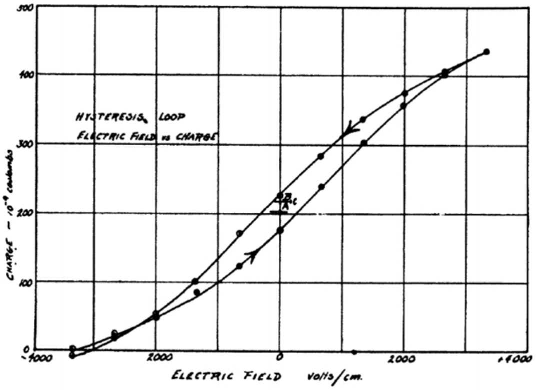

FIGURE 1.1 – *First Polarization - Electric Field loop measured by J. Valasek on Rochelle Salt in 1920 [4].*

phase transition. The order/disorder model [5,6] is a scalar model; and the displacive model [7] is a vector model. In the order/disorder model, with increasing temperature, ions progressively acquire enough kinetic energy to hop back and forth between the two sides of the potential double well, so their average position is midway between the two polar states in the high temperature disorderd phase. In the displacive model, with increasing temperature, the free energy becomes a single well with a minimum for zero polarization (see Figure 1.2 b)). The material is then in a paraelectric state. It follows that a ferroelectric phase must therefore have a non-centrosymmetric structure. In a centrosymmetric structure, restoring forces indeed cancel the relative ionic displacements [8].

1.1.2 The modern theory of polarization

The definition of the polarization states that for a certain volume element in the material ΔV, which carries a dipole moment Δp, we define the polarization density P as:

$$P = \frac{\Delta p}{\Delta V} \tag{1.1}$$

In general, the dipole moment Δp changes from point to point within the dielectric. Hence, the polarization density P of a dielectric inside an infinitesimal volume dV with an infinitesimal dipole moment dp is:

$$P = \frac{dp}{dV} \tag{1.2}$$

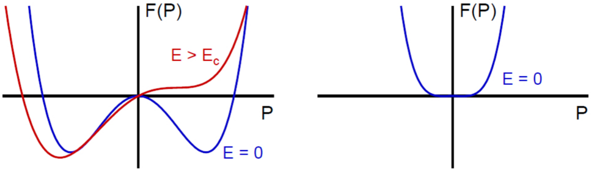

FIGURE 1.2 – *a) Free energy double-well of a ferroelectric system as a function of polarization. The blue curve is for zero external electric field: both polarization states have the same energy. The red curve is when an electric field stronger than the coercive field* E_C *is applied on the material, promoting one state over the other. b) Free energy of a paraelectric system.*

This traditional definition of polarization as a quantity describing the integrated contributions of local dipoles is no longer valid when dealing with finite crystalline solids. Indeed in the case of finite structures, changes in the surface would modify the total polarization of the sample, whereas the polarization of the bulk would remain the same.

In the early 1990s, R. Resta [9], and King-Smith, Vanderbilt [10], developed a solution to tackle this fundamental issue on the microscopic scale, known as the modern theory of polarization. In this approach, one focuses on the difference in polarization between two states of the crystal that can be connected by an adiabatic process. This calls for the need to introduce a parameter, λ, representing a dimensionless adiabatic time, which varies continuously, from 0 at the initial state, to 1 at the final state. The transition from initial to final state is achieved by slow sublattice displacements, strain or electric fields for instance. The change in polarization can therefore be given by the equation 1.3:

$$\Delta P = \int_0^1 d\lambda \frac{dP}{d\lambda} \tag{1.3}$$

where the quantity $dP/d\lambda$ is the transient current carried by electrons and nuclei.

Here, the resulting phase (from which one extracts the current, hence the polarization difference) of the Bloch wavefunctions when going from $\lambda = 0$ to $\lambda = 1$ is expressed in the more general framework of Berry phases [11]. Thus, the modern theory of polarization is often referred as the Berry-phase theory of polarization. This model allows for *ab-initio* calculation of experimentally accessible quantities such as piezoelectric coefficients, spontaneous polarization and dynamical charges. However, this method still has limitations common to every *ab-initio* technique (the limited-size of the numerical cluster, the impossibility to monitor non-equilibrium phenomena) preventing it from accurately describing realistic FE systems, *i.e.* on the macroscopic scale.

A second theory, the Landau theory, is used to analyze the behavior of a system near a phase transition involving a change of symmetry (which is made impossible using the previous model by the incapacity to monitor non-equilibrium phenomena). The Landau theory describes the transition from one phase to another of different symmetry. The phases are characterized by an order parameter (polarization in the case of FE materials) which is zero in the high-symmetry phase, and continuously changes to a finite value in the low-symmetry phase. However, this methodology fails to describe systems of reduced size when the averaging of the order parameter is no longer possible.

Both theories are needed to describe real system in the most accurate way. The use of first-principles based effective Hamiltonian techniques allows describing systems at the intermediate scale. They have been widely used on FE materials to investigate domain behavior and temperature dependence of the FE properties [12]. In a first step, Landau theory is used as a conceptual base, to find the relevant degrees of freedom of the system. Then, the system energy is described via an effective Hamiltonian, with coefficients calculated using first-principle calculations. The final step is to minimize the total energy of the system as a function of the degrees of freedom using the Monte-Carlo methodology [13]. This framework produced excellent results on domain patterns [14] or phase transition [15] in FE systems, even when the system size is reduced.

1.1.3 The case of $BaTiO_3$

$BaTiO_3$ is a prototypical FE material. Among the many discovered ones, $BaTiO_3$ is the first simple oxide in which ferroelectricity has been observed. In 1944, Wul and Goldman [16] found that barium titanate ceramics exhibited a high dielectric permittivity varying strongly with temperature and peaking at a rather high maximum at T=400 K. Up to now, it has been the most exhaustively studied dielectric ceramic together with $PbTiO_3$ and $PbZrO_3$. As a prototypical FE, it will be at the core of this thesis.

Barium titanate is an oxide of chemical formula $BaTiO_3$ in which barium, titanium and oxygen atoms are arranged in a perovskite crystalline structure. This structure is represented in figure 1.3. The conventional cell is a face-centered cubic (fcc) cell, depicted in the last part of the Figure. The perovskite structure is adopted by many oxides having the chemical formula ABO_3 where the A-type cation is the heavy atom, here the barium, and the B-type cation is the light atom, here the titanium. These oxides exhibit many interesting properties such as ferroelectricity ($BaTiO_3$, $PbTiO_3$), pyroelectricity, colossal magnetoresistance (doped $LaMnO_3$), or multiferroicity ($BiFeO_3$, $EuTiO_3$).

The perovskite cubic structure depicted in figure 1.3 is described by a cubic lattice parameter

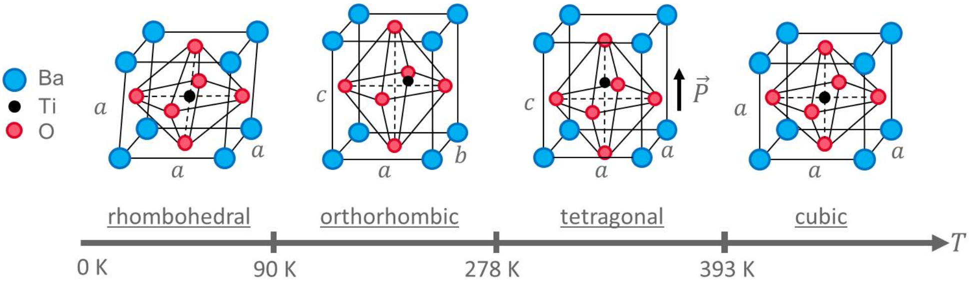

FIGURE 1.3 – *$BaTiO_3$ perosvkite structure in the rhombohedral, orthorhombic, tetragonal, and cubic phase depending on the temperature T.*

$a = 3.996$ Å, with the Ti^{4+} ion at the center of a cube with Ba^{2+} ions at the corners, and O^{2+} ions at the center of the faces. In a unit cell, the oxygen sublattice forms an octahedron with a titanium ion at its center. This phase is the only structural phase of $BaTiO_3$ which is paraelectric. The centrosymmetric structure of the cubic phase can be assigned to the fact that this phase takes place at relatively high temperature ($T_c = 393$ K), where thermal excitations and atomic motions are favored. Thus, the position of the central Ti ions is averaged to the actual center of a cubic unit cell. By contrast, the lower symmetry tetragonal phase, shown in figure 1.3, has a unit cell of lattice parameters $a = 3.995$ Åand $c = 4.034$ Å [17]. $BaTiO_3$ exhibits three non-centrosymmetric FE phases: rhombohedral (up to 183 K), orthorhombic (183 K to 278 K) and tetragonal (278 K to 393 K) [17]. In these low-symmetry phases, the titanium atom is displaced from the center of the cube towards a preferential direction, called the polar axis. In the case depicted in the tetragonal structure presented Figure 1.3, the polar axis lies along the vertical direction, on the axis named c. The resulting asymmetric charge distribution induces a local dipole moment, which is the microscopic origin of the ferroelectricity in the material.

Due to long-range Coulomb interactions between the dipole moments, $BaTiO_3$ exhibits a macroscopic polarization along the polar axis. Dipoles rearrange themselves to minimize the stray field energy as a function of temperature, strain, crystallographic defects, adsorbates and history of the sample, to form FE domains wherein the polarization is in the same direction. Experimentally, these domains can be imaged by optical microscopy, photoelectron emission microscopy (see section 2.3) or Piezoresponse Force Microscopy (PFM, see section 2.1). The $BaTiO_3$ is of great interest as it exhibits ferroelectricity at room temperature, with a naturally stable tetragonal phase. Above the Curie temperature ($Tc = 393$ K), $BaTiO_3$ becomes cubic and therefore paraelectric.

In 1960, W. Cochran developed a description of ferroelectricity in terms of the vibrational modes of a crystal lattice [7]. In this model he considers a linear chain of O - Ti - O atoms along the polar axis in $BaTiO_3$. It is possible to describe a small displacement x of the titanium atom from its equilibrium position in the framework of classical Newtonian physics, as a function of long range Coulomb forces A, and short-range repulsion R:

$$\mu \frac{\partial^2 x}{\partial^2 T} = -R \cdot x + A \cdot x \tag{1.4}$$

where R describes the restoring, stabilizing force due to the short-range potential interaction between the ions and A describes the destabilizing force due to the long range Coulomb forces (dipole-dipole coupling). μ is the reduced mass of the Ti - O unit.

The existence of ferroelectricity relies on the competition between the pro-ferroelectric forces (A) and the paraelectric forces (R). In the high-symmetry, *i.e.* the high temperature phase, the short-range forces R are dominant over the long-range forces: the system is paraelectric. With decreasing temperature (hence increasing A), the long-range forces progressively supersede over the short-range ones. Below the transition temperature (where the transverse optical phonon goes to zero), long-range forces become dominant and the system becomes ferroelectric. At the transition temperature, the competing forces acting on the ions are balanced.

The Cochran model [7] is a displacive theory model: titanium ions are considered to progressively displace from a centered position to the off-center polar positions when crossing the transition temperature. In the order-disorder theory developed by R. Comes [5] and B. Ravel [6], titanium is always displaced in one of the eight possible off-center positions along the <111> directions. Occupancy of the eight possible sites leads to the different phases. When the temperature is higher than the Curie temperature, every site is equivalent. Therefore, the mean polarization is zero and $BaTiO_3$ is paraelectric. With decreasing temperature, the site occupancy probabilities change, leading to lower symmetry phases. In the particular case of $BaTiO_3$, it seems that both models have a role, and both theories have been used in Ref. [18] by E. Stern.

In this thesis, we study ferroelectricity in a $BaTiO_3$ based capacitor. $BaTiO_3$ will be referred to as BTO for short. The geometry of the studied heterostructures leads us to focus on out-of-plane polarization, *i.e.* when the Ti atom is displaced towards or away from the surface. In-plane polarization along a-type axes also exists and is often observed in BTO systems. In the case of the out-of-plane polarization, along the c axis, the stacking of non centro-symmetric unit cells leads to a macroscopic polarization along the c axis called polar axis.

1.2 Depolarizing field and screening

1.2.1 Depolarizing field

In the previous section, one key feature of all real FE system was not considered: the boundary conditions. In thin film systems, if the FE polarization has an out-of-plane component, it induces a surface charge density at the surface, generating a depolarizing field. The latter can attenuate or even suppress ferroelectricity. The schematic of Figure 1.4 shows the relationship between the polarization and the depolarizing field.

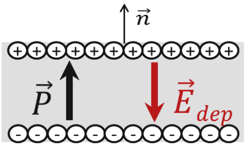

FIGURE 1.4 – *Schematic of the depolarizing field E_{dep} inside a FE material, attenuating or destabilizing the FE polarization P. These two vectors are antiparallel and parallel to the surface normal.*

If a FE polarization (P) arises in the out-of-plane direction (parallel to $\vec{n}$, the surface normal vector) of the slab, it will induce a surface charge density (σ_{pol}) where:

$$\sigma_{pol} = \vec{P} \cdot \vec{n} \tag{1.5}$$

These charges generate an electric field E_{dep} called depolarizing field which acts against the FE polarization (see figure 1.4):

$$E_{dep} = -\frac{P}{\varepsilon\varepsilon_0} \tag{1.6}$$

where ε is the dielectric constant of the slab.

The depolarizaing field E_{dep} is proportional to the reciprocal of the film's thickness. The electrical boundary condition, *i.e.* the screening of the surface polarization charges, is a key parameter in maintaining the ferroelectricity of the system, and an unscreened film means a destabilization of its polarization. Changes in boundary conditions can for example induce a FE to paraelectric transition.

1.2.2 Screening mechanisms

In order to stabilize the FE polarization in a finite system, in particular in configurations where the polarization is perpendicular to the surface, the depolarizing field E_{dep} must be at least partially screened, *i.e.* compensated by an opposite macroscopic electric field. In real systems, E_{dep} is screened by a macroscopic electric field that has various possible origins. Several screening mechanisms exist and are presented schematically on figure 1.5. They can be divided in two groups: intrinsic, which includes defects and domain ordering, and extrinsic.

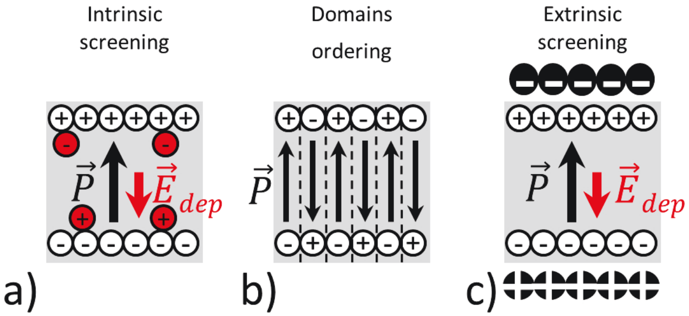

FIGURE 1.5 – *Different mechanisms for screening the polarization-induced charges. a) Intrinsic screening by defects b) Domain ordering and c) Extrinsic screening mechanisms.*

- Intrinsic screening:

  · Defects:
  Charge compensation can arise from defects and impurities inside the material itself. Vacancies or dopants inside a FE material will change the stoichiometry and lead to an excess of charge carriers that are available to screen the polarization bound charge. This screening is schematically described in figure 1.5 a). Among all the defects and impurities that can be present in oxides and have an effect on ferroelectricity [19,20], oxygen vacancies are the most studied. Oxygen vacancies act as donor defects to compensate the polarization bound charge [21,22]. For example, in BTO, the oxygen vacancies created by vacuum annealing generate free electrons according to $O_O \rightarrow V_{O^{\bullet\bullet}} + \frac{1}{2}O_2 + 2e^-$. The free carriers screen the positive polarization-induced charges, and may favor one FE polarization over the other, whereas the positive oxygen vacancies may screen negative polarization charges. Direct change of oxygen

vacancy concentration can stabilize out-of-plane, inwards pointing polarization (see Ref. [23] in reduced BTO, Ref. [24] in $PbTiO_3$). The LENSIS group reported experimental evidences of ferroelectric-paraelectric transition induced by doping by oxygen vacancies [25]. Since FE displacements are stabilized by long range interactions, the presence of free charge carriers (electrons or holes) in FE materials is expected to destabilize ferroelectricity. However, vacancies and impurities have been observed to induce conductivity without losing ferroelectricity [20, 26, 27].

- Domain ordering:
  A second intrinsic screening mechanism found in FE materials is domain ordering. A "domain"İis a region of the material in which the FE polarization is uniform. The boundaries between such regions are called domain walls. Polarization can naturally form domain patterns to reduce the total energy of the system. Figure 1.5 b) shows a schematic of one type of domain ordering in a ferroelectric film. Polarization organizes itself in several domains, which can be of few micrometers to few nanometers. In this case the separations between two domains of different polarization are 180°domain walls, so the polarization in an adjacent domain is antiparallel to its neighbor. The macroscopic electric field created by each domain screens the depolarizing field in the adjacent domains. Domain ordering at the surface of BTO has been reported in several studies [28–30].

- Extrinsic screening:
  Extrinsic screening can originate from polar molecules adsorbed on the surface of the FE material, free charges in electrodes, or an externally applied field.

  - Adsorbates:
    Extrinsic screening can be ensured by the adsorption of molecules providing surface charge compensation [24, 31, 32], as shown schematically in figure 1.5 c). Kalinin *et al.* used local-probe microscopy techniques, such as scanning surface potential microscopy (SSPM) and piezo-response force microscopy (PFM), to map the potential at FE surfaces. Evidence of complete screening of the bound charges from adsorbates was reported [33]. This study also showed that the surface charge can be fully reversed by a large quantity of adsorbates.

  - Electrodes:
    Metallic or semi-conductor electrodes grown on the FE surface in short-circuit condi-

tions can provide charge carriers to screen the polarization charge density. Figure 1.6 schematizes this situation.

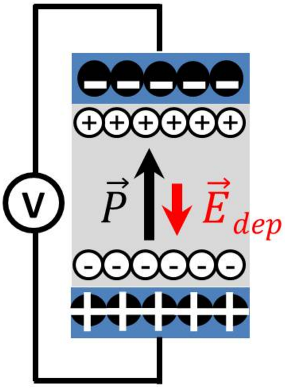

FIGURE 1.6 – *Schematic of an electrode/FE/electrode structure. The electrodes are in blue and the FE material in light grey. The fixed charges, induced by the FE polarization P, are (imperfectly) screened by free charge carriers.*

The free charges brought by the metallic electrodes (in blue) will accumulate at the interface with the FE material, screening at least partially the depolarizing field (red arrow). This allows maintaining polarization (black arrow) inside of the material. At the metal/FE interface, a region of space charge is created in the metal which generates a macroscopic electric field across the FE, thus screening the depolarizing field. This screening mechanism is complex and depends on the metal/FE interface which is characterized by a finite screening length, interface chemistry and strain. To integrate FE films in functioning devices, the presence of electrodes is indispensable to switch the polarization. This screening mechanism is thus of great interest.

1.2.3 Screening length

The screening length is a key parameter in the description of this last screening mechanism. Two hypothetical boundary conditions are often used for modeling or calculations:

- In the short-circuit boundary conditions, the FE charges are perfectly screened. The depolarizing field is zero.
- In the open-circuit boundary conditions, the FE charges are not screened at all. The depolarizing field is maximal.

In a real system, the screening mechanism is imperfect, with screening charges spatially distributed away from the surface of the ferroelectric, leading to finite interface dipole. Considering identical metallic electrodes at both surfaces of the FE slab of thickness d, the total voltage drop is:

$$\Delta V = 2\frac{\lambda_{eff}}{\varepsilon_0}|P| \tag{1.7}$$

where λ_{eff} is the effective screening length. λ_{eff} is a measurement of the displacement of the screening charge from the FE surface. It models the distance over which the polarization charges are screened. In the case of short-circuited conditions (*i.e.* both metallic electrodes are at equipotential), the equation 1.6 gives for the depolarizing field:

$$E_{dep} = -2\frac{\lambda_{eff}}{d\varepsilon_0}P \tag{1.8}$$

The schematic of Figure 1.7 shows the relationship between the different parameters of these equations.

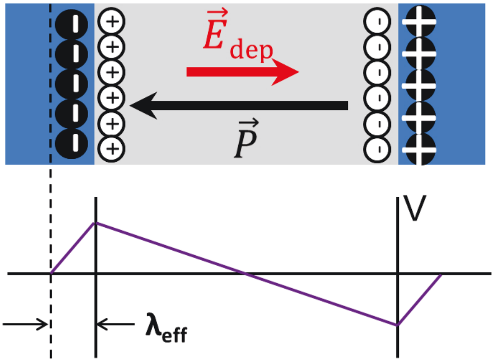

FIGURE 1.7 – *Schematic of an electrode/ferroelectric/electrode structure (top). The fixed charges, induced by the FE polarization P, are imperfectly screened by free charge from the metallic electrode over the effective screening length λ_{eff}. The resulting electrostatic potential V (bottom), or equivalently the depolarizing field E_{dep}, acts against P.*

A small screening length means good screening by the electrodes, therefore a weak depolarizing field, and a better FE stability. This screening length can be estimated from experimental results [34] or obtained from *ab-initio* calculations using electrode/FE supercells [35, 36]. Recently, a theoretical framework emerged from effective Hamiltonian methods. Ponomareva *et al.* used a screening factor to model the efficiency of screening [37]. This model has been successfully used in many FE systems [38, 39] with the advantages of effective Hamiltonian framework (large clusters, temperature dependence).

1.3 $SrRuO_3$, a metallic oxide electrode.

In 1999, $SrRuO_3$, designated SRO for short, appeared on the International Technology Roadmap for Semiconductors in the context of stacked-capacitor dynamic random access memory. As recognized early on by Eom *et al.* (1992) [40], metallic SRO is a good candidate because of its perfect registry with several substrate materials and its nearly ideal growth mode. In their work, Schlom *et al.* [41] present the lattice constant of several perovskite or perovskite-related phases along with several substrate ones. This comparison is schematically presented in figure 1.8.

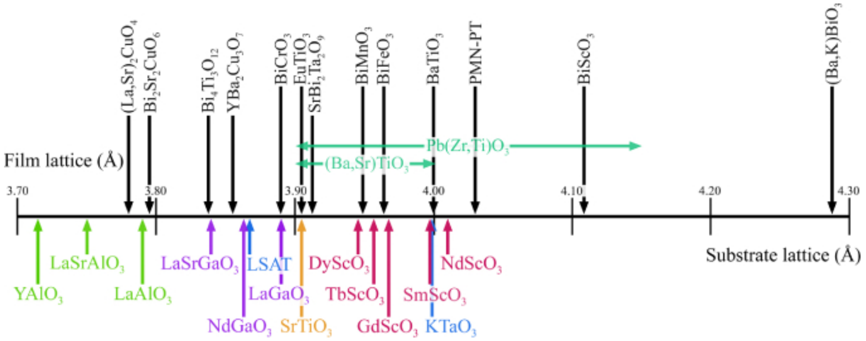

FIGURE 1.8 – *A number line showing the pseudotetragonal or pseudocubic a-axis lattice constants in angstroms of some perovskites and perovskite-related phases of current interest (above the number line) and of some of the perovskite and perovskite-related substrates that are available commercially (below the number line). From ref [41].*

The work shows that the $SrTiO_3$ substrate presents a good match with the lattices of both the BTO and the SRO. This results in single crystalline, atomically smooth thin films. The most prominent example has been the successful use of SRO in FE perovskite capacitor structures, as first demonstrated by Eom *et al.* (1993) [42] in the case of a $Pb(Zr_{0.52}Ti_{0.48})O_3$ structure. Numerous oxides have been used in combination with SRO electrodes (ferroelectrics such as $BiFeO_3$ [43], dielectrics [44], and other materials [45]).

a) Crystalline structure

SRO is the infinite-layer material ($n = \infty$) in the series of ruthenates $Sr_{n+1}Ru_nO_{3n+1}$. Similarly to many ABO_3 perovskite compounds (such as BTO for instance, as previously explained in section 1.1.3), SRO exhibits orthorhombic structure at room temperature, as depicted in Figure 1.9.

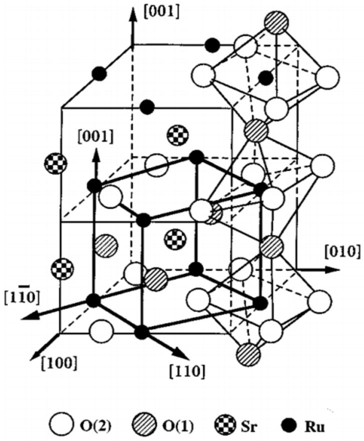

FIGURE 1.9 – *Schematic view of the orthorhombic unit cell of SRO. From Gan et al. [46].*

An orthorhombic cell is typically observed in ABO$_3$ perovskites when the A-O bond length is less than twice the B-O length, which results in rotations of the BO$_6$ octahedra. In SRO, the RuO$_6$ octahedral rotation produces a distorted, pseudocubic perovskite structure, with lattice parameters a = 5.5670 Å, b = 5.5304 Å, and c = 7.8446 Å [47]; the pseudocubic lattice constant is a = 3.93 Å. The orthorhombic phase can be visualized by rotation of BO$_6$ (RuO$_6$) octahedra counterclockwise about the [010] and [001] directions and clockwise rotation about the [100] direction of an ABO$_3$ cubic perovskite (pseudocubic with a = 3.93 Å); these directions become inequivalent upon rotation. With increasing temperature, the degree of the orthorhombic distortion decreases, and the structure transforms to higher-symmetry perovskite structures.

As described by Kennedy and Hunter in 1998 [48], around 550°C, the orthorhombic structure transforms into a tetragonal structure (with space group *I4/mcm*). In this tetragonal unit cell, the RuO$_6$ octahedra are rotated only about the [001] SRO direction. Going to higher temperatures around 680°C, tetragonal SRO transforms into a cubic structure (with a standard perovskite space group *Pm3m*), where the RuO$_6$ octahedra are not rotated. These phase transformations are illustrated in Figure 1.10. The structural transition temperatures are influenced by strain, and, hence, in the case of epitaxial thin films, they depend on the substrate material.

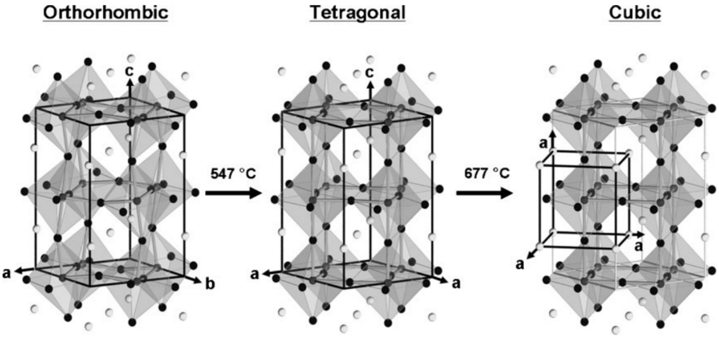

FIGURE 1.10 – *A sequence of phase transitions of unstrained bulk SRO from orthorhombic to tetragonal and then cubic symmetry at 547°Cand 677°C, respectively. The unit cell of the orthorhombic SRO consists of four formula units of the ideal cubic perovskite structure. The atoms of Ru occupy high-symmetry positions with respect to the orthorhombic shape of the cell. The atoms of O and Sr are displaced from their high-symmetry positions due to the octahedral tilting. The tetragonal SRO is a one-tilt system, where* RuO_6 *octahedra are rotated only about the [001] direction. The cube corresponds to the unit cell of each SRO form. Gray, black, and white balls represent Ru, O, and Sr atoms, respectively. From Choi et al. [49].*

Moreover, it is important that the electrodes grow epitaxially on both the BTO and the STO substrate. As the SRO has a small mismatch with BTO and STO, it will epitaxially grow on them, with little to no interfacial defects [50]. It has already been shown that SRO grows epitaxially on these materials [51].

b) Electronic properties

SRO is often used as an electrode. There are several reasons for this. It is one of the few complex oxides that are metallic without external doping. Indeed several oxides, such as $SrTiO_3$, need to be doped with metals such as niobium to be conducting. SRO has a good lattice match with a wide variety of functional oxides and therefore is relatively easy to incorporate in heterostructures. Thus, thin films of SRO have drawn wide interest as a conducting layer in epitaxial multilayered structures of complex oxides, in particular, as electrodes in oxide electronics.

The basic electronic structure of SRO can be obtained by developing its energy level structure from atomic orbitals, as depicted schematically in Figure 1.11.

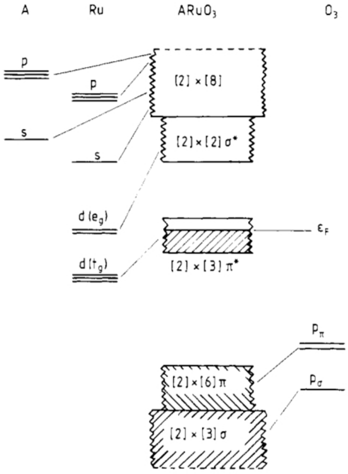

FIGURE 1.11 – *Schematic low-spin one-electron energy level diagram for a perovskite ruthenate* $ARuO_3$*. The degeneracies of the bands indicated in square brackets are multiplied by 2 to allow spin degeneracy. The correlation lines indicate the dominant atomic parentage of the band states. From Cox et al. [52].*

As the diagram shows, the fivefold degeneracy of the Ru *4d* orbitals is broken into two groups by the octahedral crystal environment, raising the energy of the *4d*(e_g) levels above the *4d*(t_{2g}) levels. When the three *4d*(t_{2g}) levels are filled with four electrons according to Hund's rules, the resulting spin state is $S = 1$. These simple arguments allow one to anticipate the band structure. Early first-principle band structure calculations for SRO were published by Allen *et al.* [53] and by Singh *et al.* [54]. Both calculations correctly predicted that SRO is an itinerant ferromagnet. Figure 1.12 shows the spin-resolved density of states (DOS) from Allen *et al.* [53], which indicates a Stoner splitting of nearly 1 eV between the majority and minority bands, together with a significant DOS for both at the Fermi level. As expected from the figure 1.11, the states near the Fermi level have predominantly Ru *4d*(t2g) and O *2p* character.

Figure 1.13 shows the resistivity of SRO as a function of temperature. The drop in resistivity at T = 160 K reflects the ferromagnetic transition. At higher temperatures the resistivity continues to rise, into becoming a "bad" metal, *i.e.* badly conducting [53, 55]. In the case of our study, this could be an issue as the SRO used as an electrode needs to be conducting to apply a bias on the FE BTO. We thus avoided any over-heating of

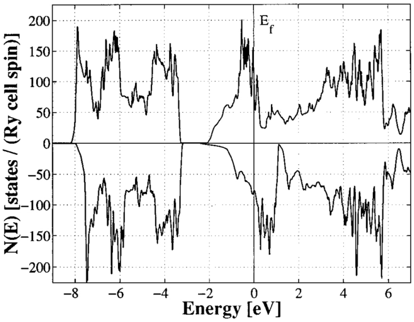

FIGURE 1.12 – *Electronic density of states of ferromagnetic SRO. Majority spin is plotted upward, minority spin downward. The cell contains four formula units. From Allen et al. [53].*

the samples. At low temperature, conventional metallic behavior is observed.

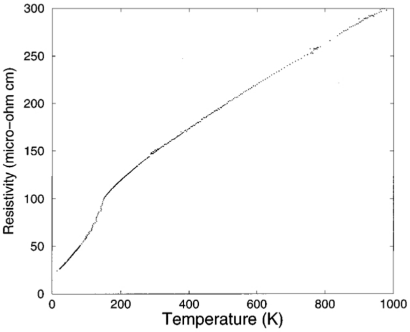

FIGURE 1.13 – *Resistivity vs temperature for SRO. From Allen et al. [53].*

1.4 Metal / ferroelectric interface - state of the art

The integration of FE materials in electronic devices requires two electrodes for application of a bias to switch the polarization state. One issue is that the screening provided by electrodes is sometimes less effective than the one provided by external adsorbates on the FE or by natural rearrangement of domains. To properly maintain the ferroelectricity, the nature and characteristic of the electrodes have to be carefully chosen, in order to provide good enough screening of the depolarizing field, along with efficiently playing their role as conductor for the electrical contact between the material and the circuit. A second issue, is the need to properly control the interface chemistry, in order to maintain the desired symmetry between the two polarization states.

Metallic electrodes under short-circuit conditions should provide a mechanism for compensation of the depolarization field that acts to stabilize the uniformly polarized state. However surprisingly, with pure metal electrodes, the screening is often imperfect. Indeed as the FE films get thinner, the residual field in the ferroelectric due to the surface-dipole density at the ferroelectric/electrode interface grows [35, 56] resulting in a renormalization of the coercive field [3], and ultimately a possible destabilization of ferroelectricity in the thinnest films. Thus, researchers have started to focus on the possibility of other electrodes such as semi-conducting oxides to provide better screening. These materials have been found to be more efficient than pure metal electrodes.

1.4.1 Ferroelectricity in ultrathin films

Promising new properties appear when reducing dimensions of thin films, dots, wires or clusters to the nanometric scale. The physics at this scale is of great interest since quantum-related phenomena can be dominant. The potential industrial applications in the long-standing quest for nanotechnology, high-storage density or low-consuming devices are very promising. Recently, the growth of strained, nanometer-thick, oxide films has met some significant developments [57, 58] ; therefore a lot of research in material science has focused on oxide multilayers. In 2008, D. Schlom wrote in a review of oxide films:

> *"Oxides exhibit the full spectrum of electronic, optical, and magnetic behavior: insulating, semiconducting, metallic, superconducting, ferroelectric, pyroelectric, piezoelectric, ferromagnetic, multiferroic, and nonlinear optical effects are all possessed by structurally compatible oxides" [58].*

The use of oxide heterostructures may thus allow one to taylor an extremely wide range of physical properties, especially when strain-engineering is used [41, 59]. In the field of FE based electronics, downscaling has also driven research towards novel nanoscale systems [60, 61], for instance with the development of FE tunnel junctions. It was demonstrated that in the case of ultrathin, or tunneling (thickness < 5 nm) FE films, these devices can exhibit a high FE polarization magnitude [62]. This raises the question on how the polarization behaves when decreasing the thickness of the FE film, how the polarization magnitude changes and how the energy of the thin film accommodates for the increasing depolarizing field.

Based on early experiments, it was believed that the ferroelectricity vanishes below a critical thickness of severral microns. Then, studies suggested that it disappeared below a few tens of nanometers, due to the depolarizing field produced by polarization charges on the two surfaces of the FE film [63]. A study by Garcia *et al.* on FE tunnel junctions has lowered this thickness limit in BTO to only one nanometers [64].

In theoretical studies, significant progress was made in the field. Using *ab-initio* methods, Junquera and Ghosez [35] studied the critical thickness of BTO thin films to maintain ferroelectricity and paved the way for numerous simulations on real device-like heterostructures of ferroelectrics thin films between two electrodes [36, 65, 66], free-standing layers under an applied electrical field [67] or domain walls [68]. Using Monte-Carlo methods, complementary information was obtained by simulating systems with realistic size and subjected to adjustable boundary conditions. They predict different domain ordering in thin films subjected to increasing depolarizing field [69] or the evolution of the Curie temperature with thickness [70].

In experimental studies, measuring the polarization itself is made very difficult in devices of reduced size [71]. Piezoresponse Force Microscopy (see section 2.1) can be used to prove the existence of polarization in a very thin film, and thus was often used to probe and determine the critical thickness for several types of films [72–75]. In tunnel junctions however, the leakage current is too high and prevents one from accessing the value of the switching current [76]. Studies thus often rely on other properties of the FE film that are more easily measured and that are linked to the polarization (i.e. that will be modified accordingly to any change in the polarization). For instance, Lichtensteiger *et al.* measured the tetragonality of the film (c/a ratio) in a $PbTiO_3$ thin film using X-ray diffraction, as this parameter is directly related to the Ti off centering, i.e. the polarization [77]. A second example is the study by Maksymovych *et al.* of the out-of-plane piezoresponse of $BiFeO_3$ thin films, expressing this response as a function of the polarization [78]. In perovskite FE oxides, ferroelectricity was observed in nanometer thick films [64, 77, 79]. These experimental results are consistent with the first-principles calculations predicting that the critical thickness for ferroelectricity in perovskite films can be as small as a few lattice parameters [35].

In the theoretical work on the thickness dependence of ferroelectricity carried out by Junquera and Ghosez [35] already cited, the role of the electrode material used was also investigated. The most notable result of this work is shown in Figure 1.14, where the evolution of the energy is measured as a function of the soft-mode distortion, and in compared to calculations on metal-oxide systems [36, 80]. First-principles results (symbols) and electrostatic model results (lines) are shown for different thicknesses of the FE thin film.

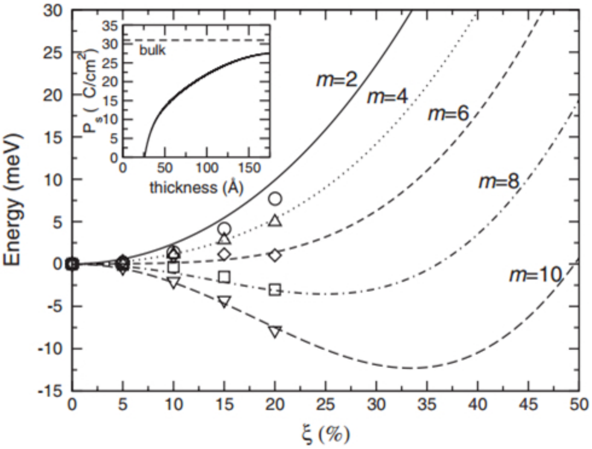

FIGURE 1.14 – *Evolution of the energy as a function of the soft-mode distortion ξ. The magnitude of ξ is reported as a percentage of the bulk soft-mode displacements of BTO atoms ($\xi = 1$ corresponds to the distortion of the bulk tetragonal ferroelectric phase). From Ref [35].*

Other work, carried out for instance by Kohlstedt *et al.* [81] or Nagarajan *et al.* [51] also investigated the role of the electrode. It was predicted that the chemistry of the ferroelectric-metal interfaces strongly influences the FE state through the formation of intrinsic dipole moments at the interfaces, as determined by the atomic species and interfacial metal-oxide bonds. For some interfaces, these dipole moments are switchable and may enhance the FE instability of the thin film, which is interesting for engineering the electrical properties of thin-film devices [36]. For other interfaces, however, the effect of interface bonding is detrimental and leads to the freezing of polar displacements in the interfacial region, thus resulting in a ferroelectrically inactive layer near the interface [82]. In electrode/FE/electrode heterostructures, a skewing of the valence and conduction bands in the ferroelectric at the interface with the electrode has also been reported [65]. This modification of the bands structure allow us to access, and even control the electronic properties of such heterostructures.

1.4.2 Ionic displacement (rumpling) at the electrode/ferroelectric interface

It was demonstrated that in addition to the screening associated with free charges in the metal electrodes [63] there is an important contribution resulting from ionic screening if electrodes are metallic oxides, such as $SrRuO_3$ [83]. This screening results in an ionic displacement which is called rumpling. It is a common behavior of oxides. In the case of BTO, rumpling is present in the bulk due to polarization induced displacements, but will be different at the surface of the film, and thus at the interface with any other film. The electrode/BTO interface of a device-like heterostructure will thus be impacted by this phenomenum.

In a crystalline bulk, the equilibrium positions of the atoms result from a balance between the forces generated by all their neighbors. At the surface, the atoms have a different environment: some neighbors are missing with respect to the bulk. Thus, the atoms relax to equilibrium positions that differ from the bulk ones. The new equilibrium positions of the surface atoms involve displacements perpendicular to the surface. The rumpling is defined by the relative displacements, normal to the surface, of the cations with respect to the anions. At the oxide surface, it usually consists of anions displaced outwards with respect to cations. Such displacements were measured in $SrTiO_3$ oxide by both reflection high-energy electron diffraction (RHEED) [84] and low-energy electron diffraction (LEED) [85]. On BTO surfaces, first-principles calculations [60, 86, 87] predict similar results. The relative displacements induced by the rumpling correspond to polar displacements, related to FE polarization at the surface. The average displacement (normal to the surface) of the cations and anions of a given plane defines the surface relaxation. The observed tendency is a reduction of interplanar spacing, at least between the surface layer and the first surface underlayer [88]. The further away from the surface atomic layer, the weaker this effect, as the properties tend to approach those of the bulk. The surface of a FE BTO(001) single crystal was studied by Pancotti [89] using synchrotron radiation induced X-ray photoelectron diffraction (XPD). The rumpling and interlayer relaxation was determined by comparing XPD results on the Ba *4d*, Ti *2p*, and O *1s* orbitals with multiple scattering simulations for the different polarization states. The results are presented in Figure 1.15. As we can see, the rumpling corresponding to the FE distortion increases as we go from the surface of the BTO towards the bulk, whyle the oxygen atoms are relaxing to their original position.

Thus, free charges from electrodes and fixed charges redistribution via rumpling in the FE or/and in the electrode may combine to screen the depolarizing field and help maintaining the

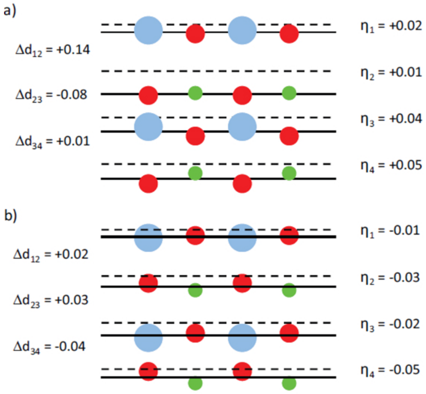

FIGURE 1.15 – *Relaxation and rumpling for the first four atomic layers in a) $P^{\uparrow}$ and b) $P^{\downarrow}$ domains obtained from the Ba 4d XPD. The original and relaxed atomic layer positions are indicated by dotted and solid lines, respectively. The atomic displacements are multiplied by 10 for clarity. Ba atoms are represented in blue, oxygen in red and titanium in green. From Ref [89].*

polarization in the FE film. Indeed, rumpling will change the pollarization charges ditribution in the FE. In the electrodes, rumpling will act to incrrase the screening phenomena, thus reducing the depolarizing field, and helping maintain the polarization.

1.4.3 Switching kinetics of ferroelectric capacitors

The traditional approach used to describe the switching kinetics of ferroelectrics is the Kolmogorov-Avrami-Ishibashi (KAI) model [90], based on the classical theory of Kolmogorov [91] and Avrami [92]. By assuming unrestricted domain growth in an infinite crystal, this model predicts the polarization change $\Delta P(t)$ to be:

$$\Delta P(t) = 1 - exp[-(\frac{t}{\tau})^n] \tag{1.9}$$

where n is the effective dimensionality and τ the characteristic time.

This theory considers the switching process as the phase transformation with a constant nucleation rate, with domain wall velocity as the rate-limiting parameter. However this theory is only valid for infinite crystals [93], and in the case of polycrystalline FE films, nucleation-limited models describe in a better way the switching kinetics [94].

We can distinguish different switching behavior for large capacitor (> 1 μm in diameter) and smaller ones. Indeed for small capacitors, a strong effect of the electrode perimeter will induce larger contribution of the domain wall motion in the polarization reversal process [95,96]. This theory needs direct studies of the switching kinetics to gain further theoritical interpretation. However, characterizing the domain kinetics in FE films proves to be difficult, due to a lack of experimental methods for such experiments. Indeed, the small capacitor size (> 1 μm in diameter) also pairs with very low switching times (well below 100 ns [97,98]).

A study by Gruverman *et al.* in 2008 succesfully attempted to investigate FE capacitor switching on a microsecond time scale for the first time, establishing a direct relationship between the polarization $P(t)$ and the domain kinetics. Using piezo force microscopy to image FE domains during switching, they showed that the scaling effect on the polarization reversal process is indeed governed by different rate-limiting mechanisms in the case of larger and smaller capacitors. For larger capacitors, the switching behavior can be approximated using the nucleation-limited model, whereas for the smaller capacitors, this models no longer applies and might correspond to a reversal governed by domain wall motion. It as been showed these small capacitors will switch faster at high fields, and slower at low fields, whereas it is the opposite for larger capacitors.

1.5 Conclusion

In this chapter, the concept of ferroelectricity was introduced, using BTO to illustrate the phenomena occurring when leading to FE polarization (such as the phase transitions in the BTO). The main issue regarding the stabilization of ferroelectricity in thin films, due to the depolarizing field, can be overcome by different mechanisms of screening. The use of metallic oxide electrodes is especially efficient, and needed in real-like devices. This introduces the core of this thesis, *i.e.* the study of the top electrode/FE interface in electrode/FE/electrode heterostructures with metallic oxide electrodes. At this interface ionic displacement, rumpling, is especially helpfull to screen the depolarizing field.

Chapter 2

Experimental considerations

In this chapter, we will introduce the experimental techniques used to investigate the interface between the FE $BaTiO_3$ and the different electrodes used, $SrRuO_3$ and Au/Co. To ensure that the samples are ferroelectric, several characterization techniques such as C-V and I-V measurements, P.U.N.D. and Piezo Force Microscopy were used. The functioning details of these tests will be presented in the first part of this chapter. In the second part, we will introduce photoemission spectroscopy in general, and then the specific techniques (hard X-ray photoemission spectroscopy, photoelectron emission microscopy and hard X-ray photoelectron emission microscopy) used to investigate the device interfaces.

2.1 Ferroelectricity characterization techniques

2.1.1 Direct measure of the ferroelectric polarization

The defining feature of the electrical properties of a ferroelectric material is how its polarization P behaves in presence of an electric field E. Obtaining P as a function of E gives key information, such as remnant and saturation polarization (P_R, P_S) and coercive fields (E_C^+, E_C^-). However, it is not possible to directly measure the polarization vector itself. To access this value, one has to quantify the variation of polarization when applying an electric field. In Polarization-Field ($P - E$) loops, the current flowing through the ferroelectric material is measured while applying a voltage. This current is directly related to the change in polarization when it is switched by the electric field.

Figure 2.1 a) shows a $P - E$ loop for an ideal ferroelectric material. From the origin of the graph, the applied bias first brings the FE material in one of the saturated polarization states (here the $P^\uparrow$ state, represented by the dashed line on the figure). Once the material reached the saturated state, it will not come back to the origin on the graph. Figure 2.1 b) shows a

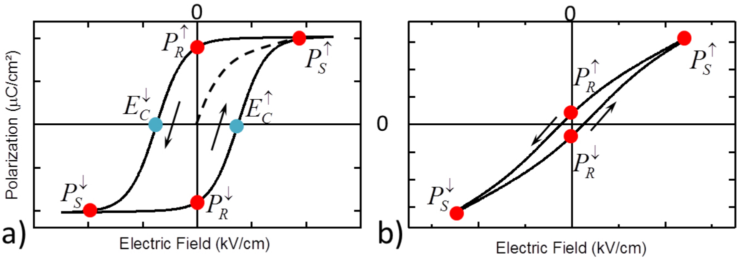

FIGURE 2.1 – *Theoretical polarization versus field curve for an ideal ferroelectric material.* P_R *and* P_S *are respectively the remnant and saturation polarization, and* E_C *is the coercive field.*

$P-E$ loop in the case of a ferroelectric material exhibiting leakage. The FE hysteresis cycle is characterized by several values:

- The saturation polarization P_S. It corresponds to the value of the polarization at the saturation of hysteresis. This also corresponds to the highest polarization possible for reversibility before breakdown.

- The remnant polarization P_R. In the case of an ideal ferroelectric material with a nearly square hysteresis loop, it is almost equivalent to P_S. (Fig. 2.1 a)). However, it can be different from the spontaneous polarization. This often occurs for imperfect materials, as the capacitor might experience some leakage responsible for a loss of ferroelectricity at the remnant state, and P_R will be smaller than P_S (Fig. 2.1 b)).

- The coercive field E_C. It is the necessary field to bring the polarization to zero. An ideal hysteresis loop is symmetrical (Fig. 2.1 a)), so the positive and negative coercive fields are equal.

The coercive field, spontaneous and remanent polarization, and the shape of the loop may be affected by many factors including the thickness of the sample, presence of charged defects, mechanical stresses, preparation conditions and thermal treatment.

In 1930, Sawyer and Tower introduced a circuit allowing measuring the hysteresis cycle of the polarization as a function of the electrical field on Rochelle Salt [99]. The principle is to measure the variation of charge (or equivalently time-integrated current) induced by a voltage sweep. A standard Sawyer - Tower circuit is shown in Figure 2.2.

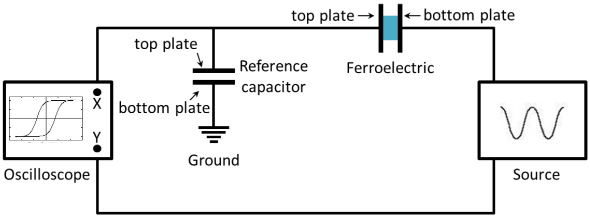

FIGURE 2.2 – *Schematic circuit for a Sawyer - Tower measurement.*

The source of this electrical circuit is a signal generator, which applies a sweeping voltage X across the capacitors. Charges are thus flowing from the source onto the bottom plate of the ferroelectric material. Charges will leave the top plate of the ferroelectric capacitor and accumulate at the top plate of the reference capacitor (also called linear sense capacitor). If C is the capacitance of the reference capacitor, its charge Q can be written: $Q = CY(X)$. This means that the voltage $Y = f(X)$ across the reference capacitor will represent the charge Q moving in or out of the ferroelectric capacitor as a result of the applied voltage X. If the material is ferroelectric, the oscilloscope in the (X : Y) graphing mode gives the resulting loop, which follows the equations 2.2:

$$P = \frac{Q}{A} = \frac{CY}{A} \tag{2.1}$$

$$E = \frac{X}{d} \tag{2.2}$$

with d the thickness and A the surface area of the ferroelectric capacitor.

However, experimental loops obtained from this circuit must be carefully interpreted since non-ferroelectric phenomena can significantly alter the signal or make the measurement impossible. Indeed, the main parasitic signal is the linear (non-switching) dielectric response of the ferroelectric overlaping the ferroelectric (switching) response [100]. In some cases, contribution from the probing circuit itself can make the linear dielectric response similar to a ferroelectric one [101]. Therefore, it is possible to mistakenly identify a non FE material as a FE one. Moreover, in partially conducting samples, such as thin films, the probing voltage might lead to high current which will severely distort the signal and even damage the studied material or the probed devices. This is often the case for very thin films since the leakage current increases exponentially when reducing the thickness. This is why this technique is less and less used for the investigation of thin film ferroelectric capacitors.

2.1.2 Positive Up Negative Down pulse train

To overcome the limitation of the Sawyer - Tower method, Traynor *et al.* [102] developed a methodology using a pulsed voltage source. This technique is often used on thin films to access information on the ferroelectricity, such as the polarization switching time, presented in section 2.1.1. The current flowing through the FE capacitor is measured as a function of time: the time-integrated quantity is the change in polarization charge induced by the voltage pulse. This allows differentiating the non-switching contribution from the switching contribution, which is the one related to ferroelectricity itself. This methodology uses the P.U.N.D. (Positive - Up - Negative - Down) train of pulses as depicted in Figure 2.3.

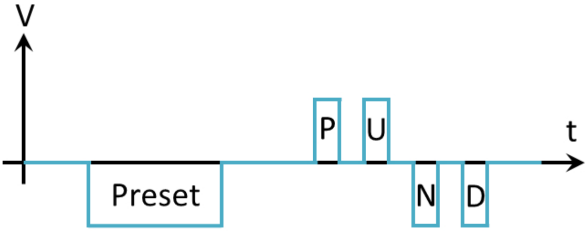

FIGURE 2.3 – *Schematic train of voltage pulses for a P.U.N.D. as a function of time (often in μs).*

After a preset pulse, which produces the initial polarization state ($P^{\downarrow}$ for instance), the source applies a series of switching pulses, as followed:

- Positive (P): This first pulse is applied to the ferroelectric material which is switched from $P^{\downarrow}$ to $P^{\uparrow}$ polarization under the bias. The polarization of the system during the pulse is $P_S^{\uparrow}$.
- Up (U): a non-switching pulse. The ferroelectric between pulses P and U is going to the remnant state $P_R^{\uparrow}$ state when the bias is 0 V. Then it goes back to $P_S^{\uparrow}$ during the U pulse. Therefore, the polarization state of the sample stays the same ($P^{\uparrow}$), which is why U is a non-switching pulse.
- Negative (N): An inverse switching pulse brings the ferroelectric material from $P^{\uparrow}$ to $P^{\downarrow}$ polarizations state. The polarization of the system during the pulse is $P_S^{\downarrow}$.
- Down (D): a non-switching pulse. Similarly as for the U pulse, the sample is brought to the remnant state $P_R^{\downarrow}$. It then goes back to $P_S^{\downarrow}$, making this a non-switching pulse.

The two non-switching pulses Up and Down leave the sign of the polarization unchanged. Thus, they are only symptomatic of the dielectric response of the probing circuit itself, and show the response of the system to the bias application, which is not related to a change in the polarization. On the other hand, the switching pulses Positive and Negative contain both the response of the circuit and of the polarization switch. The responses of the non-switching pulses are subtracted from the responses of the switching pulses. The results allow accessing information only on the polarization switching process itself. As this technique is mainly used to determine the characteristic time of the FE switching process, the time scale of the pulses is typically less than a microsecond.

Figure 2.4 a) shows the applied voltages as a function of time from a P.U.N.D. train of pulses, marked P, U, N and D. Figure 2.4 b) shows the resulting current as a function of time for typical currents in the range of few mA. These results are extracted from a study from Abe *et al.* [103] with measurements performed on a 58 nm thick heteroepitaxial BTO sample. The area under the curve corresponds to the charge displacements Q_U, Q_D, Q_P and Q_N.

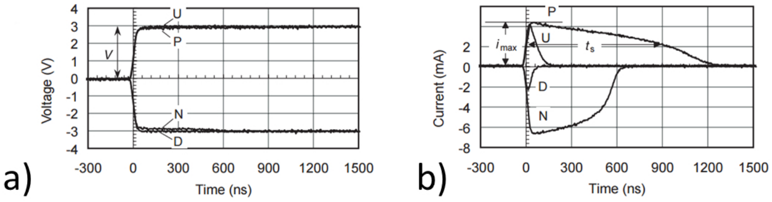

FIGURE 2.4 – *a) Applied voltage waveforms and b) current through the ferroelectric as a function of time, measured for a BTO film after offsetting the data so that current curves start at t = 0. Data from Abe et al. [103].*

The charge displacements Q_U and Q_D after non-switching pulses are subtracted from the switching charges Q_P and Q_N to give a measurement of the remnant polarization P_R and Q_N:

$$P_R = \frac{1}{2} \times \frac{Q_P - Q_U}{Q_N - Q_D} \tag{2.3}$$

This method is widely used in P-E measurement systems. The results of the measurements depend on the width, magnitude, rise time and time separation of each voltage pulse. These measurements give access to numerous informations such as coercive fields, switching times and internal fields [103–105].

The P.U.N.D. train technique was used during the framework of this thesis to access the characteristic time of polarization switching of a SRO/BTO/SRO heterostructure. We connected the heterostructure *in situ* in the X-ray photoemission spectroscopy vacuum chamber and the P.U.N.D. pulse train was applied on the sample while time-resolved X-ray photoemission spectroscopy measurements were simultaneously performed. The core-levels shifts were used to access the characteristic time value of the polarization switching.

2.1.3 Electrical Characterization

a) Capacitance - Voltage curves

Capacitance - Voltage (C-V) curves are specific for each FE material and contain precious information, not only on its dielectric properties but also on its ferroelectric properties. Brennan developed a thorough analysis of the phenomena involved in the C-V curves of ferroelectrics [106]. In this experiment, the dielectric properties of the sample are investigated by superimposing an alternating current (a.c.) probe signal to a direct current (d.c.) bias. A LCR (Inductance - Capacitance - Resistance) meter measures for each d.c. voltage step the capacitance for a fixed a.c. amplitude and frequency. Figure 2.5 displays a typical C-V loop for a perfect ferroelectric BTO sample. When the bias is increased from − 1.5 V to + 1.5 V, the FE capacitance of the material rises to reach its maximum at the coercive voltage V_C^+. Indeed when approaching the coercive voltage, *i.e.* the value for which the polarization switches, the ferroelectric material exhibits a very high permittivity (any small change in the applied field induces a large change in material polarization) and consequently a very high capacitance. When switching from $P^\uparrow$ to $P^\downarrow$, the capacitance reaches its maximum value at the coercive voltage V_C^-. In the case of a perfect FE as presented here, the two branches will cross at a voltage of 0 V, and are symmetric about this point, meaning that the sample will have the same probability of being naturally $P^\uparrow$ or $P^\downarrow$ when no bias is applied. Therefore, when a d.c. bias loop is performed, the resulting curve - widely known as the butterfly-shape loop in the case of FE materials - indicates the existence of the two remnant states of opposite polarization $P^\uparrow$ and $P^\downarrow$. C-V loops also give access to quantitative information on charge carriers, built-in field and permittivity of the ferroelectric layer [106–108].

b) Current - Voltage curves

C-V curves are often linked to Current - Voltage (I-V) curves to investigate the conduc-

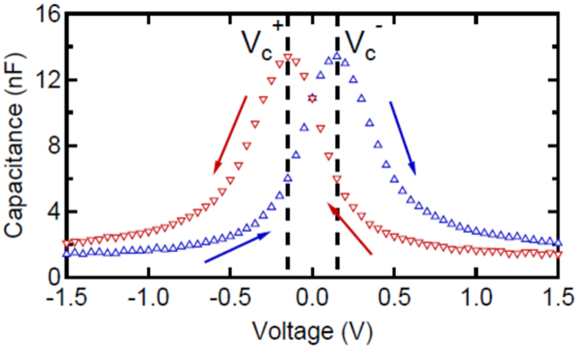

FIGURE 2.5 – *Theoretical Capacitance - Voltage loop for a hypothetical ideal ferroelectric material. Bias is first applied from -1.5V to 1.5V (blue curve) and back (red curve), with blue and then red arrows indicated the travel on the loop. Two dashed black lines indicate the maxima of the loop corresponding to the value of coercive voltages V_C^+ and V_C^-.*

tive properties of the sample. Many concepts from the semiconductor field are used to analyze these measurements on ferroelectrics. For instance, thin ferroelectric films may exhibit thermionic emission or ohmic conduction [109].

C-V and I-V electrical characterizations are often used on typical FE materials. In our case especially, we chose to perform C-V and I-V analyses as we were able to perform those characterization with a single set up, both *ex situ* and *in situ* in the X-ray photoemission spectroscopy and hard X-ray photoemission spectroscopy set ups. This allowed us to characterize the sample and check its ferroelectric nature before and after deposition of the electrode during the fabrication process, but also to verify that the ferroelectricity was maintained during the photoemission experiments.

2.1.4 Piezo Force Microscopy

The operation principle of a Scanning Probe Microscope (SPM) is based on the detection of a signal – the local deflection – at the position of a soft cantilever-type spring with a sharp tip mounted at its end. Figure 2.6 shows a schematic of a SPM. The forces acting on the tip after it has approached the sample surface causes a deflection of the cantilever (according to the Hooke's law stating that the force needed to extend or compress a spring by some distance is proportional to that distance). This deflection is measured by the reflection of a laser beam off the back of a cantilever. A SPM allows moving the sample so that the area of interest can be scanned by the tip. The tip, connected to the cantilever will move following the topography or electrical properties of the scanned area. Bending the cantilever will induce a displacement of a laser spot on a four-sectional photodiode and, as a consequence, a change of voltage in one of the quadrant of the photodiode. From the feedback provided by the diode, the vertical position of the tip is regulated with respect to the sample surface. By keeping the deflection constant while scanning the sample, a three-dimensional map of the surface topography can be obtained.

Among the different SPM modes, Atomic Force Microscopy (AFM) is widely used to image the topography of a sample. Another mode, often used to investigate ferroelectric materials, is the Piezoresponse Force Microscope (PFM). This technique was reviewed by Soergel in 2011 [110]. In addition to mapping the physical topography, the technique allows characterization of the ferroelectric nature of the sample, and also permits applying a current through the sample in order to modify its polarization state, when using a conducting tip.

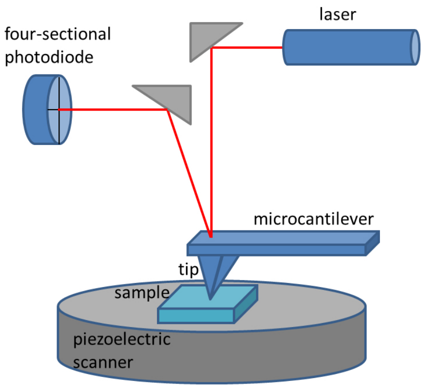

Figure 2.6 – *Schematic of a scanning probe microscope. The piezoeletric scanner allows movement of the sample. The tip is mounted on a cantilever which reflects a laser beam to a four-sectional photodiode. The repulsive-attractive forces between the surface and the tip induce vertical movements of the microcantilever which deflects the beam and changes the photo-diode signal.*

The force involved in the PFM technique is due to the converse piezoelectric effect. The linear coupling between the electrical and mechanical properties of the sample is probed by the PFM tip. Since all ferroelectrics exhibit piezoelectricity, an electric field applied to a FE sample results in a change of dimension. To detect or switch the polarization orientation, the PFM tip acts as a top electrode which can be moved over the sample surface. In reading mode, for each position step, an a.c. signal is used to detect the alteration of the excitation phase due to out-of-plane polarization orientation. The PFM gives an image of the phase shift of the a.c. signal which can be related to the out-of-plane direction of polarization (up or down). This technique can also be used to measure in-plane polarization, as presented by Kalinin *et al.* [33], but will not be used in this thesis.

PFM can also be used to directly switch the FE polarization. This is done in writing mode. At each position, a d.c. bias of typically a few volts is applied between the tip and a grounded bottom electrode to switch the ferroelectric polarization in the desired direction.

PFM has the advantages of any scanning microscopy: a very good lateral resolution (10-20 nm nano-sized domains can be written or detected on ferroelectric surfaces [73]), simultaneous ferroelectric and topographic information, and the possibility of time-resolved PFM to investigate the kinetics of domain switching [111]. A P-E hysteresis loop experiment, as described in section 2.1.1, is usually the solution chosen to verify the ferroelectric nature of the scanned area and access the desired quantitative information (such as the coercive voltages). A key point of PFM is that the probe is local with the tip having a very small surface (few nanometers) compared to the electrodes (a few micrometers) used in classic $P-E$ hysteresis loops. This limits the effect of exponential leakage currents. Moreover, the PFM technique can also be used to provide information on the polarization itself. For example, Tian *et al.* use PFM phase and amplitude variation as a function of the voltage to characterize polarization-induced resistance switching in poly(vinylidene fluoride) tunnel junctions [112].

PFM provides information on the bulk of the film. Indeed, ferroelectricity is measured throughout the entire capacitor and one cannot access specific information of the surface. In the framework of this thesis the major question is on the possible effects at the interface between the FE and the electrode, *i.e.* located at the surface of the BTO. We therefore need complementary techniques to probe only the BTO at its surface. For this reason, photoemission spectroscopy and photoelectron emission microscopy were used to probe the capacitor and are presented in the following section.

2.2 Photoemission Spectroscopy

Photoemission Spectroscopy (PES) is a very sensitive technique to access the electronic and chemical properties of the sample surface. This technique is based on the photoelectric principle stating that when illuminated by a photon beam, an atom can absorb a photon of sufficient energy, leading to the photoemission of an electron from one of the electronic levels in that atom. From this phenomenon, we can access a wide range of information on the photoelectron such as its kinetic energy, take-off angle and wave-vector. PES is thus a very versatile and powerful analysis technique, providing access to the electronic structure of a very wide variety of materials, from complex bulk structures down to free atoms. For this reason, it is widely used in material science, primarily in solid-state and surface science. Based on PES, several experimental techniques were developed, such as X-Ray Photoemission Spectroscopy (XPS), Angle-Resolved PhotoEmission Spectroscopy (ARPES), X-ray Photoemission Diffraction (XPD), PhotoElectron Emission Microscopy (PEEM) or even Time-resolved XPS, each with its own specificities. The principle of PES goes back to the photoelectric effect discovered by Frank and Hertz in 1887 [113] stating that electrons are ejected from a metal when it is illuminated by electromagnetic radiation. Einstein gave in 1905 the explanation of the photoelectric effect in one of his three seminal papers of that year [114], along with Compton's work on inelastic X-ray scattering [115]; those were essential discoveries confirming the corpuscular nature of the light and giving the theoretical basis for the development of PES. The development of PES techniques received significant improvements in 1957, when Siegbahn *et al.* studied the energy levels of core electrons in atoms using X-rays excitation [116]. This work is also the first example of the use of high energy X-rays that were used to recently develop the Hard X-ray Photoemission Spectroscopy technique, presented below. This technique was described in the recent work from Woicik [117]. Siegbahn was awarded the Nobel Prize in 1981 for *"his contribution to the development of high-resolution electron spectroscopy"*. Since then, many contributors helped the development of such techniques [118–122].

2.2.1 The Photoemission process

a) Theoretical principle

Einstein described in 1905 [114] the phenomenon that when a material is illuminated by a photon beam, the absorption of a photon of sufficient energy by an atom leads with a given probability to the photoemission of an electron. The possibility to collect and analyze the kinetic energy of the emitted electron to describe properties of the emitting atomis is the basis of the PES principle. Figure 2.7 schematizes this effect.

The absorption of a photon with energy $h\nu$ causes the excitation of an initial state of a system of one atom surrounded by N-electrons with the energy $E(N)$ into a final state of the same atom with N-1 electrons with an energy of $E(N-1)$ and a photoelectron

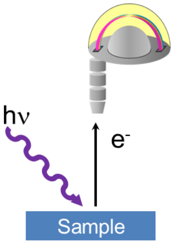

FIGURE 2.7 – *Schematic of the photoelectric effect. A beam of photons (purple arrow), with an energy $h\nu$, illuminates the sample. The emitted photoelectron (black arrow) is then collected by a detector to be analyzed.*

with a kinetic energy KE . From the conservation of energy, the initial system (before emission) and the final system (after emission) have the same energy. Therefore:

$$h\nu + E(N) = E(N+1) + KE \tag{2.4}$$

The binding energy BE of the photoemitted electron can be written as:

$$BE = E(N) - E(N-1) \tag{2.5}$$

From this, the dependence of the binding energy and the kinetic energy can be written:

$$h\nu = KE - BE \tag{2.6}$$

This binding energy is specific to the electronic level of the atom from which the electron is photoemitted, *i.e.* it will change with the chemical environment of the atom. For this reason, Siegbahn coined the name Electron Spectroscopy for Chemical Analysis (ESCA). The term XPS is also widely used to describe PES with a X-ray source.

b) The three step model

The photoemission process in solids can be described most comprehensively according to the one-step model, that has been developed by Adawi and Pendry in Ref. [123, 124]. This model is based on a full quantum description of the photoemission phenomenon, taking into account the coupling of an initial state (Bloch wave in the crystal) of an electron with an available final state. Although less rigorous, the three step model is more accessible and gives a physically more transparent picture of the process. This model separates the photoemission of a single electron into three main processes: the photoexcitation of the electron in the solid, the transport of this electron towards the surface and the transmission of the electron through the surface of the material.

Step 1: Photoexcitation of the electron in the solid

Inside the solid, we consider the excitation of electrons from an initial state i with a wave function ψ_i to a final state f with a wave function ψ_f, by a photon field described by a vector of potential A. We can estimate the probability for this transition, w, as:

$$w \propto \frac{2\pi}{\hbar} | < \psi_f | r | \psi_i > |^2 \delta(E_f(k_f) - E_i(k_i) - h\nu) \tag{2.7}$$

where $h\nu$ is the incident photon energy, and $E_{i,f}$ are the energies of the initial and the final state of momentum $k_{i,f}$.

The matrix element $| < \psi_f | r | \psi_i > |$ contains the information on the probability of the transition from the initial state to the final state. Working in the framework of perturbation theory, *i.e.* the Fermi's Golden Rule [1] and the dipole approximation (which assumes that the wavelength of the radiation is large compared to the interatomic distance), the matrix element is written:

$$| < \psi_f | r | \psi_i > | = | < \Phi_{f,KE} | r | \Phi_i > || < \psi_f(N-1) | \psi_i(N-1) > | \tag{2.8}$$

The matrix element is thus the product of one electron matrix element and a (N-1) electron overlap integral. If we assume that the final and the remaining orbitals are the same in the initial and the final state (in the Koopman approximation or frozen orbital approximation [125]), then the second term of the matrix element, *i.e.* the overlap integral, is equal to one. In that case, the binding energy defined above is equal to the Hartree-Fock orbital energy of the electron in its initial state, as the matrix element is reduced to the first term only.

However, in general this approximation is not necessarily true. The system can relax after the ejection of the electron to minimize its energy, leading to different excited states s and the matrix element is calculated by summing over all the possible final excited states:

$$| < \psi_f | r | \psi_i > | = | < \Phi_{f,KE} | r | \Phi_i > \sum_s c_s \tag{2.9}$$

With $c_s = | < \psi_f(N-1) | \psi_i(N-1) > |$

---

[1] Fermi's golden rule is a way to calculate the transition rate (probability of transition per unit of time from one energy eigenstate of a quantum system into a continuum of energy eigenstates due to a perturbation).

Thus, from 2.7, the photoelectron intensity spectra can be theoretically calculated as:

$$I(E,h\nu) \propto \sum_{f,i}(| < \Phi_{f,KE}|r|\Phi_i >^2 \sum_s |c_s|^2\delta(E_f(k_f)-E_i(k_i)-h\nu)\delta(k_f-ki))\times\delta(E-E_f(k_f)-\Phi_s) \tag{2.10}$$

where Φ_s is the work function, *i.e.* the smallest energy needed at 0 K to extract an electron from the solid.

After photoionization, the emitted electron has a kinetic energy which depends on the photon energy, its initial state in the emitting atom and its environment.
The width of the photoemission peak is due to the convolution of an experimental broadening (Gaussian shape) and the intrinsic energy width of the photoionized state (Lorentzian shape). The intrinsic energy width is directly related to the lifetime of the state, as expected from the uncertainty principle.

Step 2: Transport of the photoelectron towards the surface
During its travel through the material towards the surface, the photoelectron will undergo Coulomb interaction with its surroundings, suffering elastic and inelastic scattering processes. We can distinguish three main scenarii schematically presented in figure 2.8 a), with a typical resulting spectrum in figure 2.8 b):

- the electron does not undergo inelastic scattering: it will contribute to the main (elastic) photoemission peak of the emitting element (Figure 2.8, case (i))

- the electron encounters at least one inelastic scattering event: it will lose kinetic energy and contribute to the secondary electron background (Figure 2.8, case (ii))

- the electron undergoes too many inelastic scattering events and is no longer able to overcome the work function barrier (Figure 2.8, case (iii))

As a consequence of the utilization of electrons, a practical limitation is that experiments must be conducted in ultra-high vacuum (below 10^{-9} mbar in typical PES experiments) so that emitted photoelectrons do not undergo scattering with the atoms present in the atmosphere of the analysis chamber, while traveling from the sample to the analyzer.

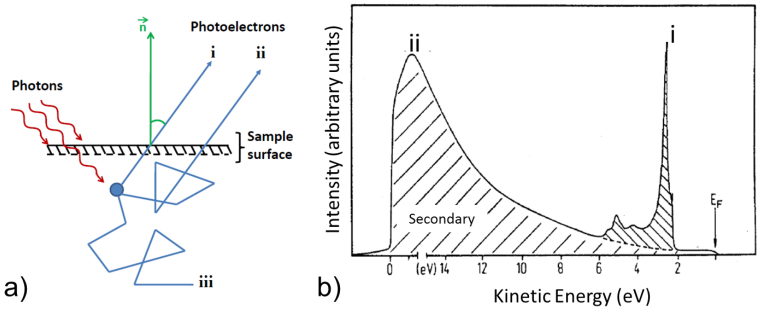

FIGURE 2.8 – *a) Scattering processes involved in photoemission (i) primary electrons, (ii) secondary electrons and (iii) non-emitted electrons, b) typical resulting PES spectrum.*

Step 3: Transmission of the photoelectron from the solid to the vacuum

Near the surface, the photoelectron has to cross the barrier potential, also called work function, to exit the material. The definition of the work function of a surface is the smallest energy needed at 0 K to extract an electron from the solid into the vacuum. Equation 2.11 gives the kinetic energy KE of a photo-electron emitted after absorption of a photon of energy $h\nu$ from a level of binding energy BE, schematically represented in Figure 2.9. The binding and kinetic energies in this equation are expressed in reference with the Fermi level.

$$KE = h\nu - \Phi_s - BE \tag{2.11}$$

b) Core level spectra study

Figure 2.10 shows a schematic representation of the energy levels of a standard PES acquisition. When the sample is electrically connected to the spectrometer (see Figure 2.10), the Fermi level of the spectrometer and the sample becomes equal. We can thus express the kinetic energy of the photoelectrons as a function of the measured kinetic energy KE_{meas} as:

$$KE = KE_{meas} + (\Phi_{spec} - \Phi_{sample}) \tag{2.12}$$

where Φ_{spec} is the work function of the spectrometer and Φ_{sample} is the work function of the sample by measuring KE_{meas}.

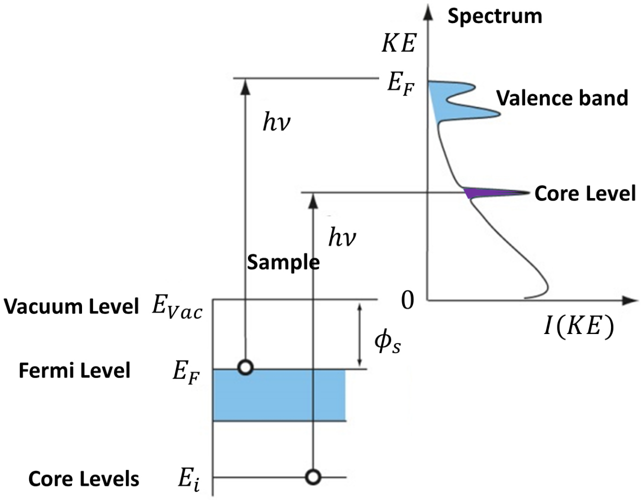

FIGURE 2.9 – *Energetics of the photoemission process (adapted from Ref. [120]). Photo-electrons of kinetic energy KE emitted after absorption of a photon of energy $h\nu$ from an electronic level of binding energy BE are schematized in purple, and photoelectrons from the valence band emitted from the Fermi level are schematized in blue.*

According to this equation, the calculation of KE implies knowing the value of Φ_{sample} for each sample. To overcome this issue, the Fermi level of the spectrometer is chosen as a reference and the conservation of the energy can be written as:

$$h\nu = KE_{meas} + BE + \Phi_{spec} \tag{2.13}$$

By knowing the photon energy and the work function of the spectrometer, it is easy to access the binding energy of the considered atom.

Energy shift of the core level

This binding energy is specific to the electronic level of the atom from which the electron is photoemitted, *i.e.* it will change accordingly with changes in the chemical environment of the atom.

The electronic energy levels, including core-levels, are sensitive to the binding state of an atom with its environment. This induces a displacement of the electronic levels on the binding energy scale, called chemical shift. The difference in binding energy between

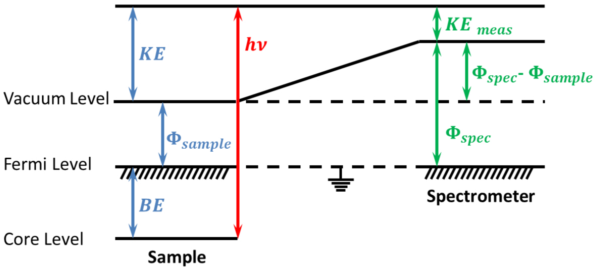

FIGURE 2.10 – *Schematic representation of the energy levels during an acquisition. The sample and the spectrometer are electrically connected so that their Fermi levels are equal.*

two electrons emitted from an identical atom, located in different chemical environments 1 and 2, ΔBE, can be written:

$$\Delta BE = BE(2) - BE(1) \tag{2.14}$$

The binding energy can be expressed as the sum of the orbital energy Îţ with an added term for the relaxation energy E_R. We can thus write the difference in binding energy as:

$$\Delta BE = \Delta\varepsilon + \Delta E_R + \Delta E_F \tag{2.15}$$

where

- $\Delta\varepsilon$ is the chemical displacement. It represents the change in potential felt by the electron during the creation of a chemical bond between two atoms. This effect comes from two contributions. If we consider an atom i, its valence electrons (having a charge q_i) will modify the felt potential by the core electron. This very electron will also experience a second potential from the other atoms of the system. We can express this second potential as $\sum_{j\neq i}\frac{q_j}{r_{i,j}}$ where q_j is the charge of the electrons and $r_{i,j}$ the distance between the atoms i and j. Thus, we can write:

  $$\Delta\epsilon = k \cdot q_i + \sum_{j\neq i}\frac{q_j}{r_{ij}} \tag{2.16}$$

  where k is the Coulomb interaction between core electron and valence electrons.

- ΔE_R is an energy term representing the relaxation of the electrons during the process of photo-ionization of an electron.

- ΔE_F represents an eventual modification ot the position of the Fermi level.

Spin orbit-coupling:

An electron in an atom may possess orbital angular momentum by virtue of its motion around the nucleus (if it is in an orbital with an orbital quantum number $l > 0$) in addition to its intrinsic spin angular momentum. Since the electron carries a charge, there is a magnetic moment associated with its angular momentum.

The two magnetic moments associated with the spin and orbital angular momentum of the electron interact and give rise to shifts and splittings of the lines in a spectrum called fine structure. This interaction is called spin-orbit coupling.

If we let the operators for the total orbital and total spin angular momentum of the electrons in an atom be $\hat{L}$ and $\hat{S}$ respectively, the operator representing the shift in energy due to spin-orbit coupling may be written:

$$\hat{H}_{so} = hc\zeta\hat{L} \cdot \hat{S} \tag{2.17}$$

where the spin-orbit coupling constant, ζ, is expressed in wavenumber units (so that $hc\zeta$ is an energy).

In a multi-electronic system, it lifts the degeneracy of the energy levels, and implies to take into account the vector operator for the total electronic angular momentum $\hat{J}\acute{C}$ such as $\hat{J} = \hat{L} + \hat{S}$.

2.2.2 Use of photoemission in material science.

a) Optimization of the XPS experiment

We use the photoionization cross section in order to estimate the probability of the desired transition. Using the Hartree-Fock one-electron central potential and the dipole approximation, cross sections have been calculated (for elements with Z from 1 to 103 for photon energy going from 0 to 1500 eV) and are reported in Ref. [126]. The transition matrix element depends on the nature of the emitting element, the electronic level of the emitted electron, the photon energy and the photon polarization. Cross section values are therefore used to choose the photon energy in order to enhance the contribution of the wanted core-level. Hubbell *et al.* measured in 1980 the cross section of elements from Z = 1 to 100 for photon energies going from 10 MeV to 100 GeV. Figure 2.11 shows the measured total photon cross section for a) lead and b) carbon. Both graphs show a clear drop of the cross section at high photon energies, corresponding to the hard X-ray range. This means that in order to work at these energies, the time of acquisition will be increased to get the same signal to noise ratio than at low energies.

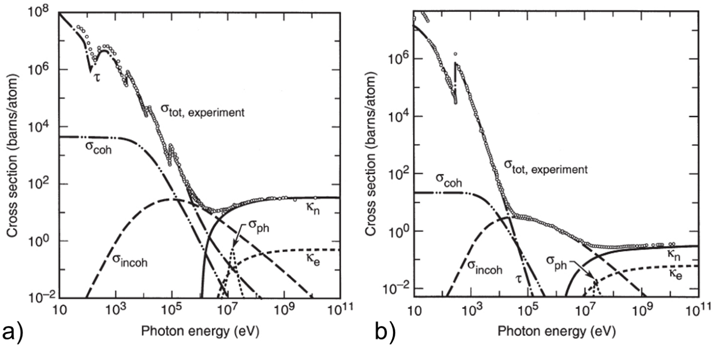

FIGURE 2.11 – *Total photon cross section in a) lead and b) carbon, as a function of photon energy, showing the contribution of different processes:* τ *atomic photo-effect;* τ_{coh} *coherent scattering;* τ_{incoh} *incoherent scattering;* K_n *pair production (nuclear field);* K_e *pair production (electron field);* τ_{ph} *photonuclear absorption. (From Ref. [127]).*

b) Information collected from a typical photoemission spectrum

The observation of a core level photoemission spectrum can give qualitative information. To obtain more precise information on the different chemical environment of an element, the spectrum has to be decomposed into elementary contributions linked to each chemical species. A schematic wide spectrum is shown in Figure 2.12. We can already distinguish at least three types of photoelectrons.

Secondary Electrons The peak of secondary electrons (SE) (as captioned in Figure 2.12) arises from photoelectrons which have lost energy due to many inelastic scatterings. The threshold of the SE peak thus corresponds to the minimum energy for electrons to exit the surface of the sample. This threshold gives the value of the work function. The SE also form the so-called photoemission background for the rest of the spectrum. Most of the time, SE have lost all coherence with their initial state and this background is discarded using a subtracting procedure. In the simplest case, background is removed by subtracting a linear (in energy) contribution to the spectrum. A more sophisticated shape, the

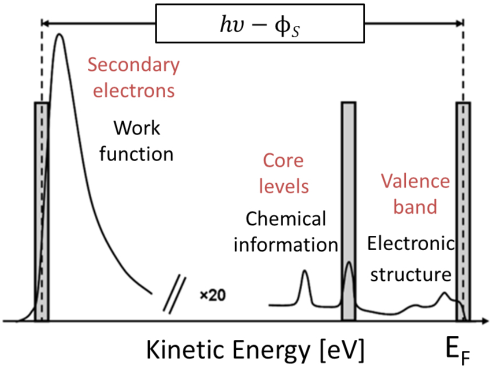

FIGURE 2.12 – *Typical photoemission spectrum, showing the measured intensity as a function of the kinetic energy for three types of electrons: secondary electrons, electrons coming from core-levels and the valence band.*

Shirley background, is more accurate to model the background [128]. Contrary to the linear shape, this model takes into account the fact that the more electrons are excited by the photoemission process, the more electrons are likely to be scattered. Therefore, each main line induces a step in the background intensity and the Shirley background accurately corrects this phenomenon.

Core-levels The exact calculation of the binding energy is very difficult in terms of computation time. Therefore, less time consuming models based on the Born-Haber cycle [87, 129] have been developed to calculate the binding energy of core-levels, but they are not as accurate as an exact calculation. In any case, the measurement of shifts in binding energy, which are characteristic of a change in the chemical environment of the emitting element, is usually more interesting than a precise and absolute determination of the binding energy itself. The cause of such shift is related to the change in orbital energies when the core electronâĂŹs surrounding changes and the value of these shifts can be predicted. However, the binding energy shifts of oxidized barium are a well-known example in the field of oxides where the shift goes in the opposite direction as the one predicted [130]. Many numerical methods exist to estimate the shift in energy from Hartree-Fock Self Consistent Field numerical simulations to electrostatic models using the Madelung potential of the solid to predict or explain the magnitude and the direction of the shifts [131]. Other phenomena might cause binding energy shifts in solids which are not related to a chemical change of the emitting element. While traveling through the surface, electrons are affected by the electrostatic boundary conditions of the sample. This is particularly important when studying the buried interface of any multilayer structure. At the interface between a semiconductor and a metal for instance, band bending induces an internal electric field in the semiconductor [132]. Electronic orbitals from each layer are shifted in energy by the electric field, leading to a distribution of core-level peaks coming from each atomic layer with a slightly different binding energy. This phenomenon has been studied in references [132–135].

Valence band The spectral structure of the Valence Band is usually very complicated, but can in XPS and with low energy resolution correspond to a single peak. The electrons emitted from the valence band determine the electronic properties of the material. Their angle of emission allows accessing the band structure. Two techniques are used to study the band structure of a material: angle resolved photoemission spectroscopy (ARPES) and Photoelectron emission microscopy (PEEM) performed in the k space. The later will be described in section 2.3.

2.2.3 Sensitivity to the surface

a) Inelastic mean free path

Photoelectron spectroscopy is a highly surface sensitive technique. This is due to the inelastic mean free path of the photoelectrons, λ. This value describes the average length an electron travels between two successive inelastic scattering events in a material. Using the well-known Beer-Lambert attenuation law [136], the effect of this scattering can be expressed and the probing depth can be estimated:

$$I(z) = I_0 \exp -(\frac{z}{\lambda \sin\theta}) \tag{2.18}$$

where, as shown on the schematic Figure 2.13 a):

- z is the probing depth
- $I(z)$ is the measured intensity coming from the layer at depth z
- I_0 is the intensity without attenuation
- λ is the inelastic mean free path (IMFP)
- $\sin\theta$ is the take-off angle of the photoelectron

This is illustrated in Figure 2.13 b), on which the probability of emission of a photoelectron P is expressed as a function of the depth z. This curve shows that 95 % of the signal comes from the first 3λ of the material. The inelastic mean free path allows describing the probed depth in PES experiment.

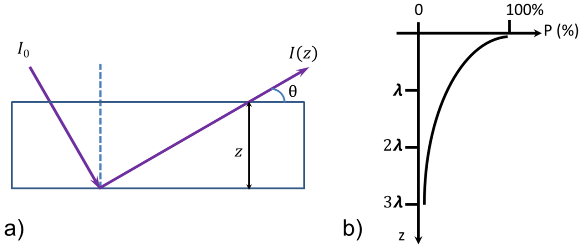

FIGURE 2.13 – *a) Schematic of the geometry involved in equation 2.13 b) Contribution to the photoelectron peak (in %) of the sample as a function of the depth z.*

This quantity λ depends on the material, the element and the electron kinetic energy. Figure 2.14 presents λ as a function of the photoelectron kinetic energy. This curve is usually called universal curve [137], as its shape is more or less independent from the nature of the studied material and is a good estimation of the mean free path for many materials. For the majority of the materials, this curve presents a minimum value for λ of between 3 and 5 for kinetic energies between 50 and 100 eV. Below and above this energy, λ increases. At lower energies, the probability of inelastic scattering decreases since the electron has insufficient energy to cause plasmon excitation (the main scattering mechanism); consequently, the IMFP increases.

Using typical lab sources (1486.60 eV for the Al Kα lab source), photoemission experiments probe the first 2-3 nm of the sample. Indeed as we can see from Figure 2.14, at an energy of 1500 eV, we can access a probing depth of about 2-3 nm, making PES a highly surface sensitive experiment.

b) Hard X-ray PhotoEmission Spectroscopy

As mentioned in the previous section, the IMFP increases for higher energies. The high sensitivity to the surface of the XPS technique can thus be partly overcome by using hard X-ray photons (above 5 keV). Figure 2.15 presents the evolution of λ as a function of the kinetic energy, calculated for 41 elements, for electron energies going from 10 eV to 30 keV. We can see on the curve that for those elements, it is possible to access IMFPs as high as 1000 , and thus to probe deeper into the material, therefore accessing also

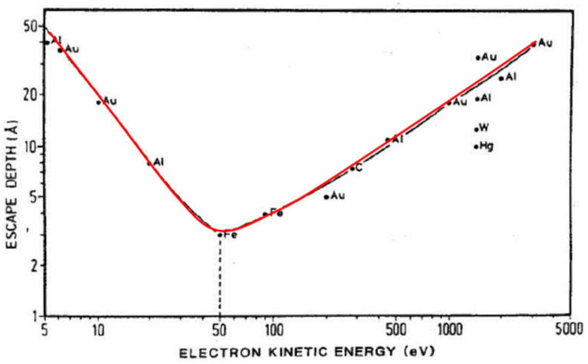

FIGURE 2.14 – *Universal curve of the IMFP as a function of the electron energy. (Fig. taken from [137]).*

buried interfaces [138].

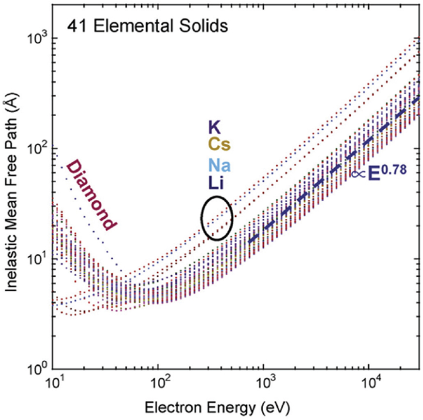

FIGURE 2.15 – *Evolution of the IMFP λ as a function of the kinetic energy, calculated for 41 elements, for electron energies going from 10 eV to 30 keV. From ref [138].*

The technique consisting in reaching higher binding energies by exciting the photoelectrons with photon energies in the hard x-ray regime is called Hard X-ray PhotoEmission Spectroscopy, or HAXPES. An overview of this method was given by Fadley [139]. HAXPES poses several experimental challenges [140], such as the need of modified electron spectrometers able to measure photoelectrons of high kinetic energies while conserving a good energy resolution. Another issue when using HAXPES is that, for most elements, the photoexcitation cross section drops dramatically when increasing the photon energy as previously showed in section 2.2.2. Those phenomena will lower the signal for core level measurement. The only way to overcome this is by increasing the photon flux, making HAXPES experiments very difficult to perform with laboratory sources. The synchrotron radiation can offer higher flux, and synchrotron facilities became an attractive environment to develop such experiments.

The HAXPES experiments, presented in this thesis, were performed on the GALAXIES beamline at the SOLEIL synchrotron, where the photon energy is tunable in the multi-keV regime up to 8000 eV. We could thus achieve greater sensitivity to our buried layer and interfaces. Indeed our heterostructure has a top electrode, whose existence is indispensable to switch the ferroelectric material and carry out *in situ* bias-dependent measurements. To determine the value of the photon energy that would be used, we calculated the IMFP for Ba *4d* in the BTO using the SESSA software [141]. The SESSA software allows simulation of XPS spectra of nanostructures of complex geometry (islands, lines, layered spheres on surfaces, multilayer films...) using a database of physical parameters. Such data include, for example, the inelastic mean free paths, the differential elastic- and total eleastic-scattering cross sections, the Auger-electron lineshapes, etc. A simulation module provides an estimate of peak intensities as well as the peak spectra. Figure 2.16 presents the calculated IMFP as a function of the electron energy for energies going from 50 eV to 10000 eV.

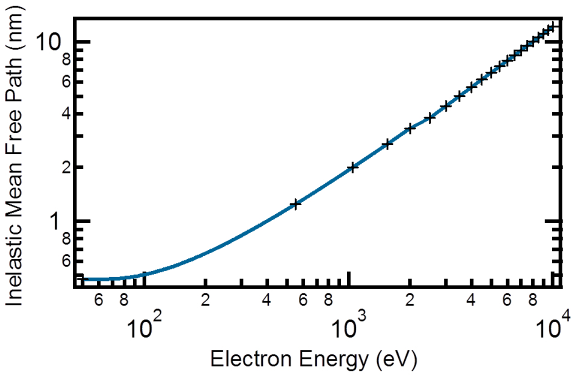

FIGURE 2.16 – *IMFP for the Ba 4d core level in BTO for energies going from 50 eV to 10 keV.*

Using the same software [141], the survey spectra obtained on a SRO(2nnm)/ BTO(60nm)/ SRO(35nm)// STO heterostructure have been simulated for different photon energies. Figure 2.17 presents the obtained spectra using a) a classic Al Kα lab source ($h\nu = 1486.6$ eV) and b) a hard X-ray source at a photon energy $h\nu = 6893.9$ eV.

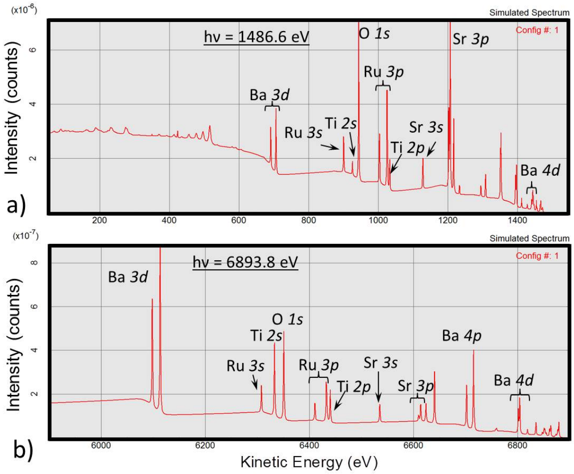

FIGURE 2.17 – *SESSA simulations of survey spectra obtained on a SRO(2nnm) / BTO(60nm) / SRO(35nm) // STO heterostructure using a) a classic Al Kα lab source ($h\nu = 1486.6$ eV) and b) a hard X-ray source ($h\nu = 1486.6$ eV).*

Comparing the relative intensity of the obtained peaks, we can see that the core levels of the BTO (below the top SRO layer) have a much better signal to noise ratio when using hard X-ray. Taking into account these results along with the cross section of Ba *4d*, we used for the main part of our experiments a photon energy of 6900 eV, for which the value of the IMFP for Ba *4d* is 8.8 nm. However, for the time resolved measurements presented in section 5, only soft X-rays were available at the TEMPO beamline. For this reason, we limited our sample to heterostructure with 2 nm top electrodes (as presented in section 3.1) so that the signal from the buried interface would be high enough in the time-resolved experiments.

c) Angle variation

Another way to probe deeper below the surface is to select the takeoff angle of the photoelectron (often by rotating the sample with respect to the analyzer). Figure 2.18 shows a schematic of the situation where a sample is probed with a) a small angle of detection and b) a larger angle of detection. As previously discussed, equation 2.13 obtained from the Beer-Lambert law links the probing depth to the angle of detection. Thus, electrons emitted with a small angle of detection are more likely to be emitted from the topmost surface, whereas electrons with a larger angle of detection are emitted from deeper in the material. Grazing versus normal emission experiments will be used to determine the relative contribution to the signal of surface and bulk atoms.

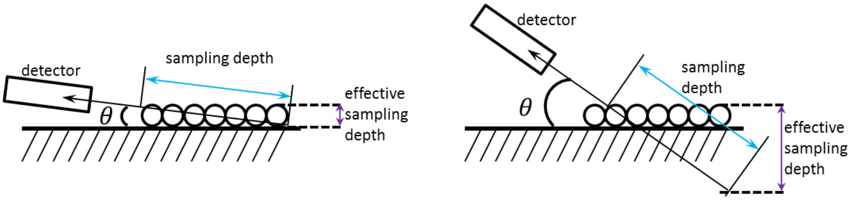

FIGURE 2.18 – *Relative surface to bulk sensitivity in XPS showing the variation of the effective sampling depth with the angle of detection ϑ. Light blue arrows represent the sampling depth whereas the purple arrows represent the actual depth probed. Adapted from Ref. [120].*

2.2.4 Quantitative measurement - Interface thickness calculation

Photoemission spectroscopy based experiments can be used quantitatively to calculate the thickness of a layer, by using the ratio of intensity between components from different layers in the sample. Here, we take the case of a BTO sample, which has a surface layer of unknown thickness. In this example, the two considered layers, the surface and the bulk, are of the same material, but their relative core-level peaks are shifted in energy. This might be due to several reasons such as a different chemical environment, polarization or distortive effects, and this will be investigated in the next chapter. In Figure 2.19 a Ba *4d* spectrum is presented. The envelope (white squares) presents two distinct asymmetric peaks that are due to spin orbit coupling of the *4d* states ($4d_{5/2}$ and $4d_{3/2}$). Peak fitting analysis has allowed linking the asymmetry of the peaks to the presence of two contributions: one from the bulk of the sample, and one relative to the surface of the BTO. We can see that the Ba *4d* core-level signal for the surface layer (dark blue) is shifted to higher binding energies with respect to the bulk component (grey).

Figure 2.20 shows schematically the intensity of the signal photoemitted from a sample with an angle of emission θ (Fig 2.20 a)) and of the intensity emitted from each unit cell of the BTO layer (Fig 2.20 b)). From Fig. a) and equation 2.13 we can write the intensity emitted from a single unit cell of thickness the lattice parameter c, with an angle of emission θ as:

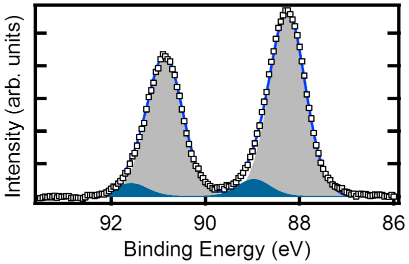

FIGURE 2.19 – *Photoemission spectra of the Ba 4d core-level. The raw spectrum is marked by the white squares. Peaks were fitted by a combination of a surface contribution (filled in dark blue) and a bulk contribution (filled in grey), for both $4d_{5/2}$ and $4d_{3/2}$ components. The resulting fit is showed by a blue line.*

$$I(c) = I_0 \exp\left(-\frac{c}{\lambda \sin\theta}\right) \tag{2.19}$$

Given the TiO$_2$/BaO layer alternation along [001] (see chapter 1) the Ba *4d* photoelectron intensity from the pth BaO layer below the surface can be written:

$$I(p) = I_0 k^p \tag{2.20}$$

where $k = \exp\left(-\frac{c}{\lambda \sin\theta}\right)$

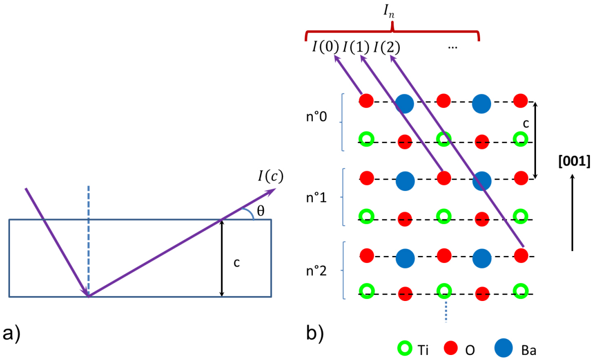

FIGURE 2.20 – *Schematic of a) the intensity emitted from a sample of thickness c with an angle of emission θ (x is the distance traveled by the electrons before exitting the material) and b) of the intensity emitted from each unit cell of the BTO layer.*

If M is the number of unit cells contributing to the interface layer, then the intensity emitted from the surface I_{Surf} and from the bulk I_{Bulk} can be written:

$$I_{Surf} = I_0 \sum_{i=0}^{M-1} k^i = I_0 \frac{1-k^M}{1-k} \tag{2.21}$$

$$I_{Bulk} = I_0 \sum_{i=M}^{n} k^i = I_0 \frac{k^M}{1-k} \tag{2.22}$$

The interface to bulk intensity ratio is therefore:

$$\frac{I_{Surf}}{I_{Bulk}} = \frac{1-k^M}{k^M} \tag{2.23}$$

From this formula, we can calculate the value M of the number of unit cells of the surface layer, and thus the thickness of this surface layer.

$$M = \frac{\lambda \ln \frac{I_{Surf}}{I_{Bulk}} + 1 \sin\theta}{c} \tag{2.24}$$

2.2.5 Operando measurements in photoemission spectroscopies

In the past years, the increasing need of knowledge on electronic and chemical properties of functional devices lead to a development of photoemission spectroscopy with *in situ* bias application. Suzer *et al.* used photoemission spectroscopy to perform chemically-resolved impedance-like measurements on the Rb/SiO_2 interface [142]. Nagata *et al.* conducted several experiments using hard x-ray photoemission on resistive switching devices to probe the interfacial chemical properties as a function of the bias-induced resistive state [143, 144]. Regarding ferroelectric materials, Chen and Klein performed photoemission spectroscopy on a BTO single crystal covered with either Platinum or RuO_2 as a function of the ferroelectric polarization. The ferroelectric polarization is switched *in situ* in this experiment [145]. Rault *et al.* used operando XPS experiments to study the Pt/BTO interface of heterostructures depending on the polarization [25]. All of these studies demonstrate how crucial operando experiments are, in accessing further information on the behaviour of device-like structures depending on their polarization state.

In the framework of this thesis, PES experiments were performed at the synchrotron SOLEIL, on two beamlines using XPS (TEMPO) and HAXPES (GALAXIES). To perform operando measurements on metal/ferroelectric interfaces, the experimental set up has to allow *in situ* bias application, and the sample has to be properly designed. The interface has to be as free of contamination and as sharp as possible. Moreover, it must not be too deeply buried so that the photoemission signal from this interface under the thin electrode is still significant. The size of the capacitor has to be properly chosen to limit leakage currents due to defects. Finally, the electrical connections must be compatible with an ultra-high vacuum (UHV) chamber both in terms of vacuum contamination and easiness of *in situ* manipulation. The designed heterostructure used to answer those issues and the experimental set up used are described in detail in the next chapters 3 and 4 presenting operando experiments.

2.3 PhotoElectron Emission Microscopy

The need for devices of reduced sizes calls for an analysis technique which requires spatial resolution of the same order of magnitude than the studied structures. For this particular need among others, we also used PEEM to study our system. In 1933, Brüche showed that an electrostatic lens accelerating photo-emitted electrons to high energy can be used to image surfaces [146]. This was the beginning of surface imaging using cathode lenses, also called immersion lenses (i.e. the sample itself serving as the cathode). Material science investigation based on low energy electron microscopy techniques took a significant jump forward after the work of Rempfer [147], and then of Telieps and Bauer in the 1980s on the low energy electron microscope [148]. Following Brüche's early work, many years of technological improvements in electron lenses and ultra-high vacuum technology were needed to significantly improve spatial resolution and intensity contrasts [85]. An additional turning point came with the development of dedicated synchrotron radiation sources which provides high brilliance photon flux. It allows photoelectron emission imaging in a reasonable amount of time and enables X-ray absorption imaging [149].

2.3.1 Technical aspect of electron emission microscopy

The PhotoElectron Emission Microscopy (PEEM) is a photoemission-based technique, thus principles presented in the section 2.2 are still valid in PEEM. However, its special feature, in comparison with PES, is that it is an imaging technique, thus allowing conservation of the spatial provenance of the photoemitted electrons thanks to imaging optics. In addition to the lateral origin of the collected electrons, the emission angle and energy of the photoelectrons are conserved, allowing one to unveil information on the surface chemical and electronic structures. This is made possible by the combination of a PEEM column, composed by electrostatic or electromagnetic lenses, followed by an energy analyzer.

By collecting all emitted electrons, the electron optics of a standard PEEM works as a low-pass filter having a higher transmission for slow electrons than for fast electrons. In order to access a specific binding energy of the photoelectron, an energy analyzer is used, in the same way as in standard photoemission experiment [120], working as a band-pass filter, however, with imaging properties.

A typical photoemission spectrum was presented in the previous section in figure 2.12, with the intensity of the collected photoelectrons plotted as a function of kinetic energy. Based on the equation $KE = h\nu - BE - \Phi_S$, we know that primary electrons give access to core levels and to the valence band, giving us information on the electronic structure. At the photoemission threshold, the onset of secondary electrons gives access to the work function. In PEEM, the Fermi level of the sample and sample holder are aligned.

a) Description of the NanoESCA setup

A schematic of the NanoESCA PEEM used for the experiment in this thesis is given in Figure 2.21. Photons of energy $h\nu$ hit the sample, generating a photoelectron current (schematized by a red line) moving through the instrument.

The first part of the microscope is a PEEM column (A - D in Fig. 2.21). It contains the immersion lens (A in Fig. 2.21) which is composed by the sample and the objective lens. The objective lens is at high voltage (typically 12 to 24 kV) while the sample is at a tunable potential V close to the ground. The high electric field allows collecting electrons emitted with large angles. A contrast aperture can be positioned in the back focal plane of the objective (B in Fig. 2.21). Projective lenses (C in Fig. 2.21) then carry the collected photoelectrons towards the entrance slits (D in Fig. 2.21) of the imaging double energy analyzer (IDEA) (E in Fig. 2.21). The band pass of the energy analyzer is set by the pass energy. Applying proper settings, electrons of chosen kinetic energy are slowed down at the entrance of the analyzer to a kinetic energy that matches the pass energy. Hence, selected photoelectrons can travel through the analyzer, giving access to the kinetic energy of the photoelectrons. The binding energy can be calculated according to equation 2.6. Then, these photoelectrons pass through the second analyzer, designed to correct the dispersion of spherical-like aberrations generated by the first analyzer [150]. The two analyzers are linked by a transfer lens system (F in Fig. 2.21). The use of a double hemisphere analyzer and of electrostatic lenses is specific to the design of the NanoESCA. However, several other possibilities for realizing an energy-filtered PEEM exist and are described in the literature [151–153]. Finally, the selected photoelectrons reach an ima-

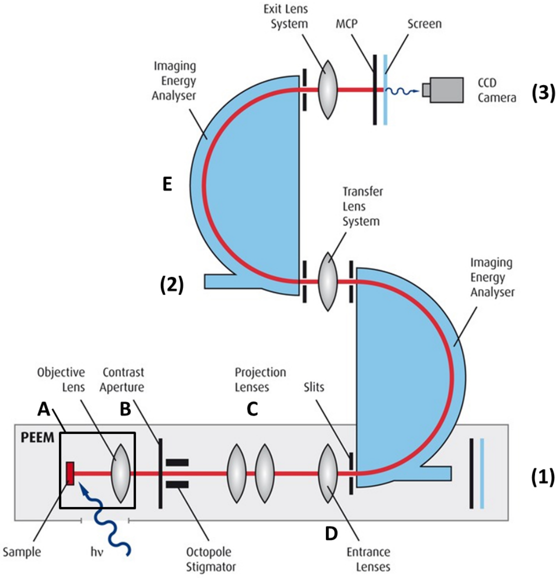

FIGURE 2.21 – *NanoESCA PEEM schematic. The instrument can operate in three modes: (1) direct PEEM, (2) micro-spectroscopy and (3) energy-filtered PEEM.*

ging unit (G in Fig. 2.21) composed of multi-channel plates, a screen and a CCD camera.

b) Energy resolution and transmission

The energy resolution of the NanoESCA analyser is given by [150]:

$$\Delta E_a = PE(\frac{w_1 + w_2}{2R_0} + \alpha^2) \tag{2.25}$$

where PE is the pass energy, w is the width of the energy slits, R_0 the mean radius of the analyzer and α the acceptance angle of the lens system with respect to the optical axis of the analyzer. The resolution can be improved by increasing the transmission of the analyzer, given by [154]:

$$T \propto (\frac{\Delta E}{\sqrt{PE}}\alpha 2R) \tag{2.26}$$

From the instrumental design of the NanoESCA, the remaining chromatic and spherical aberrations induced by the extractor field give theoretical spatial resolution limits in the

30 to 50 nm range [150], governed by the aberrations of the immersion lens [155]. The resolution can be enhanced with the use of a contrast aperture in the back focal plane and smaller energy windows set by the energy filter. In practice, the counting statistics is the primary limitation for the resolution that can be obtained.

c) Modes of operation of the NanoESCA

The NanoESCA can be operated in three different modes:

- (1) the direct PEEM mode: there is no energy filtering and photo-emitted electrons are all collected independant of their kinetic energy. This mode has not been used in this work.

- (2) the micro-spectroscopic mode: a region of interest is selected on the sample (using a field aperture called the iris aperture) and is probed with photoemission spectroscopy, using a channeltron®detector at the end of the first analyzer. Therefore, photoemission spectra can be acquired over a particular ferroelectric domain for instance.

- (3) the energy-filtered PEEM mode: This mode gives access to images resolved both spatially and in energy. An image series gives a stack of images for different kinetic energies $I = f(KE, x, y)$. From this stack, intensity, as a function of the energy, extracted on one pixel leads to a standardİ photoemission spectrum. This mode can also be used to image in the reciprocal space, where the image series takes the form of an image stack $I = f(KE, k_x, k_y)$ with k_x and k_y the components of the electron wave vector [156]. It is possible to select a region of interest in the direct PEEM mode using the iris aperture, and then switch to k-PEEM mode to access the band structure of that region. Hence, a specific region of the surface can be characterized by local core level micro-spectroscopy and band structure imaging.

The NanoESCA setup allows easy switching between the imaging (direct and reciprocal spaces) and spectroscopy modes.

2.3.2 Imaging in the reciprocal space

Primary electrons escape the sample with kinetic energy KE and wave vector $\vec{K}$ into the vacuum. The emission geometry is drawn in Figure 2.22. The emission geometry can be described in a spherical coordinate system, with the polar θ and azimuth φ emission angles defined with respect to the n axis, *i.e.* the sample surface normal. The emission angle and energy are preserved when being collected in the PEEM column.

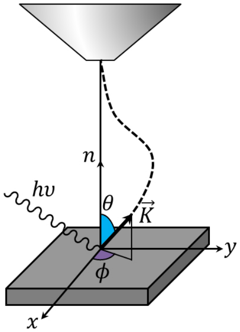

FIGURE 2.22 – *Geometry of the emission and collection of photoelectrons. The surface of the sample (in grey) is illuminated with a beam of photons of energy $h\nu$ and electrons are emitted, with an energy KE, a wave vector $\vec{K}$ and emission angles θ and φ. The photoelectrons particular trajectory (dashed line) is due to the high potential difference between the extractor lens and the sample.*

Once the photoelectron has reached the vacuum, it can be considered as a free electron and therefore described by a plane wave of wave vector $\vec{K}$. From the emission angles (θ, φ) of the electron, the magnitude and components of $\vec{K}$ are:

$$|\vec{K}| = \frac{1}{h}\sqrt{2m_e KE} \tag{2.27}$$

$$K_x = |\vec{K}| \sin\theta \cos\varphi \tag{2.28}$$

$$K_y = |\vec{K}| \sin\theta \sin\varphi \tag{2.29}$$

$$K_z = |\vec{K}| \cos\theta \tag{2.30}$$

where m_e is the effective mass of an electron.

From the conservation of energy, and because of the 2D symmetry of the surface [157], the in-plane component of the emitted photoelectron wave vector is conserved and can be written:

$$\vec{K}_{in-plane} = \vec{K}_x + \vec{K}_y = \frac{1}{h}\sqrt{2m_e KE}\sin\theta \tag{2.31}$$

$$\vec{K}_{in-plane}(^{-1}) = 0.512\sqrt{KE(eV)}\sin\theta \tag{2.32}$$

Figure 2.23 represents schematically the travel road for electrons emitted from the surface in both PEEM and k-PEEM imaging mode. Appropriate electron optics and energy analyzer configurations allow imaging the sample surface either in real or in reciprocal space. In real space, the (x, y) position of the emitted electrons from the surface is projected onto the image (lateral resolution) whereas in reciprocal space, the back focal plane of the objective lens is imaged giving direct access to the in-plane components of the wave vector $\vec{K}$ which carries the angular information (θ, φ) of the emitted electrons (angular resolution).

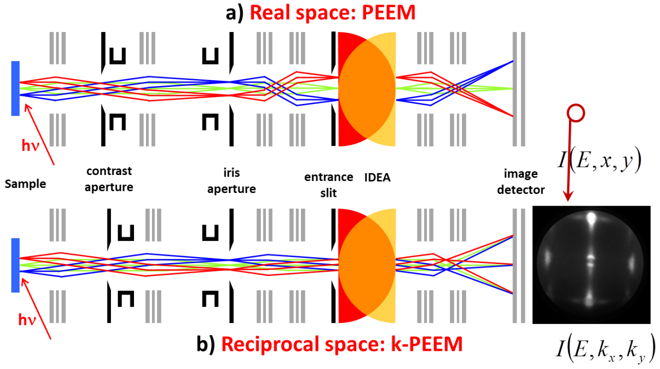

FIGURE 2.23 – *Schematic of the electron beam pattern for the real (PEEM) and reciprocal space (k-PEEM).*

As shown on the simplified schematic, in the real space, the position of the emitted electron is conserved, thus giving access to a real image of the surface. The object plane, positioned once at the iris aperture, is therefore enlarged and projected onto the CCD screen. In the k-PEEM mode, the back focal plane, located in the contrast aperture, is imaged. The angles with which electrons are emitted are conserved, but the information of their spatial origin is lost. The resulting images are a function of the photoelectron wave vectors k_x and k_y. By scanning the energy, an image series can be recorded and we get access to a stack of $I = f(KE, k_x, k_y)$ as presented in Figure 2.24.

2.3.3 Hard X-ray PhotoElectron Emission Microscopy

The information depth of photoemission spectroscopy can be significantly enlarged by increasing the used kinetic electron energies, inducing larger IMFPs, as previously explained when introducing HAXPES (see section 2.2.3). This method can be combined with the PEEM ap-

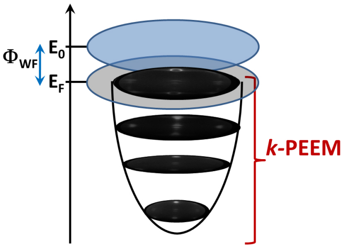

FIGURE 2.24 – *Schematic of the $I = f(KE, k_x, k_y)$ stack obtained using the k-PEEM mode. Images presented ore from a STO(001) sample.*

proach and was used in this thesis using the NanoESCA setup. This technique is called hard X-ray photoemission electron microscopy (HAXPEEM).

The general working principles of HAXPEEM is the same as for the standard NanoESCA described in section 2.3.1. However, the use of high photon energies has consequences, especially on the electron trajectories through the optical elements. Indeed, in a standard PEEM, the energy filtering is controlled by the sample voltage. Thus, higher sample potentials have to be used if higher photon energies are used (as an example, to access the Fermi level of a sample probed with an energy of $h\nu = 10$ keV, the sample voltage has to be set to approximately 10 kV). This induces improving the electrical isolation of the sample stage.

The major issue, in a HAXPEEM setup, is the reduction of the transmission. Indeed, angles of photoelectrons (with respect to the surface normal) at higher kinetic energies have trajectories that are harder to bind by the extractor field. As a result, they risk not entering the column of the microscope. This leads to a reduced angular acceptance, and thus a reduced transmission of the microscope, as seen from equation 2.26 (see section 2.3.1.b). Combined with the already mentioned low photo-ionization cross sections for hard x-rays (see section 2.2.2), this phenomenon drastically lowers the count-rate for core level imaging.

In order to overcome this issue, the HAXPEEM set up uses an extractor voltage at 24 kV. Other specificities of the instrument are also modified such as the potential of the imaging column raised to 2 kV, instead of usually 1 kV, and the distance between the sample and the extractor is increased to 2.5 mm to avoid too high fields at the sample surface which may promote electrical breakthrough. Figure 2.25 summarizes typical settings for the use of HAXPEEM, as described in Patt *et al.* study [158].

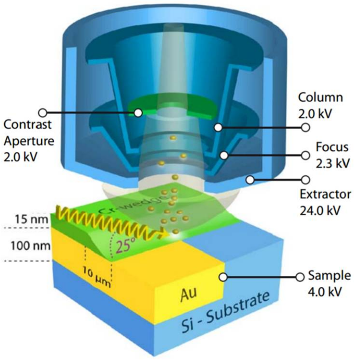

FIGURE 2.25 – *Schematic set up of the HAXPEEM experiment including typical potential settings for the objective lens in the high kinetic energy operating mode. From Ref [158].*

2.4 Experimental details

2.4.1 Different studied heterostructures

In this thesis, we will present the study of two different heterostructures of BTO with top and bottom electrodes. Both have a SRO bottom electrode, grown on a STO substrate. These layers have all been grown by PLD at the Institut d'Electronique Fondamentale (IEF, Orsay, France). Depending on the experimental approach used to study those devices, the top electrode material and geometry was chosen different for both of them. The final designs are presented in Figure 2.26, with a side schematic view of the devices ready for introduction in a photoemission end-station.

A first type of heterostructure (Figure 2.26 a)) was prepared to be studied using operando hard X-ray photoemission. For this heterostructure, we used SRO as top electrode also to study in deeper details the interface between the BTO and the oxide top electrode. A set of several (300×300) μm^2 SRO electrodes was prepared, and one electrode was used to connect the sample so that a bias could be applied *in situ*. Hard X-ray, combined with the *in situ* switching of the polarization allowed us to probe the buried SRO/BTO top interface in both out of plan polarization states $P^{\uparrow}$ and $P^{\downarrow}$. A similar sample was used to study the dynamic of polarization switching of such devices, using time-resolved photoemission. In the same way, *in situ* switching allowed performing time resolved experiment for both out of plane polarization states.

A second heterostructure (Figure 2.26 b)) was prepared to perform hard X-ray photoemission electron microscopy measurements (section 2.3). Therefore, top electrodes to swhitch the FE *ex situ* using piezo force microscopy in the writing mode (section 2.1) were designed. For this sample, we used smaller electrodes as the study was centered on phenomena taking place in very small devices. We chose electrodes of Cobalt (2 nm) capped by gold (4 nm), to compare results with previous study on similar samples by Chanthbouala *et al.* [159]. Once the top electrodes prepared, several were switched *ex situ* into different polarization states.

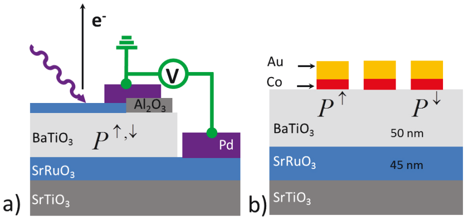

FIGURE 2.26 – *Schematic side view of a) the connected SRO/BTO/SRO and b) the Au/Co/BTO/SRO heterostructures.*

2.4.2 Growth methods of the thin films - use of Pulsed Laser Deposition for our samples

Since SRO can be epitaxially grown on several substrates [40], the processes for depositing SRO thin films have been extended and refined to a high degree. SRO thin films have been grown by a wide variety of approaches. In all cases, the quality of the film growth depends on the choice of the substrate with singly terminated surfaces, and on a precise control of the stoichiometry. In order for SRO to grow epitaxially on a single-crystal substrate, its in-plane lattice parameter and the one of the substrate are required to be close. The residual lattice mismatch introduces strain that can affect the structural and electrical properties of the SRO layer. Bulk SRO is known to have several structural phase transitions. However, the temperatures at which these transitions occur in thin films depend on the nature of the substrate. Several deposition techniques are used to produce SRO films, such as magnetron sputter deposition [40], reactive electron beam coevaporation [160], and pulsed laser deposition.

By far, Pulsed Laser Deposition (PLD) is the most wide spread method for depositing thin films of complex oxides. SRO is no exception, and its first successful synthesis in thin film form was reported by Wu *et al.* [161] on $LaAlO_3$ and later by Chen *et al.* [162] on $SrTiO_3$, using this technique. Subsequently, PLD has been used by many groups, with correspondingly as many deposition conditions of growth (temperature, pressure of the O_2 flux, deposition rate...) reported. Figure 2.27 describes the PLD technique principles.

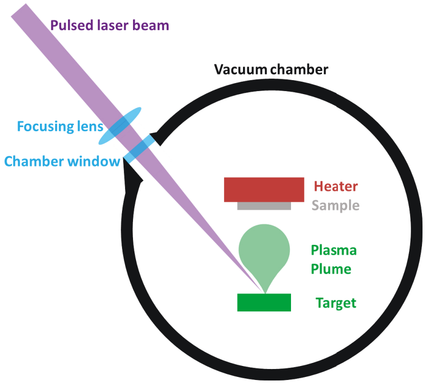

FIGURE 2.27 – *Typical configuration of a PLD deposition chamber. The pulsed laser beam is focused by a lens onto the target material. The material is then vaporized in the shape of a plasma plume on the heated sample.*

PLD is a physical vapor deposition technique where a high-power pulsed laser beam (purple on Figure 2.27) is focused inside a vacuum chamber to strike a target of the material that is to be deposited (green). When the laser pulse is absorbed by the target, energy is first converted to electronic excitation and then into thermal, chemical and mechanical energy resulting in evaporation, ablation, plasma formation and even exfoliation [163]. The target material is vaporized in a plasma plume which deposits it as a thin film on a heated substrate. Said substrate is located face down, above the target, to avoid contamination from falling on the sample during growth. This process occurs in ultra-high vacuum or in the presence of a background gas, such as oxygen which is commonly used when depositing oxides to fully oxygenate the deposited films.

In PLD, a large supersaturation occurs on the substrate during the pulse duration. The pulse lasts around 10 to 40 μs [164] depending on the laser parameters. This high supersaturation causes a very large nucleation density on the sample surface as compared to molecular beam epitaxy or sputtering deposition. This nucleation density increases the smoothness of the deposited film. Since this technique allows a very accurate control of the thickness of the deposited film, PLD was used in this thesis to prepare both SRO and BTO layers. In Figure 2.28, a transmission electron microscopy (TEM) cross-section image of a heterostructure formed by a SRO film (used as an electrode) on top of a FE BTO film is shown. This image was recorded on a SRO/BTO/SRO//STO heterostructure grown by PLD. This shows that the SRO growth on top of the BTO is coherent, with a very sharp electrode-ferroelectric interface.

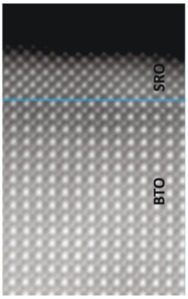

Figure 2.28 – *High Resolution TEM section of the top SRO/BTO interface of a studied sample, grown by PLD.*

Reflection high-energy electron diffraction (RHEED) [165] makes it possible to follow the nucleation and growth of these PLD SRO films during the film growth. Figure 2.29 shows a schematic of the RHEED system.

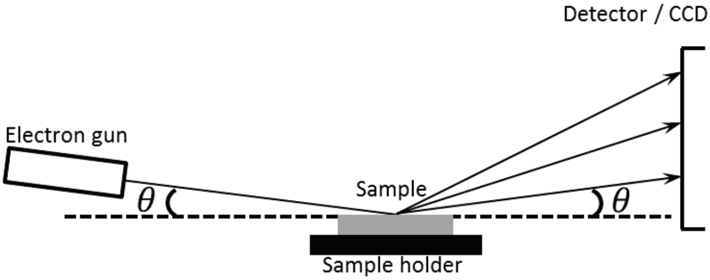

Figure 2.29 – *Systematic set up of the electron gun, sample and detector/CCD components of a RHEED system. Electrons follow the path indicated by the arrow and approach the sample at angle θ.*

The electron gun generates a beam of electrons striking the sample at a very small angle

θ relative to the sample surface. Incident electrons diffract from atoms at the surface of the sample: those diffracted electrons interfere constructively at specific angles and form regular patterns on a photoluminescent detector screen. They interfere according to the periodicity of atoms on the sample surface, so the diffraction pattern at the detector is a function of the sample surface. It is thus possible to characterize the crystallography of the sample surface through analysis of the diffraction patterns. An example of this diffraction pattern can be seen in Figure 2.30 a).

On a practical point of view, RHEED is a very popular technique for monitoring the growth of thin films. The intensities of individual spots on the RHEED pattern fluctuate in a periodic manner as a result of the relative surface coverage of the growing thin film. Figure 2.30 b) shows an example of the intensity fluctuating at a single RHEED point during growth. Each full period corresponds to formation of a single atomic layer thin film. The oscillation period is highly dependent on the material system, electron energy and incident angle, so researchers obtain empirical data to correlate the intensity oscillations and film coverage before using RHEED for monitoring film growth. Applied to our heterostructures, the use of RHEED gives us a better knowledge of the interfaces. Indeed, the (001) surface can exhibit either BaO or TiO_2 non reconstructed termination, in which barium has eight oxygen ligands compared to twelve in the bulk, and titanium is five-fold coordinated with oxygen anions compared to its six-fold coordination configuration in the bulk.

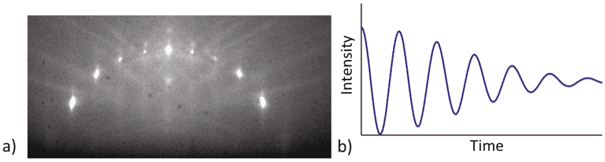

FIGURE 2.30 – *a) RHEED pattern obtained from electron diffraction from a clean* TiO_2*(110) surface. The bright spots indicate the diffraction peaks. b) Model of the fluctuation of the intensity of a single RHEED point during deposition. Each peak represents the forming of a new monolayer. The degree of order is at a maximum once a new monolayer has been formed. The spots in the diffraction pattern therefore have maximum intensity since the maximum number of diffraction centers of the new layer contribute to the diffracted beam.*

CHAPTER 3

Response of the electronic structure of a $SrRuO_3/BaTiO_3$ interface to an *in situ* applied bias voltage

One of the approaches to stabilize and/or even enhance ferroelectricity in nm-thick films has been suggested by first-principles calculations [166]. They predict that interface atomic structure and chemical bonding may significantly impact the initial ferroelectric state. In this perspective, pure metals which would appear to be the most logical choice for an electrode are often replaced with conducting metal oxides for ferroelectric thin-films, to reduce fatigue in the devices and enhance the screening.

Both electronic properties and interface chemistry can affect the ferroelectric properties of a thin film. Using a combined Ginzburg-Landau based phenomenological model and first principles calculations, Tagantsev *et al.* [167] have studied the relative short-range (interface related) and long-range (electronic) contributions to the ferroelectric stability in SRO/BTO/SRO heterostructures. In the case of soft electrodes (*i.e.* allowing ionic distortion) such as conducting oxides, ionic off-centering in the electrode near the interface provides a screening mechanism [168] additional to the one from free charges in the electrodes. For this reason screening by a conducting oxide electrode can be very different from that of a noble metal. Black and Welser [169] suggested that the interface capacitance due to the SRO electrode is about four times larger than the one from a Pt electrode because of the higher dielectric constant of SRO. Thus, interface chemistry can influence the ferroelectric properties of the film, as ionic distortion and free charges in the electrode combine to screen the polarization charge. Understanding the interface electronic and chemical structure is therefore of prime importance in the elaboration and optimization of FE based electronic devices. This raises several questions. Is there electron spill-over from the electrode into the FE, as predicted by first principles calculations [166]? This spill-over would make the interface part of the BTO more metallic-like, but this may also be an artefact due to the small band gap values obtained using the local density approximation. Does the Schottky barrier height change significantly as a function of polarization state? Is there a modified electronic or chemical environment in the BTO next to the interface? Does phase separation, which might also modify the chemical environment at the interface in SRO [170], take place? In order to answer these questions, we have used a combination of HAXPES, TEM and electrical measurements to study the top electrode/FE interface of a SRO/BTO/SRO heterostructure. The polarization dependent band alignment and electronic structure of the top SRO/BTO interface of the SRO/BTO/SRO heterostructure were investigated using photoemission spectroscopy with *in situ* biasing.

3.1 Design of the studied heterostructure - main issues and their answers.

3.1.1 Sample design

In this section, we will describe the experimental issues at stake, such as allowing PES probing while applying *in situ* bias for the sample, and how the micro-fabrication was designed to answer these issues. The studied heterostructure was designed to be electrically connected. To conduct such experiments on metal/ferroelectric interfaces, several issues have to be tackled:

- The interface has to be as free of contamination and as sharp as possible. The best solution is the growth of the full structure in the same ultra-high vacuum chamber.

- The interface must not be too deeply buried so that the photoemission signal from the interface buried under the thin electrode is still significant. Using soft X-ray (∼1 keV), the probing depth is of 3-4 nm whereas hard X-ray (above 5 keV) can probe 10-20 nm.

- The capacitor area must not be too small so that the photoemission signal comes only from the interface of interest. The size of the capacitor will thus have to be at least equal to the beam spot size on the sample (typically in the order of $\sim(100 \times 100)\ \mu\text{m}^2$)

- The capacitor area must not be too large so that leakage currents due to defects are minimized. Indeed leakage is known to increase with the capacitor size, so we have to keep the latter at its minimum, while still fulfilling the previous requirement.

- The electrical connections must be compatible with an ultra-high vacuum (UHV) environment in terms of vacuum contamination. The sample manipulation must also remain possible under UHV conditions.

The heterostructure has been designed according to those constraints. The heterostructure is a BTO thin film, with a bottom electrode of SRO deposited onto a STO substrate, and a set of several SRO top electrodes. SRO is chosen since it can epitaxially grow on BTO and it provides screening via free carriers charges and via ionic displacements. Similar samples were also prepared for the studies presented in chapter 4.

The two first issues have been resolved by growing the full heterostructure in a unique deposition chamber. For the SRO/BTO/SRO capacitors the top electrodes thicknesses are 2 nm. These electrodes are much thinner than the probing depth of 10-20 nm, accessible in hard X-ray photoemission spectroscopy.

To address the issues of biased photoemission, the metal/ferroelectric/metal structure, has to be carefully designed. The starting point is a (5×5) mm^2, planar sample. In photoemission spectroscopy, signal from small areas can be measured by using a small beam spot focused on the region of interest. At a synchrotron facility, such as SOLEIL, several beamlines offer photoemission end-stations with beam spots of width of $\sim(100 \times 100)$ μm^2. This is the case for the GALAXIES beamline. Therefore, by adding a margin of error which takes into account the tail of the beam, we chose (300×300) μm^2 as the area of a capacitor. With such large electrodes, it is likely that defects inducing high leakage current, for example high conduction channels through grain boundaries, occur randomly for some capacitors. This is the reason why we chose to fabricate twenty independent capacitors per sample to ensure that at least some of them have a low enough defect concentration for FE stability.

Once this dimension problem is settled, the next step is to design a system which can be electrically connected to different ultra-high vacuum manipulators and is suitable for photoemission spectroscopy. The final design is presented in Figure 3.1, with a schematic side view of the device.

Experiments are performed using HAXPES. Therefore, the thickness of the top electrode cannot exceed 10 nm if we want a sufficient signal to noise ratio from the buried interface. In fact, the top electrode prepared was chosen even thinner, and provided continuous conductive films. These thin top electrodes cannot hold any wire and an intermediate stage has been designed to allow an easy connection. This has been done by the deposition of a thicker layer of metal, overlapping a small part of the top electrodes, which will serve as a connecting pad. It can then be connected by micro-wiring to the sample holder. Moreover, the metal pad has to be electrically separated from the ferroelectric layer to avoid disturbing the electrical properties of

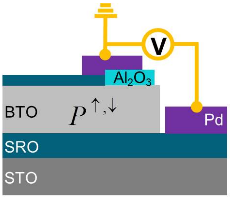

FIGURE 3.1 – *Schematic side view of the connected SRO/BTO/SRO heterostructure.*

the capacitor. This is the last feature of the design: an intermediate, highly insulating, dielectric layer is inserted between the pad and the ferroelectric to limit, at best, parasitic behaviors. The pad is 300 nm thick and made of palladium because of its good conduction properties and excellent compatibility with micro-wiring. The intermediate dielectric is 100 nm thick and made of Al_2O_3 because of its highly insulating properties.

The sample was prepared in the Institut d'Electronique Fondamentale, Orsay (France). The three layers of SRO (2 nm), BTO (60 nm) and then SRO (35 nm) thin films were grown on a $SrTiO_3$ (001) (STO) substrate using PLD. Prior to film growth, the STO substrate was cleaned using buffered HF solution and rinsed in deionized H_2O, followed by annealing under oxygen atmosphere to obtain a clean, atomically flat, TiO_2 terminated, STO surface [171].

To perform *in situ* bias studies, both the top and the bottom electrodes need to be accessible to be connected, while ensuring proper isolation of the BTO from the connecting wire.

The full microfabrication of the sample consists of a series of several photolithography processes, and can be resumed in five mains steps presented in figure 3.2.

Step 1: This is the initial state of the lithography process. The layers of SRO, BTO and finally SRO were successively deposited by PLD.

Step 2: A first step of optic lithography was used to pattern the full electrode top layer in 20 identical (300 × 300) μm^2 pads. Photolithography, also termed optical or UV lithography, uses light to transfer a geometric pattern via a photomask to a light-sensitive chemical photoresist on the film. Then, a series of chemical treatments either engraves the exposure pattern into, or enables deposition of a new material in the desired pattern upon the material underneath the photo resist. Photolithography is used because it can create extremely small patterns (down

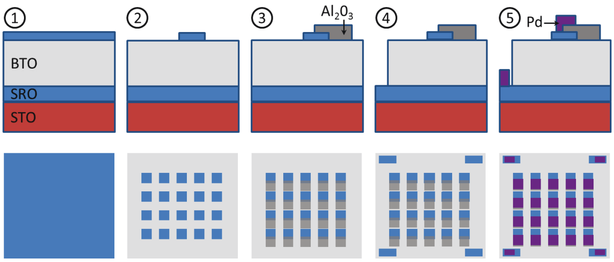

FIGURE 3.2 – *Side (top) and top (bottom) view of the sample throughout the 5 main steps of the lithography process used to prepare our heterostructure. The SRO top electrode (blue) is patterned to form 20 pads, then 20 pads of* Al_2O_3 *(dark grey) are added, and finally 24 pads of palladium (purple) are superposed to connect the sample.*

to a few tens of nanometers in size), and affords exact control over the shape and size of the objects it creates.

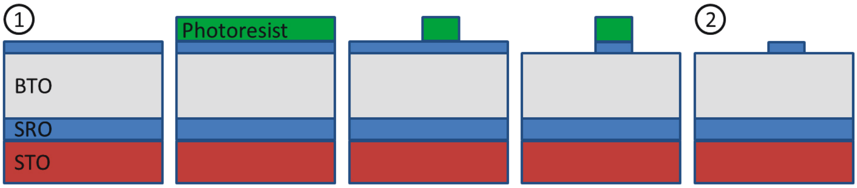

FIGURE 3.3 – *First step of the lithography process of the full heterostructure micro fabrication. Figures marked 1 and 2 correspond to the one presented in Figure 3.2.*

This first lithography step is detailed on figure 3.3. In this case, the wafer is covered with photoresist by spin coating (green on the figure 3.3 b)), producing a layer between 0.5 and 2.5 μm thick. The photo resist-coated wafer is then prebaked to drive off excess photoresist solvent. After prebaking, the photoresist is exposed to a pattern of intense light. The exposure to light causes a chemical change that allows some of the photoresist to be removed by a special solution, called "developer" by analogy with photographic developer (figure 3.3 c)). We used positive photoresist which becomes soluble in the developer when exposed, with a mask where only the regions for 20 pads were exposed. The resulting wafer is then "hard-baked" to solidify the remaining photoresist, to make a more durable protecting layer during the etching. In etching, the SRO is removed in the areas that are not protected by photoresist (figure 3.3 d)).

Finally, a solvent, or resist stripper, is used to remove the remaining photoresist (figure 3.3 e)). The result of this lithography was thus 20 electrode pads, as we can see on the step 2 of Figure 3.2.

Step 3: Using a second optical lithography process, a set of 20 Al_2O_3 pads was deposited over the top electrodes. Each Al_2O_3 pad is overlapping its corresponding top electrode pad over 5 μm. This step will provide an electrical isolation between the BTO and the palladium pads deposited in the step 5. Al_2O_3 was thus deposited on top of the all sample and a lithography process identical to the one performed in Step 2 was used to pattern it.

Step 4: To electrically connect the sample, this latter layer was etched in order to give access to the bottom electrode on each of the four corners of the sample. To do so, we performed a lithography using negative photoresist making unexposed regions soluble in the developer. The principle is the same as in step 2, with the difference that the resist will be activated on the whole surface except on the 4 corners of the sample. We then etched the sample through the BTO to access the bottom SRO before removing the remaining resist.

Step 5: A fourth and final step of lithography with positive resist was performed to deposit the palladium. Similarly as in step 2 and 3, we evaporated palladium onto the entire surface of the sample and used lithography to shape this layer into the desired pattern. As a result, a set of 20 palladium pads was deposited over the Al_2O_3 and the top electrodes, with an additional 4 pads over the four accesses to the bottom electrode in the corners of the sample. Each palladium pad is overlapping its corresponding SRO electrode over 5 μm (*i.e.* it is overlapping the Al_2O_3 by 10 μm). This way, it allows electrical contact while remaining isolated from the BTO. Moreover, this configuration leaves most of the surface of the electrode free to perform XPS on the electrode and on the BTO below, without probing the Pd or the Al_2O_3.

Figure 3.4 shows a top view of the micro-fabrication mask used for those 5 steps. The position of the 20 SRO top electrodes are presented in blue, and the four additional rectangular patterns in the corner used to connect the bottom electrode in pink. The overlapping Pd pads used for connexion are green on the picture. The mask also presents the lithography alignment marks - the crosses near the edge of the sample - used to properly align the mask for each lithography step.

Finally, each one of the top/bottom electrode pairs was electrically tested (as presented in section 3.1.2). The pad which has shown the best electrical response was connected to the sample holder using gold micro-wiring. Figure 3.5 shows a top view of the connected sample as a) a simplified schematic and b) a photography. On the photography, we can clearly distinguish

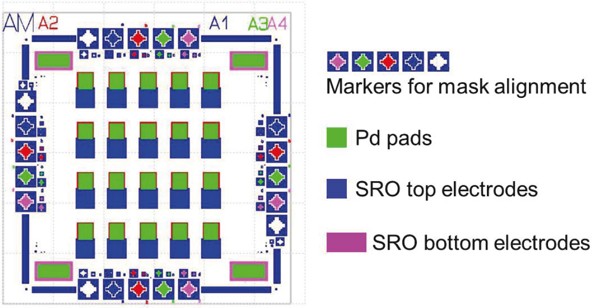

FIGURE 3.4 – *Top view of the mask used during the lithography steps of the micro-fabrication.*

the 20 SRO top electrodes and the 4 accesses to the bottom electrode on the corners of the sample. On the connected pad (bottom right of the sample), we can also see the gold wire going outside of the sample, towards the sample holder, where it was connected to the voltage supply.

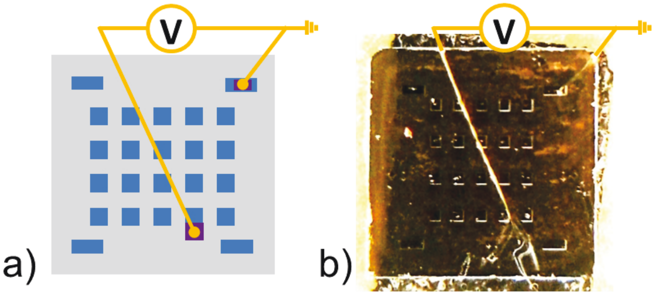

FIGURE 3.5 – *a) Simplified schematic and b) photography of the connected SRO/BTO/SRO heterostructure.*

3.1.2 Electrical characterization of the $SrRuO_3/BaTiO_3/SrRuO_3$ heterostructure.

a) Electrical characterization

We performed *in situ* electrical characterization of the connected sample, to verify the FE character of the sample, and to access the coercive voltages. The accurate measurement of these values is extremely important for applying *in situ* the correct bias voltages during the HAXPES measurements. Before subjecting the sample to the hard X-ray beam, we measured the capacitance of the system as a function of the applied voltage (C-V loop), and the obtained C-V curve is presented in Figure 3.6.

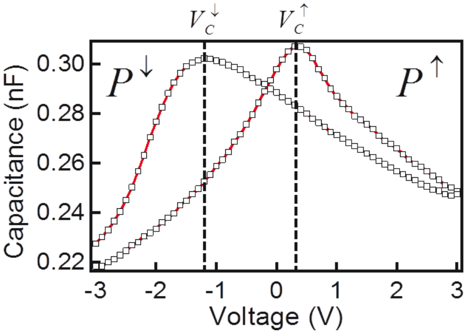

FIGURE 3.6 – *C-V butterfly characteristic of a FE capacitor.* $P^{\uparrow}$ *is obtained by applying a positive voltage to the bottom electrode. The coercive voltages needed to switch the polarization* $V{-}C^{\downarrow}$ *and* $V{-}C^{\uparrow}$ *are marked by dashed lines.*

Figure 3.6 shows a C-V butterfly loop, characteristic of the switchable ferroelectric state of the capacitor. The coercive voltage needed to switch from $P^{\uparrow}$ to $P^{\downarrow}$ is $V_C^{\downarrow} = -\ 1.20$ V and $V_C^{\uparrow} = +\ 0.35$ V from $P^{\downarrow}$ to $P^{\uparrow}$. The C-V loop shows that the crossing of the two branches of the butterfly loop does not occur at zero bias, but with a $-$ 0.16 V offset from the expected value of 0 V for a perfect FE material. This means that the sample will have a tendency to be naturally in the $P^{\uparrow}$ state, *i.e.* that it demonstrates ferroelectric behavior with a weak built-in $P^{\uparrow}$ polarization. The used set up also allows performing I-V measurements.

The current density-voltage (I-V) is presented in Figure 3.7 a). The I-V curve was acquired from $P^{\downarrow}$ to $P^{\uparrow}$ as we sweep for current from -1 V to +1 V. Figure 3.7 b) displays a plot of $\ln I$ against $\sqrt{|V|}$ obtained from the figure 3.7 a). This corresponds to a switch from $P^{\downarrow}$ to $P^{\uparrow}$ polarization while measuring the current through the capacitor. The two branches for $V < 0$ and $V > 0$ are almost perfectly superposed, as we can see on the inset in Figure 3.7 b) showing a zoom of the curve for $\sqrt{|V|}$ between 0.5 and 1.0. In this range, we obtain a good linear fit of $\ln I = f(\sqrt{|V|})$ (in red in Fig. 3.7 b)) typical of Schottky thermionic emission [109]. The capacitor thus exhibits a Schottky-like behavior, *i.e.* it has a diode-like behavior for both positive and negative bias voltages. The I-V curve shows that capacitance leakage was low enough for the chosen electrode size

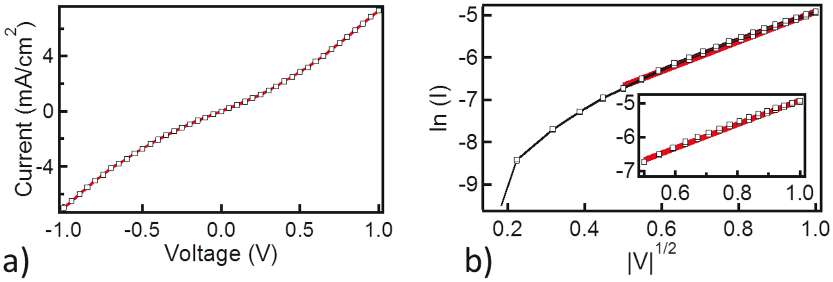

FIGURE 3.7 – *a) I-V characteristic showing nearly symmetric Schottky-like response b)* $\ln I$ *vs* $\sqrt{|V|}$ *fitted to a straight line typical of Schottky thermionic emission.*

of (300 × 300) μm^2.

b) Influence of the synchrotron beam X-ray induced reduction.

Since the incident high-energy photon beam and its high flux might affect the ferroelectric and conductivity properties of the heterostructure [34], we also did C-V measurements under X-ray illumination. A patterned SRO/BTO/SRO sample, identical to the one schematically described in figure 3.1 (the films have the same thicknesses), was introduced in the ultrahigh vacuum (10^{-9} mbar) HAXPES analysis chamber of the GALAXIES beamline. The photon energy was $h\nu$=6893.8 eV.

To check for an eventual destabilization of the FE state due to possible reduction under the X-ray beam, the sample was exposed to the beam and C-V curves were recorded every 10 minutes for 50 minutes, and after 4 hours of exposure. The resulting C-V curves are presented figure 3.8. All the C-V curves have similar shape and absolute values although a small diminution of the capacitance during exposure is observed. Indeed, the capacitance decreases with an increasing time of exposure to the beam, mainly between 20 and 30 min of exposure with a diminution of about 8% of the maximum value. Then, we can see a stabilization, with values of the capacitance almost identicals for the rest of the acquired C-V. This means that overall the properties of the FE films remain the same (no change of the coercive value and a diminution of the capacitance smaller than 10% at its maximum value) and that there is no noticeable change due to the photon flux exposure. Under these experimental conditions, the beam has no detrimental effect on the FE nature of the capacitor during 4 hours of irradiation.

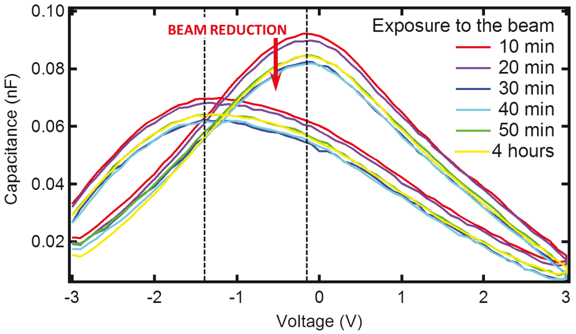

FIGURE 3.8 – *C-V butterfly of the FE capacitor recorded under beam exposition every 10 minutes for 50 minutes and after 4 hours (in yellow). The reduction due to the beam is traduced by a diminution of the capacitance, indicated by a red arrow. The values of the coercive field are marked by the two dotted lines.*

Systematic C-V recording allows us to deduce that the FE capacitor can resist the high photon flux for several hours, allowing to proceed to the HAXPES experiment. Indeed, as this test was performed under the same conditions (exposure duration, beam flux) as our experiments, on this time-scale, the experimental results will not be modified by a reduction of the capacitance of the heterostructure from the beam.

3.2 Hard X-ray experiments

3.2.1 Hard X-ray photoemission spectroscopy experiment on a full wafer

Static measurements were performed on a full wafer sample, as a first step of this HAXPES investigation. The software SESSA [141] was used to determine the photon energy set for the HAXPES experiments. It was chosen so that the IMFP is high enough to probe below the SRO top electrode with good signal to noise ratio. The curve of the IMFP for Ba *4d* core level in BTO, already introduced in section 2.2, is presented again in Figure 3.9. From this curve, we can deduce that, at the chosen photon energy of 6893.8 eV, the IMFP value for the Ba *4d* core level in the studied heterostructure is 8.8 nm.

The SESSA software [141] was then used to simulate the expected spectra resulting from our heterostructure at different photon energies to verify the relative intensities of the different peaks. Figure 3.10 shows the simulated spectrum at the selected photon energy of 6893.8 eV (top), and the experimental survey spectrum (bottom). The simulation allowed us to verify

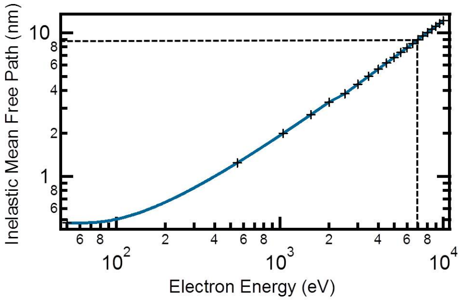

FIGURE 3.9 – *IMFP (nm) for the Ba 4d core level in BTO calculated for energies between 50 eV and 10 keV.*

the feasability of the measurement at the selected photon energy of 6893.8 eV, showing peaks from the buried interface with intensities high enough to be quantitatively analyzed. The two spectra (simulated and experimental) are very similar, both from the number of peaks present, and their relative intensity. The only exception is the O *1s* peak, higher in intensity in the measured spectra than in the simulated one. Indeed, the sample was exposed to air and shows some sign of C *1s* contamination. This is not an issue for our study, as we are probing the BTO below the top SRO interface where contamination should not happened, since the layers are all grown under controlled atmosphere in the same PLD chamber.

Preliminary experiments were conducted on a SRO/BTO/SRO full wafer sample, with a top SRO electrode of 8 nm, schematically described in Figure 3.11. HAXPES measurements were performed at different angles of detection, in order to distinguish eventual contributions of the SRO/BTO interface from the bulk.

The photon energy used was 6893.8 eV, calibrated using the Au *4f* core level spectrum of a gold reference sample (Figure 3.12). The two components from the spin orbit coupling, the Au $4f_{5/2}$ and the Au $4f_{7/2}$ can be observed. The latter is measured at a kinetic energy of 6809.8 eV. Knowing from the literature the binding energy of this core level to be 84.0 eV, we can calculate the photon energy to be 6893.8 eV.

Figure 3.13 shows the survey spectrum acquired on the grounded sample, *i.e.* both electrodes were grounded. The spectrum shows core level peaks characteristic of the SRO electrode and the BTO layers, confirming that the beam is well positioned on the SRO electrode. The low intensity of the C *1s* peak is proof of a low surface contamination of the sample. This implies a very weak attenuation of the photoemission signal, especially since carbon contamination should be absent at the interface, as previously explained. The inset shows a high resolution

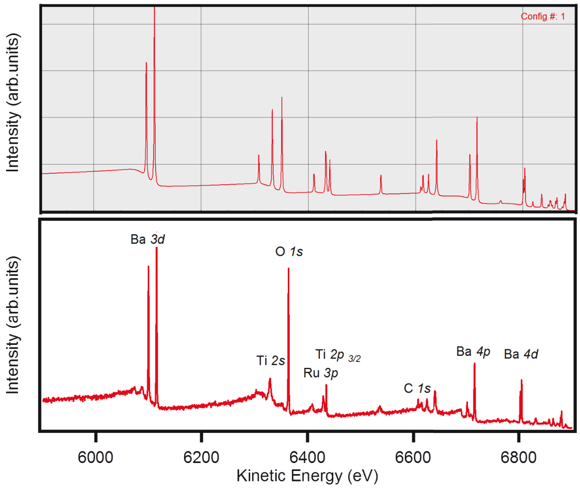

FIGURE 3.10 – *SESSA simulated (top) and measured (bottom) survey spectra for the SRO/BTO/SRO interface using photon energies of 6893.8 eV.*

scan of the Fermi level region. The sharp edge confirms the metallic-like character of the 5 nm SRO electrode.

The Ba $4d$ core-level spectra were measured, providing a unique signature of the BTO and the eventual BTO interface layer below the STO, as the barium only belongs to this layer. The Ba $4d$ spectra were fitted using pseudo-Voigt functions, with a ratio of 70% Gaussian to 30% Lorentzian. Figure 3.14 shows the steps of the peak fitting for the spectrum recorded with a low angle of detection (20°). On the top part of the figure, we can see the raw data marked by round shaped markers. In purple, is the background calculated using a Shirley algorithm [128]. After subtraction of the background, the spectrum is fitted using a combination of several pseudo-Voigt functions. The middle part of the figure shows the rough spectrum after subtraction of the background (still in round markers), and the four different peaks used to fit the spectrum. There are two couple of peaks in dark grey and light gray, each of them presenting the double contributions due to the spin-orbit splitting, identified as Ba $4d_{5/2}$ and Ba $4d_{3/2}$. We see that there are two contributions, one in dark grey (at higher binding energy (HBE)) and one in light grey (at lower binding energy (LBE)). The full width at half maximum (FWHM) of each peak is 0.8 eV. The energy separation between the Ba $4d_{5/2}$ and Ba $4d_{3/2}$ and their intensity ratio was imposed to be 2.6 eV and 1.5 respectively, according to the spin orbit splitting and branching ratio (as described in section 2.2.2). Finally, the bottom part of the figure shows the

FIGURE 3.11 – *Schematic of the full wafer sample.*

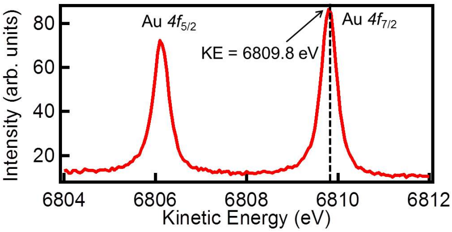

FIGURE 3.12 – *Au 4f core level spectra acquired on a gold reference sample. The Au $4f_{7/2}$ is measured at a Kinetic Energy of 6809.8 eV.*

resulting fit (blue line) superimposed on the rough spectra after background subtraction (round markers) and the different peaks (filled in dark and light grey). The former is the sum of each peak and is adjusted to follow the shape of the rough spectra. The red spectrum corresponds to the residual, *i.e.* the difference between the raw data and the best fit. This difference is very low, in the same order of magnitude as the noise of the spectra, confirming the quality of the resulting fit.

Figure 3.15 shows the Ba *4d* core-level spectra obtained for different emission angles (20°, 45°, 60°) with respect to the surface normal. The measurement with a low angle of detection (20°) corresponds to a bulk sensitive analysis, whereas with a large angle of detection (60°), the majority of electrons detected are emitted from the topmost surface of the sample.

The spectra for the three angles of detection (20°, 45° and 60°) were fitted following this procedure. Figure 3.15 shows the best fits for the three different angle of emission (20° on the top part of the figure, 45° on the middle, and 60° on the bottom part of the figure). The energy position of the two components (dark grey and light grey) and their relative intensities are presented in table 3.1 for the three spectra. Only the Ba $4d_{5/2}$ contributions are presented as the information is similar for the Ba $4d_{3/2}$ peak. The dark grey component's intensity increases

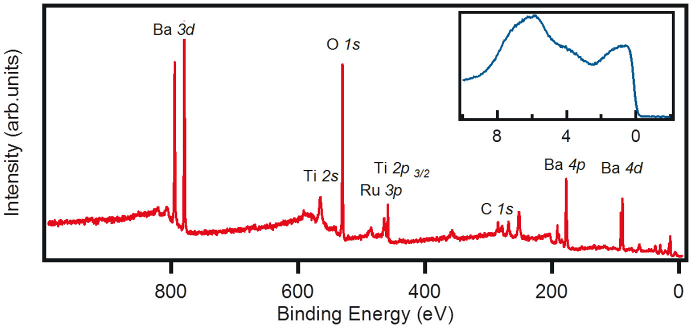

Figure 3.13 – *HAXPES survey spectrum showing core level peaks, characteristic of the SRO electrode and of the BTO. The binding energy scale was calibrated using the Au reference sample. The inset is a scan close to the Fermi level region showing the sharp metallic Fermi edge at zero binding energy.*

with the angle of detection, *i.e.* with the sensitivity to the surface, with respect to the light grey components. As explained previsouly in section 2.2.3, where is described the connection between the angle of detection and the origin of the electrons in the sample, the dark grey component at HBE is therefore attributed to the topmost surface of the sample, *i.e.* to the SRO/BTO interface.

Angle of detection	Bulk (LBE)		Interface (HBE)	
	BE (eV)	Relative Intensity	Be (eV)	Relative Intensity
20°	88.35	0.63	89.52	0.37
45°	88.34	0.49	89.67	0.51
60°	88.36	0.35	89.59	0.65

Table 3.1 – *Binding energy (eV) and relative intensity of the Ba* $4d_{5/2}$ *bulk and interface contributions (the sum of both bulk and interface contributions is fixed to 1) for the three angles of detection 20°, 45°and 60°.*

The analysis of the full-wafer sample allowed us to relate a HBE component in the Ba *4d* spectra to a contribution from the SRO/BTO interface of the capacitor. For the HAXPES measurements, a patterned sample with smaller top electrodes was used to limit the possibility of leakage current that would disrupt the experiment. The sample is a SRO(2 nm)/BTO/SRO/STO heterostructure schematically represented in figure 3.1, similar to the one on which fatigue tests were performed (section 3.1.2.b).

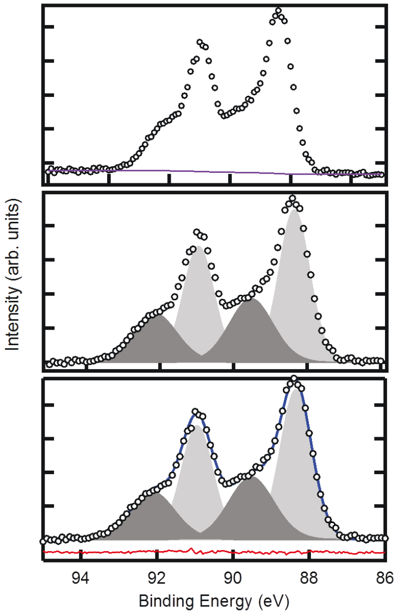

FIGURE 3.14 – *Peak fitting steps for the Ba 4d core level spectra acquired at a 20° angle of detection. It shows on three graphs the raw data (round markers) along with: on the top graph the Shirley background (purple); on the middle graph the different peak used for the peak fitting (filled in light and dark grey), on the bottom graph the resulting best fit (blue) and the residual spectra (red).*

3.2.2 Description of the operando experimental conditions

The size of electrodes (300 × 300) μm^2 has been designed to be significantly larger than the spot size of the GALAXIES beamline. The beam spot of (100 × 100) μm^2, three times smaller than the electrodes, can therefore be entirely positioned on the capacitor excluding totally the surrounding region. In order to locate the wired SRO top electrode, the sample was mapped by moving the sample while measuring the Sr *2p* photoemission spectrum. From the map, the position of the palladium pads can easily be observed. Mapping the full sample is time-consuming, so the acquisition was stopped as soon as the capacitor was located. As described in section 3.2.1, we used a photon energy of 6893.8 eV where the IMFP of Ba *4d* is high enough (8.8 nm) to probe the buried interface, below the 2 nm thick top electrode, with a good statistics. The overall energy resolution was of 250 meV and the photoemission detection angle was 45° with respect to the surface normal.

Figure 3.16 shows typical hysteresis FE loop. In order to study the polarization dependent

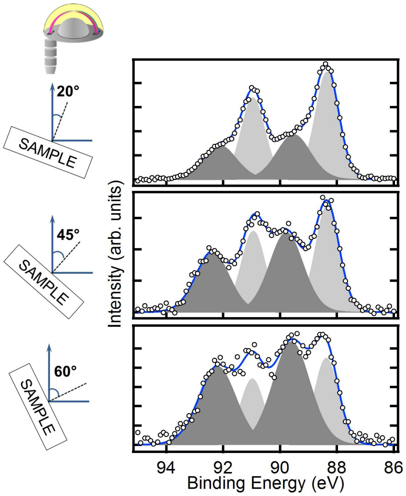

Figure 3.15 – *Ba 4d core level spectra and their peak fitting acquired for three different angle of detection: 20°, 45° and 60° with respect to the normal of the sample surface.*

band alignment and electronic structure of the SRO/BTO top interface, we made 4 series of measurements along the polarization loop, marked by dots. Measurements were made at saturation (plain dots), *i.e.* when the sample is under bias, and at remanence (empty dots), *i.e.* when the sample is polarized but under zero bias. In each case, spectra were recorded for both $P^{\uparrow}$ and $P^{\downarrow}$ polarization states giving a total of 4 measurement series. For the saturation measurements, the bottom electrode was biased with respect to the top electrode which was maintained at sample ground. To ensure that the device is fully switched, we applied voltages greater than the coercive values, *i.e.* of ± 3 V, for 1 minute. Then, we decreased the voltage applied to ± 1.1 V on the capacitor in order to limit the current leakage whilst remaining at polarization values near saturation. For the remanence measurement, we used the same voltages of ± 3 V for 20 seconds to fully switch the FE state, but measured the spectra with zero bias. In this case, the top and bottom electrodes were short-circuited. For all measurements, bias was applied on the bottom electrode in order to allow direct measurement of the energy response to the voltage pulse. It was showed in Ref. [25] that applying bias on the top or bottom electrode does not change the binding-energy shifts significantly. Ba *3d*, Ba *4d*, Ti $2p_{3/2}$ and Sr $2p_{3/2}$ core-level spectra were acquired for each polarization states. Overall, during these measurements (including HAXPES measurements and preliminary electrical characterization), the sample was switched ~100 times. Such a capacitor is expected to exhibit sign of fatigue after 10^6 to 10^9

switches from one polarization state to the other [172]. Fatigue is thus not expected to influence our experiments.

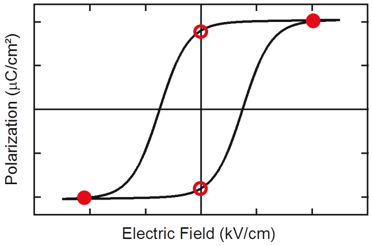

FIGURE 3.16 – *Schematic of a typical hysteresis P(E) loop of a FE material. Measurements are made in saturation (full red dots), and in remanence (empty red dots).*

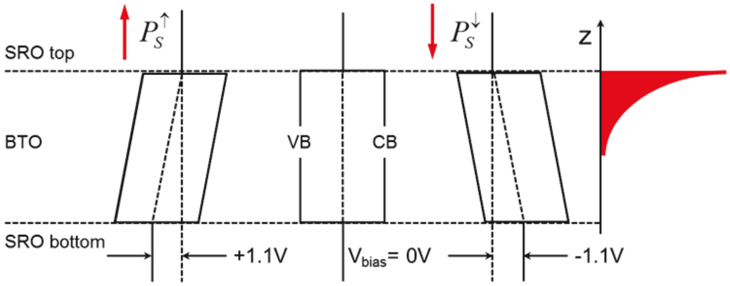

FIGURE 3.17 – *Band skewing due to the applied voltage for saturation measurements, for +1.1 V; 0 V and -1.1 V. The emission intensity as a function of depth is indicated by the red exponential decay on the right.*

The *in situ* applied voltage results in a potential gradient across the BTO, shifting the intensity distribution as a function of binding energy as shown in Figure 3.17. This is a first linear approximation [173]. Any departure from this behavior can therefore be attributed directly to the interface polarization. The deeper in the BTO, the larger the shift will be, with respect to the same emission from an unbiased sample. Conversely, the core level emission from the BTO at the interface with the top electrode at ground is almost unaffected by the applied bias. The attenuation due to inelastic scattering is visualized on the right hand side of Figure 3.17. Thus, parts of the core level shifts are due simply to the operando condition, creating a potential difference across the films. Both the shift and the attenuation as a function of emission depth are taken into account in the following data analysis.

Figure 3.18 shows Sr $2p_{3/2}$ spectra acquired in saturation regime for both $P^{\uparrow}$ and $P^{\downarrow}$ states. Both of them were fitted using a pseudo-Voigt function, after subtraction of a Shirley background. The FWHMs were found to be 2.2 eV. The BE of the peaks are 1938.97 eV for the $P^{\uparrow}$ state and 1939.24 eV for the $P^{\downarrow}$ state.

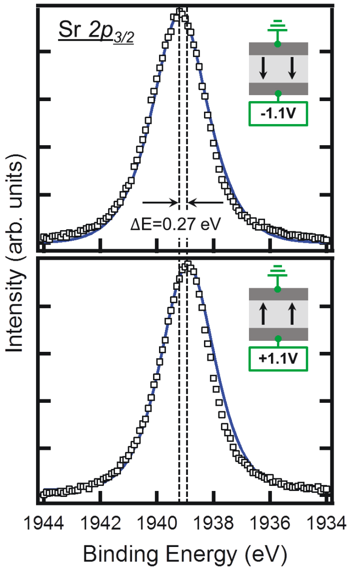

Figure 3.18 – *Sr $2p_{3/2}$ core level spectra acquired in saturation for both $P^{\uparrow}$ (bottom) and $P^{\downarrow}$ (top) polarization states. Vertical dotted lines indicate the energy of the intensity maximum for each peak, after peak fitting.*

With the bias applied to the bottom electrode, the Sr $2p_{3/2}$ core level spectrum was measured on the top electrode, at sample ground. Therefore, it should not shift under the applied bias. However, we can observe from the position of the Sr $2p_{3/2}$ peaks a shift of 0.27 eV between $P^{\uparrow}$ and $P^{\downarrow}$ polarization states. This is indicated on figure 3.18 by the dotted lines. We recall that the electrical contact on the top SRO electrode is done through a contact with a palladium pad (see Figure 3.1). The shift observed between the two Sr $2p_{3/2}$ peaks can be attributed to the parasitic resistance of the Pd-SRO contact. It has been subtracted from all saturation spectra presented in the following.

3.2.3 Results

The raw Ba $3d_{5/2}$, Ti $2p_{3/2}$ and Ba $4d$ core level spectra in the saturation regime are shown in Figure 3.19 for both $P^{\uparrow}$ and $P^{\downarrow}$ polarization states.

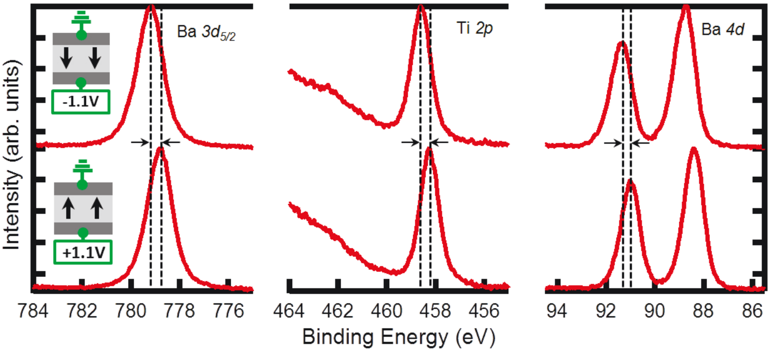

FIGURE 3.19 – *Ba $3d_{5/2}$, Ti $2p_{3/2}$ and Ba $4d$ core level spectra acquired in saturation for both $P^{\uparrow}$ (bottom) and $P^{\downarrow}$ (top). Vertical dotted lines indicate the shift in intensity maximum.*

A shift of ∼0.40 eV between both polarization states is observed for all of the measured core-level, as indicated by the dashed lines on the figure. This suggests that all of the three core-levels related to the BTO layer are affected in a similar way by the applied bias. A slight asymmetry of the peaks at higher binding energy (HBE) for both polarizations is noticeable for all measured core levels. However, following Figure 3.17, the applied bias should lead to an opposite asymmetry in the peaks for the two polarizations. This suggests that there is also a second component at higher binding energy. As previously showed in Figure 3.15, spectra measured as a function of the emission angle on a similar full wafer sample show that the HBE peak can be related to the interface between the BTO and the SRO top electrode, which might explain this constancy in asymmetry. The total lineshape is therefore due to the combination of the applied bias, the interface peak and the polarization effects.

Here we presented three different core levels. The titanium core levels are expected to be the ones most affected by a polarization switching, as the polarization in BTO is principally due to a displacement of the central Ti atoms with respect to the surrounding oxygen atoms. In ferroelectric BTO, the Born effective charge of the Ti ion is much greater than that of Ba [174]. However, we chose to focus mainly on the study of the Ba core levels. The first reason for this choice is that the Ti *2p* core level is difficult to analyse. Indeed, the Ti $2p_{3/2}$ peak (460.2 eV) partially overlaps with the Ru$3p_{3/2}$ peak, appearing at a very similar binding energy (461.4 eV), with a much higher intensity (as the Ru comes from the top electrode and thus is not attenuated). Moreover, the sample that we are studying consists of a BaO terminated BTO layer, increasing the weight of the Ba core levels, as the Ba atoms are located in the last layer at the interface with the top electrode.

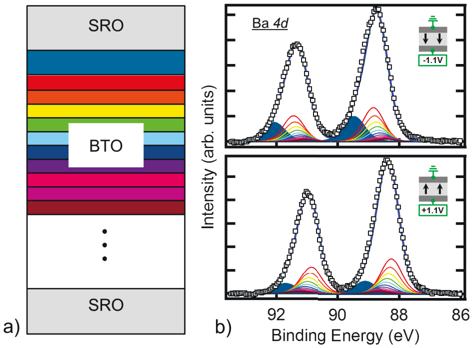

Figure 3.20 – *a) Schematic of the layered structure used to model the core level emission from the BTO. b) Ba 4d core level spectra in the* $P^{\uparrow}$ *(top) and* $P^{\downarrow}$ *(bottom) states in saturation. The corresponding fit is superimposed on the spectra: the bulk peaks (rainbow colored lines), the interface (plain blue) and the resulting fit (black empty squares).*

Figure 3.20 shows the fitted Ba *4d* spectra in saturation b) for both $P^{\uparrow}$ and $P^{\downarrow}$ polarization states. The spectra were fitted using pseudo-Voigt functions, after subtraction of a Shirley background. The fits include the gradient induced by the applied bias on the SRO/BTO structure. The modelling of the BTO by 11 bulk layers, and an additional interface layer on the top, is schematically represented in Figure 3.20 a). A first layer (in dark blue on the figure 3.20 b)) represents the interface, *i.e.* the top most unit cells (u.c.) of the BTO, whose thickness is unknown. Below the interface, we have the bulk BTO, modeled by eleven layers all 5 u.c. (2.4 nm)-thick, named Bulk_1 to Bulk_{11}, and an additional layer representing the rest of the BTO (10 nm thick). To simulate the effect of the potential gradient due to the applied bias, we assume that the bulk binding energy varies linearly with depth. The intensity of each bulk peak is attenuated by $e^{-z/\lambda}$ where λ is the inelastic mean free path, estimated at 8.8 nm at this photon energy, and z is the depth of the considered layer. For this reason, the position in energy and the intensity of the layers Bulk_2 to Bulk_{11} can be expressed as a function of Bulk_1, as described in table 3.2.

Layer	z position below the interface (nm)	Energy shift (eV)	Intensity attenuation
Bulk_1	0	0	1
Bulk_2	2.4	0.044	0.761
Bulk_3	4.8	0.088	0.580
Bulk_4	7.2	0.132	0.441
Bulk_5	9.6	0.176	0.336
Bulk_6	12.0	0.220	0.256
Bulk_7	14.4	0.264	0.195
Bulk_8	16.8	0.308	0.148
Bulk_9	19.2	0.352	0.113
Bulk_{10}	21.6	0.396	0.086
Bulk_{11}	24.0	0.440	0.0653

TABLE 3.2 – *Energy shift and intensity attenuation of the bulk layers used to model the Ba 4d peak fitting as a function of the bias applied to the capacitor for the saturation measurement.*

Each layer, simulated by a peak, was fitted by a pseudo-Voigt function. The FWHM was fixed at 0.8 eV, the value found for the full wafer sample, recorded in the exact same conditions (energy resolution, photon energy). Therefore, there are only two free parameters left: the binding energy shift between the interface and the first bulk layer (Bulk_1) and the interface/bulk intensity ratio, in other words the thickness of the interface.

Table 3.3 gives the parameters obtained from peak fitting for the interface and the first bulk peak, *i.e.* the binding energy of the peaks, and their relative intensity. To calculate the relative intensity, the sum of all the peaks' intensities is set equal to 1, and the intensity of the interface peak and of the sum of the bulk peaks are calculated accordingly. The resulting fit almost perfectly describes the raw spectra, validating the used model as a first approximation.

In saturation, the interface peak is shifted by 0.85 (0.64) eV with respect to the bulk for $P^{\uparrow}$ ($P^{\downarrow}$) polarizations, showing that the Ba atoms at the interface have a different chemical environment than the ones in the bulk. This is a proof of the influence of the SRO electrode on the top most layer of the BTO. The different value of this shift between the two polarization states (also supported by the fact that the interface peak shifts by 0.37 eV between $P^{\uparrow}$ and $P^{\downarrow}$) shows that the interface electronic environment differs for the two polarization states. These results are in agreement with first principles calculations performed by Lu *et al.* [175]. In their paper, they show that in the proximity of the interface the rumpling is maintained thanks to the ionic distortions in the SRO electrode. However, the rumpling magnitude is not the same for $P^{\uparrow}$ and $P^{\downarrow}$, nor is the penetration of ionic distortion into the SRO. This means that the

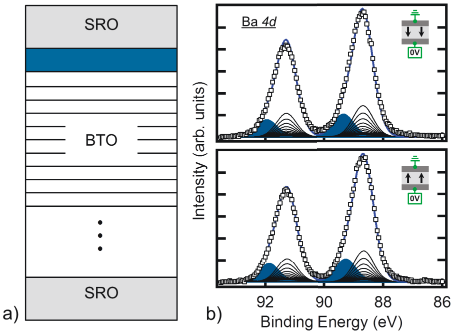

Figure 3.21 – *a) Schematic of the layered structure used to model the core level emission from the BTO. b) Ba 4d core level spectra in the* $P^{\uparrow}$ *(top) and* $P^{\downarrow}$ *(bottom) states in remanence. The corresponding fit is superimposed on the spectra: the bulk peaks (black lines), the interface (plain blue) and the resulting fit (black empty squares).*

local electronic and chemical environment of the Ba at the interface is therefore different for $P^{\uparrow}$ and $P^{\downarrow}$ states.

The same peak fitting was applied to the remanence measurement, but with no shift between the different bulk layers (as there is no bias applied to the sample), in order to properly compare the two sets of results. Figure 3.21 shows the fitted Ba *4d* spectra in remanence b) for both $P^{\uparrow}$ and $P^{\downarrow}$ polarization states. The 11 bulk peaks are reduced in fact to a single peak. Again there are only two free parameters. This time the bulk peaks, all at zero bias are all represented by a black line, similarly as on the schematic of the heterostructure in Figure 3.21 a). At remanence, spectra for the $P^{\uparrow}$ and $P^{\downarrow}$ polarization states are almost identical. This can be attributed to the tendency of the sample to be in the $P^{\uparrow}$ state, *i.e.* it has a built-in $P^{\uparrow}$ polarization, as seen from the C-V curve presented in Figure 3.6. The interface peak is also shifted with respect to the bulk peak by 0.61 (0.66) eV for $P^{\uparrow}$ ($P^{\downarrow}$) polarizations at remanence, meaning a different chemical environment at the interface than in the bulk. However, the bulk to interface shift is 0.08 eV between $P^{\uparrow}$ and $P^{\downarrow}$ states at remanence compared to 0.37 eV at saturation. This suggests that the distinct interface environment observed in saturation is due to the applied voltage maintaining the polarization state. At remanence however, the shift is smaller, *i.e.* there appears to be partial relaxation of the polarization of the interface layer.

Using the formula 2.24, the relative intensities of the bulk and interface peak component were used to calculate the thickness of the BTO interface region for each polarization state. Given the value presented in table 1, we obtain 1.3 u.c. for the $P^{\uparrow}$ and 2.6 u.c. for the $P^{\downarrow}$ polari-

Polarization state		Bulk (LBE)		Interface (HBE)		Core level shift (eV)	
		BE (eV)	Relative Intensity	BE (eV)	Relative Intensity	Bulk	Interface
Saturation	P$^{\uparrow}$	88.26	0.92	89.11	0.08	0.58	0.37
	P$^{\downarrow}$	88.84	0.84	89.48	0.16		
Remanence	P$^{\uparrow}$	88.66	0.85	89.27	0.15	0.02	0.08
	P$^{\downarrow}$	88.68	0.85	89.34	0.15		

TABLE 3.3 – *Binding energy (eV) and relative intensity of fits to bulk and interface Ba 4d$_{5/2}$ core level spectra (the sum of both bulk and interface contribution is fixed to 1) in remanence and in saturation.*

zation states, *i.e.* 0.53 and 1.05 nm, respectively. These values are in good agreement with the ones found by first principle calculation by Lu *et al.*, confirming the hypothesis of a distortion localized in about 1-3 unit cells in the BTO.

Band line-up: Further insight into the origin of the capacitor properties lies in the electronic band line-up of the SRO/BTO interface that can be accessed by calculating the valence band offset. The HAXPES results reveal the existence of a layer located at the SRO/BTO interface inside the BTO, which behavior differs from that of the bulk. We can expect that there will be a difference in the band position at this interface layer with respect to the bulk. Most analyses of band alignment at a FE/electrode interface assume rigid band shifts for all levels, as in classical semiconductor physics introduced by Kraut *et al.* [176]. The valence band offset (VBO) at the top interface can be calculated as follows:

$$E_{VBO} = (BE_{Ba4d} - BE_{Sr2p})_{film} + (BE_{Sr2p})_{pad} - (BE_{Ba4d} - BE_{VB})_{bulk} \tag{3.1}$$

The first term is obtained from the experimental data: the values for BE$_{Ba4d}$ can be found in table 3.3. The binding energy for the Sr *2p*$_{5/2}$, BE$_{Sr2p}$, is 1938.97 eV (1939.24 eV) for P$^{\uparrow}$ (P$^{\downarrow}$). The second term was directly measured on a SRO pad of the sample; its binding energy is 1939.10 eV. Finally, the third term is the difference between the maximum of the Valence Band and the Ba *4d* peak (87.40 eV) and was measured on a BTO monocrystal during a previous experiment. The C-V and I-V electrical characterization of the capacitor shown in section 3.1.2 exhibit a Schottky behavior of the capacitor. Using the binding energy of the Ba *4d* interface peak for the first term and assuming that the BTO has a band gap of 3.2 eV [177], we calculate a Schottky Barrier Height (SBH) for electrons of 2.75 (2.15) eV for the P$^{\uparrow}$ (P$^{\downarrow}$) in saturation and 2.34 (2.32) eV for the P$^{\uparrow}$ (P$^{\downarrow}$) in remanence. The resulting band line-up can be sketched, as shown in figure 3.22.

Values of the calculated SBH are high enough to be consistent with a Schottky contact at the

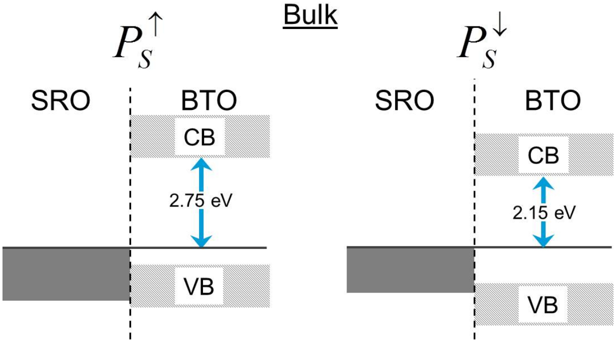

FIGURE 3.22 – *Schottky barrier height for electrons deduced from the experimental HAXPES results for the* $P^{\uparrow}$ *and* $P^{\downarrow}$ *polarization states at saturation, assuming a band gap of 3.20 eV. The SBH is calculated using the bulk peak component of the Ba 4d.*

top interface. The residual internal field can be estimated, assuming that the SBH difference for $P^{\uparrow}$ and $P^{\downarrow}$ at remanence is equal to the potential drop across the BTO. This seems to confirm the high screening efficiency obtained by free charges from the metallic oxide electrode.

We use the equation for Schottky emission to compare more quantitatively the barrier height as deduced from the I-V characteristic with that measured by HAXPES. The current density in the case of thermionic emission is [109, 178]:

$$J = A^* T^2 \exp -\frac{q}{kT}(\varphi_0 - \sqrt{\frac{eE_m}{4\pi\varepsilon_0\varepsilon_{op}}}) \tag{3.2}$$

where A^* is Richardson's constant; T, the temperature; q, the electron charge; k, Boltzmann's constant; φ_0 the potential barrier at zero voltage; E_m the maximum electric field at the interface; ε_0 the permittivity of the free space and ε_{op} the high-frequency dielectric constant. For sufficiently large applied voltages this equation provides a straight line with the y-axis intercept

$$b = \ln A^* T^2 - \varphi_0 \frac{q}{kT} \tag{3.3}$$

Richardson's constant can be calculated from:

$$A^* = \frac{A\pi m k^2 q}{h^2} \tag{3.4}$$

where m is the effective mass and h Planck's constant. For an effective mass four times the electron mass [179, 180], we estimate a SBH of 1.36 eV at zero bias. The difference with respect to HAXPES determined values of 1.96-1.98 eV may be ascribed to the approximations used in the model for thermionic emission, in particular the electric field at the barrier which can be polarization dependent and which will increase the value of the barrier height as estimated from the Schottky equation [109]. However, in our case, the film is too thick for the electron transport to be expressed by these equations. It is thus necessary to do an $A(T)$ measurement. By measuring I-V curves while heating the sample, one can access the real value of the Richardson constant and accurately describe the electron transport in this ferroelectric. Those experiments are underway.

Calculating the band offset in the same way using the binding energy of the interface component of the Ba *4d*, we find a SBH for electrons of 2.08 (1.49) eV for the $P^{\uparrow}$ ($P^{\downarrow}$) at saturation. This situation is sketched in figure 3.23.

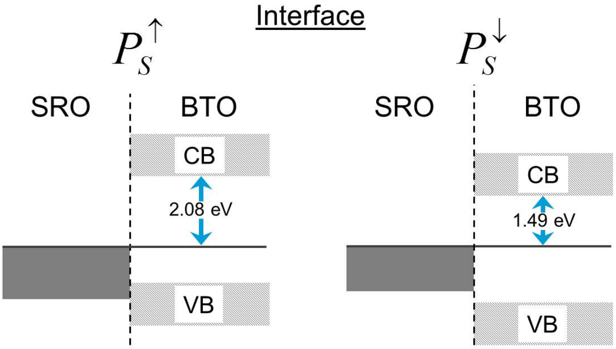

FIGURE 3.23 – *Schottky barrier height for electrons deduced from the experimental HAXPES results for the* $P^{\uparrow}$ *and* $P^{\downarrow}$ *polarization states at saturation, assuming a band gap of 3.20 eV. The SBH is calculated using the interface peak component of the Ba 4d.*

Equivalently, this valence band offset corresponds to a hole barrier of only 1,12 (1,71 eV) (assuming a band gap of 3.2 eV). However, hole mobility is much lower in BTO [181, 182] thus the electrical characteristics remain Schottky-like. Nevertheless, this does confirm the presence of an interface BTO layer with quite different electronic structures with respect to the bulk.

We now consider the eventuality of electron spill-over into the ferroelectric layer. In a MIM (metal-insulator-metal) capacitor with symmetric electrodes and a ferroelectric insulator, partial screening results in a net residual internal field, skewing the electron energy levels across the capacitor. This may be sufficiently important to start filling the conduction band of the FE, adjacent to the positively poled electrode. Electrons spilling over from the electrode would push the FE occupied electronic states away from the Fermi level, similar to doping in classical semiconductors. This should induce higher binding energies to $P^{\uparrow}$ polarized states. However, we observe the contrary, as shown on figure 3.20.

In the case of a hypothetical electron spill-over, such as schematized on the figure 3.24, electrons from the top electrode would be displaced into the BTO close to the interface, locally increasing the conductivity of the FE and virtually creating a thicker electrode.

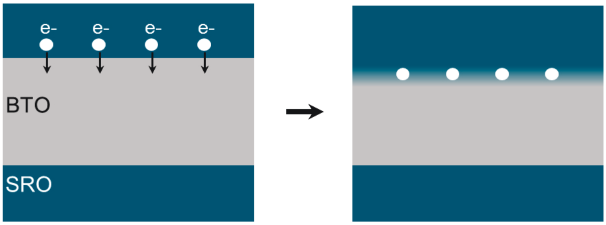

FIGURE 3.24 – *Schematization of the heterostructure in the case of electron spill over from the top electrode into the BTO. Free electrons from the top SRO electrode are migrating into the BTO, making the interface more conductive.*

The different results measured in our sample show no evidence for electron spill-over, neither in the core level shifts nor in the SBHs, although modulated by the polarization state. This supports the conclusion [166] that theoretical predictions of spill-over may be an artefact caused by an underestimation of the band gap in LDA. The value of the SBH calculated on our capacitor is more consistent with a screening of the polarization by free electrons and ionic displacements [36,169]. Stengel *et al.* used first principle calculations [36] to study the screening efficiency of SRO with respect to elemental metal electrodes. They concluded that screening is more efficient in this oxide electrode by both the accumulation of free electrons in the metallic/oxide and the ionic distortion taking place in SRO close to the interface. Their work is consistent with our results on the interface electronic structure.

TEM: In order to get further insight into the atomic organization at the interface, High-Resolution Transmission Electron Microscopy (HRTEM) experiments were performed after the operando HAXPES analysis. This technique allows a direct observation of atomic positions at metal/ferroelectric interfaces [183,184]. The sample has been measured in the $P^{\uparrow}$ state. To switch the sample in the $P^{\uparrow}$ state, it was poled using a bias of +3 V, and measurements were then made with no applied bias. A 100 nm thick specimen was prepared by focused ion beam milling using a FEI Strata FIB. Rough milling was performed using an operating voltage of 30 kV and the finishing step used 8 kV ions, as this provides a good compromise between minimizing the damage and having a good quality parallel-sided specimen. High angle annular dark field (HAADF) scanning transmission electron microscopy (STEM) images were then acquired using a probe corrected FEI Titan Themis operated at 200 kV.

BTO and SRO are both ABO_3 type perovskites; Ba is the A-site cation in BTO and Sr in SRO. B-site cations are Ti in BTO and Ru in SRO. Figure 3.25 a) shows the HAADF and Figure 3.25 c) the Annular Bright Field (ABF) of the BTO/SRO top interface. On the HAADF measurement, heavy atoms (Ba and Ru) appear with high intensity (bright dots), because of high scattering cross-section, whereas for the ABF image, they correspond to areas with less intensity (dark dots). In both images we can see a change in the crystallinity at about 2 nm below the surface dark area which corresponds to the interface between the SRO electrode above and the BTO below. HAADF and ABF-TEM images show that the SRO/BTO interface is well-defined and sharp. Thus, we can exclude the possibility, for example, that SrO segregates to the interface [170]. This configuration would create for the Ba *4d* a distinct chemical environment, which would be responsible for the HBE component in the Ba *4d* core-level.

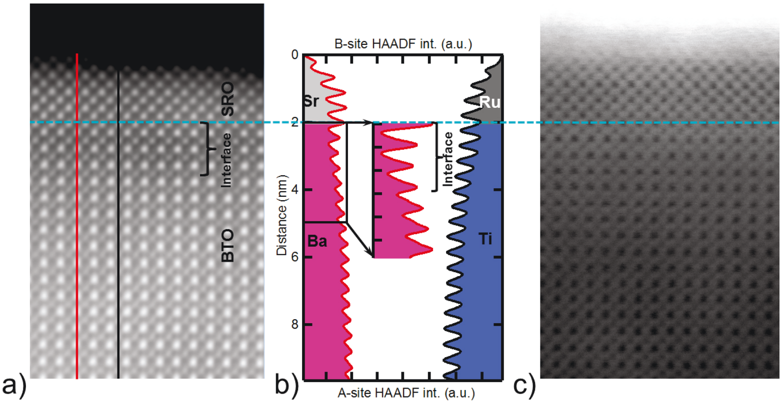

FIGURE 3.25 – *HAADF- and ABF-TEM observations for the SRO (2 nm)/BTO heterostructure and element characterization. a) High-resolution HAADF image. b) HAADF intensity profiles of A-site (left side) and B-site (right side) cations across the heterostructure, collected along the red and black lines in the HAADF image. c) ABF image taken from the same region as the HAADF image. The light blue line shows the top SRO/BTO interface.*

The HAADF intensity profiles of A-sites cations and B-site cations across the heterostructure are presented in Figure 3.25 b). A high intensity corresponds to the presence of an atom so the oscillations show the atomic positions. At a depth of 2.2 nm, a change in the A cation intensity shape is marked by a light blue dotted line. This corresponds to the interface between the SRO and the BTO. We can also see from the B-site cation intensity that this change occurs at a Ti atom position, proof that the BTO is TiO_2 terminated [185]. After this delimitation, the A-site cations intensity profile shows that there are 2-3 unit cells, *i.e.* 0.8-1.2 nm, on the BTO side of the interface which appear different from the bulk, regarding the general shape of the intensity profiles. The inset of Figure 3.25 b) is a zoom of the A-site cation profile over 2.5 nm below the interface. We can see on this zoom that after 2-3 unit cells below the interface, the shape of the profile for each A-site cation is different from just after the interface.

The intensity profiles have been fitted with Gaussian peaks and a polynomial background in order to extract the positions of the Ba and Ti atoms. Figure 3.26 a) shows the intensity profiles for both the titanium and barium atoms (in white square shaped markers). The Gaussian peaks used to trace the position of each atom are presented in red in the figure. Figure 3.26 b) presents the distance between two atoms for the Ba and Ti profiles, as a function of the depth z below the surface. The positions are fitted to a straight line. The distance between two atoms becomes smaller when approaching the interface and the unit cell dimension decreases from 0.462 nm in the bulk to 0.447 nm close to the interface, enlightening a difference in the ionic displacements in the interface region and in the BTO bulk.

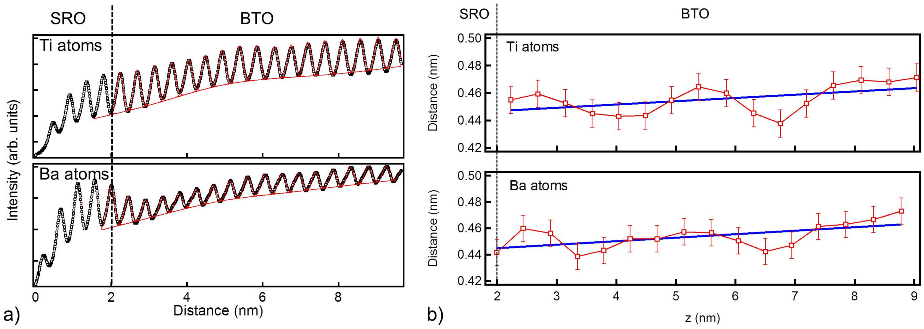

Figure 3.26 – *a) Intensity HRTEM profil for (top) the titanium and (bottom) barium atoms. The Gaussian peaks used to obtain the position of the atoms are in red. The SRO/BTO interface is marked by a dotted line. b) Distance between two atoms as a function of the depth below the surface of the capacitor extracted from the Ba HAADF profile (top) and the Ti HAADF profile (bottom), both fitted to a straight line.*

From the HAXPES measurement, we estimated an interface thickness of 1.3 u.c. for the $P^{\uparrow}$ polarization state. The HRTEM observation (showing a difference in the interface in atoms positions on about 2-3 u.c.) thus gives an interface thickness in the same order of magnitude as calculated from the photoemission characterization.

3.3 Conclusion and Discussion

The core level spectra at remanence are almost identical between the two polarization states, suggesting that the built-in upward polarization prevents us from observing the $P^{\downarrow}$ polarization state at remanence. To do so, new experiments would have to be performed with samples grown in order to lower, and if possible suppress, any polarization imprint. A complete absence of polarization imprint is very difficult to obtain, especially with SRO as both bottom and top electrode. However, growth tests can be made with different parameters (such as pressure and temperature for the layers depositions) until the minimal polarization imprint is obtained. After properly taking into account the effect of *in situ* bias, the saturation measurements show that 1.3 (2.6) unit cells of BTO are altered in the $P^{\uparrow}$ ($P^{\downarrow}$) at the SRO/BTO interface. Both HAXPES results and HR-TEM cross-section analysis support the hypothesis of atomic distortion propagating into the SRO. A SBH for electrons of 2.75 (2.15) eV is measured at saturation for the $P^{\uparrow}$ ($P^{\downarrow}$) polarization states, consistent with the macroscopic electrical characterization. There is no evidence for electron spill-over into the ferroelectric. At the interface however, the VBO is lowered to 2.08 (1.49) eV for the $P^{\uparrow}$ ($P^{\downarrow}$) polarization states. In the case of a fully screened polarization, we would observed a full ferroelectric distortion stabilized by a screening of the depolarizing field or the surface polarization charge. It seems that our results are more coherent with the existence of an interface layer in the capacitor, where the displacement of the Ti ions is smaller, leading to a decreased polarization. Only measurements in saturation show distinct electronic environments at the interface as a function of polarization. Operando experiments therefore appear invaluable in order to precisely measure the differences in the saturation/remanent interface electronic structure where leakage currents may play an important role.

These experimental results of the SRO/BTO interface with the thickness of the interface layer measured by TEM and HAXPES are in good agreement with first principles calculations of an asymmetric SRO/BTO/SRO stack [175]. In the latter, at the TiO_2/SrO interface the atomic displacements in the BTO reach the bulk value of the FE film after 2.5 unit cells (1.2 nm). The slightly thicker interface measured here might be due to the fact that the HAXPES analysis averages over (100×100) μm^2 (thus includes surface roughness) whereas first principles calculations and TEM focus on a single sharp interface. Lu also predicts that while the FE distortion propagates into the SRO side of the interface, there are modifications on the BTO side over several unit cells [175]. Although the effective Thomas-Fermi screening length due to free charge in SRO is predicted to be 0.2 Å [36], ionic distortion appears to penetrate several unit cells into the SRO electrode and is predicted to be responsible for the better dielectric response FE capacitors with oxide electrodes than with elemental metal electrodes [169]. Thus, experimental evidence is pointing to a combination of polarization dependent ionic distortion and free charge accumulation at the interface.

Chapter 4

Investigation of the polarization switching and fatigue in a $SrRuO_3/BaTiO_3/SrRuO_3$ heterostructure using time-resolved photoemission spectroscopy

In the previous chapter, we acquired crucial information on the polarization dependent changes of the interface electronic structure to polarization switching in a SRO/BTO/SRO heterostructure. The electrode/FE interface may also affect the switching kinetics of the polarization reversal process. For example, it has been suggested that local fields related to defects determine the switching time in $BiFeO_3$ capacitors [186]. At the electrode/FE interface, an accurate description of the switching process kinetics will allow to optimize switching times, voltages and understand the domain wall motion. Finally, it can help gaining further informations on the rate limiting switching process: the domain wall motion or the domain nucleation (see chapter 1).

A first time-resolved XPS study of the switching dynamics of a Pt/BTO/Nb:STO heterostructure was performed by the LENSIS team [25]. They determined that the FE/electrode interface exposed to a P.U.N.D. train of pulse can be modeled using a simple RC circuit with an additional series capacitance, as predicted by theory. In thin FE capacitors, this interface capacitance could even dominate the switching kinetics. As discussed in chapter 3, SRO used as an electrode provides screening via free carriers as well as via ionic displacements and we expect ionic relaxation at the SRO/BTO interface [186]. This could provide a different interface kinetics.

The aim of the experiment is to carry out an investigation of the kinetics of the SRO/BTO interface in response to polarization switching. To do so we rely on the fact that the dynamical response of the FE to switching and non-switching voltage pulses are not the same, as explained in section 2.1. In this chapter we present time-resolved XPS measurements on a SRO/BTO/SRO heterostructure. This sample was exposed to an *in situ* P.U.N.D. train of pulse in the vacuum chamber of the TEMPO beamline (SOLEIL), while soft X-ray photoemission was performed. We present informations on the characteristic time of polarization switching.

The study of the dynamic process of polarization reversal implies subjecting the sample to a high number a switching events, which can induce fatigue in our sample. This study thus might also give access to informations on fatigue in device-like structures by defining the application limits in terms of maximum frequency and long-term fatigue [187]. Indeed, it is crucial to know a capacitor life-time before it exhibits signs of fatigue, when highly solicited. Several studies, including Lou *et al.* [172] and Kim *et al.* [188], found that fatigue is experienced in similar herostructures after a number of switching events comprised between 10^6 and 10^9. We will compare these results with the conditions in which fatigue is experience in our capacitors.

4.1 Design of the studied heterostructure

These time-resolved experiments were performed on a SRO(2 nm)/BTO(60 nm)/SRO(35 nm) heterostructure. In order to study the kinetics of switching on the same heterostructure as the one presented in chapter 3, studied by operando HAXPES, we chose to use the same sample design, and the microfabrication process was performed. The final design is presented in Figure 4.1, with a side schematic view of the device ready for introduction into the photoemission end-station. The details of the growth process are described in section 3.1.

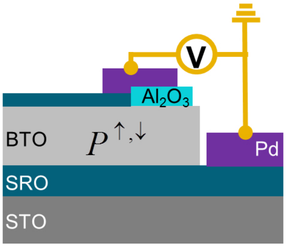

Figure 4.1 – *Schematic of the connected SRO/BTO/SRO//STO heterostructure. The gold micro-wiring is represented in yellow.*

To ensure that this heterostructure exhibited proper polarization and electrical characteristics for the time-resolved XPS measurements, *in situ* electrical characterizations were performed on the sample, and C-V and I-V curves were recoreded. The capacitance of the system as a function of the applied voltage (C-V loop) is presented in Figure 4.2. Figure 4.2 shows a C-V butterfly loop, characteristic of the switchable ferroelectric state of the capacitor. The coercitive voltage needed is -0.20 V to switch from $P^{\uparrow}$ to $P^{\downarrow}$ and 0.95 V from $P^{\downarrow}$ to $P^{\uparrow}$. The accurate measurement of these values is crucial for application of correct bias voltages during the measurements. The C-V loop shows that the crossing of the two branches of the butterfly loop does not occur at 0 V, as expected for a FE material with no internal field, but at +0.2 V. This means that the sample has a tendency to be naturally in the $P^{\uparrow}$ state, *i.e* that it demonstrates ferroelectric behavior with a weak built-in $P^{\uparrow}$ polarization. The C-V characteristic of this sample thus shows a very similar behavior than the sample studied in the previous chapter. We note that the apparent difference in the off-centering of the C-V curve (here to a positive voltage, and to a negative voltage in chapter 3) simply comes from the fact that the voltage is applied here on the top electrode (with the bottom electrode grounded), whereas it was applied on the bottom electrode in chapter 3.

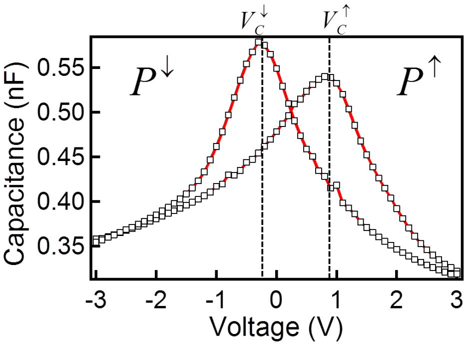

FIGURE 4.2 – *C-V butterfly characteristic of a FE capacitor. $P^{\uparrow}$ is obtained by applying a positive voltage to the top electrode; i.e. with the bottom eletrode on ground potential.*

4.2 Time-resolved X-ray Photoemission Spectroscopy

4.2.1 Preliminary experiments: Static measurements

The samples were introduced in the XPS analysis chamber of the TEMPO beamline. We chose to work at a photon energy of 1100 eV. This energy was selected to combine a high enough IMFP to probe below the SRO electrode with reasonable signal to noise ratio, while taking into account the characteristics of the beamline giving a high flux at this energy. After proper calibration using the SRO Fermi edge, we determined that the exact photon energy was 1097.15 eV. This energy was high enough to acquire a signal through the 2 nm deep top electrode. Indeed the IMFPs at this energy in the BTO are: 8.53 Åfor the Ba $3d_{5/2}$, 19.13 Åfor the Ba *4d*, and 13.75 Åfor the Ti $2p_{3/2}$ [141]. Beam spot size was (30×100) μm^2. We chose the electrode size accordingly, so that the beam can be entirely positioned on the capacitor without impinging on the surrounding region. The chosen size of the electrodes was (300×300) μm^2. In order to locate the wired SRO top electrode, the surface was mapped by moving the sample while measuring the Pd *3d* photoemission spectrum. From the obtained map, the position of the palladium pads, and thus of the adjacent SRO electrodes could easily be found. Figure 4.3 shows a picture of the sample where the position on the connected pad is circled in red.

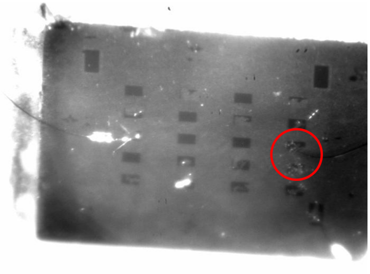

Figure 4.3 – *Photo of the sample in situ. The palladium pads appear in a darker color than the BTO background. The connected pad is circled in red.*

Figure 4.4 shows the survey spectrum acquired on the connected capacitor, in the case where both electrodes are grounded. The spectrum shows core level peaks characteristic of the SRO electrode and the BTO layers, confirming that the beam is well positioned on the SRO pad and that we receive signal from the BTO below, through the electrode. The insert shows a high resolution scan of the Fermi edge and its corresponding fit using a Fermi-Dirac distribution. The sharp edge confirms the metallic-like character of the 2 nm SRO top electrode.

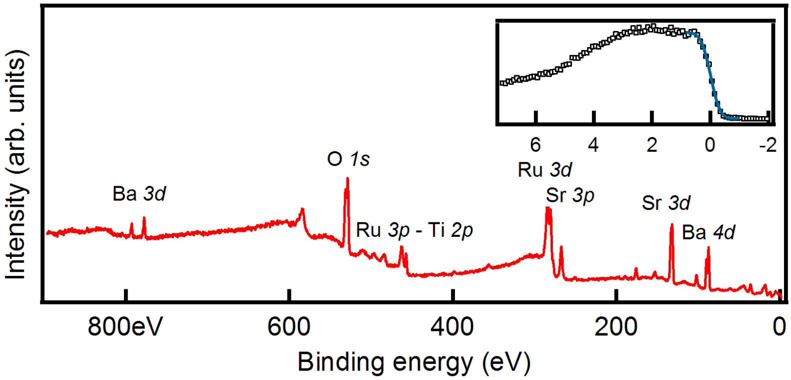

FIGURE 4.4 – *XPS survey spectrum showing the core level peaks characteristic of the SRO electrode and of the BTO FE. The binding energy scale was calibrated using the Fermi edge. The insert is a scan close to the Fermi level region showing the sharp metallic Fermi edge at zero binding energy.*

First, static core level spectroscopy was conducted on the sample, at the two remanents states. We used a bias of ± 3 V for 1 minute on the top electrode of the capacitor to ensure that it was fully switched. The sample was then grounded to perform the measurements.

On the top electrode, the Sr *3d* core level spectra were measured to ensure that there was no remaining bias in the capacitor. The Sr $3d_{5/2}$ core level spectra for both polarization states are presented in figure 4.5. The two core level spectra are perfectly superimposable, indicative that no remaining bias on the top electrode is displacing the core level and thus risks disrupting the measurements.

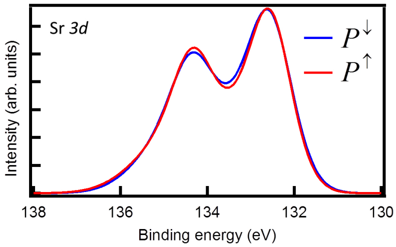

FIGURE 4.5 – *Sr 3d core level spectra acquired at remanence for the* $P^{\uparrow}$ *and* $P^{\downarrow}$ *polarization states.*

We measured the Ti $2p_{3/2}$, Ba $3d_{5/2}$ and Ba *4d* core levels. The spectra are presented in figure 4.6, in the P$^{\downarrow}$ state (top part of the figure) and in the P$^{\uparrow}$ state (bottom part of the figure). Overall energy resolution is calculated from the characteristics of the beamline to be 400 meV. After substraction of a Shirley background, the spectra were fitted using pseudo-Voigt functions with a 70 to 30 Gaussian to Lorentzian ratio, as previsouly used in the data treatment in chapter 3. For all spectra, the different peaks obtained from the peak fitting are filled in different shade of grey (dark and light), and the overall best fit is represented by a blue line. A slight asymmetry of the peaks to higher binding energy (HBE) for both polarizations is noticeable suggesting, as for the sample measured in HAPXES, the existence of an interface component at higher binding energy. The FWHM is 0.85 eV for the bulk peaks, and 0.95 eV for the interface peaks. In the case of the Ti $2p_{5/2}$ core level, the peak at HBE is partially covered by the Ru $3p_{3/2}$ core level, which nominal binding energy is 461.4 eV and which intensity is much higher than the Ti $2p_{5/2}$ core level one. For this reason it is impossible to observe the HBE component attributed to the interface. However, it is still possible to access the BE position of the peak. On the figure 4.6 in the case of the Ti $2p_{5/2}$ core level, we only presented part of the spectra: the end of the actual measured spectra is marked by two black parallel lines, and above 460 eV the intensity is brought to zero. An energy shift of ~0.11 eV between both polarization states is observed for all of the measured core levels. This suggests that all of the three core levels related to the BTO layer are affected in a similar way by the applied bias.

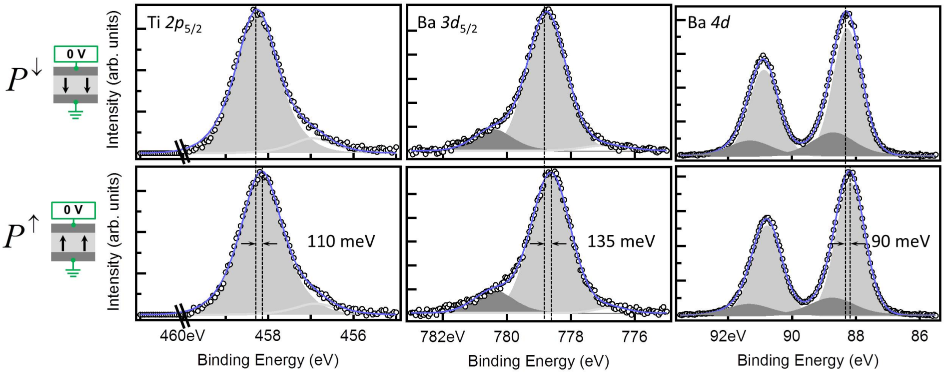

FIGURE 4.6 – *Ti $2p_{5/2}$, Ba $3d_{5/2}$ and Ba $4d$ core level spectra in the P$^{\downarrow}$ (top) and P$^{\uparrow}$ (bottom) states in remanence (black empty dots). The peaks used for the peak fitting (filled in dark or light shades of grey) and the corresponding fit (blue line) are superimposed on the spectra.*

4.2.2 Description of the time-resolved setup

a) Time-resolved set up: use of a delay line detector

Time-resolved experiments were possible using a delay-line detector (DLD). With such a device, electrons can be detected with a resolution time down to 5 to 10 ns [84]. A DLD can measure events in temporal reference to an external clock. The DLD consists of a microchannel plate array for pulse amplification and an in-vacuum readout unit, the DLD anode. The DLD anode basically consists of two meander structured delay-lines, one rotated by 90° with respect to the other, and both isolated from each other. A positive potential between the Microchannel Plates (MCP) of the detector and the anode draws the electron cloud from the MCP output to the DLD anode. It induces electrical pulses in the delayline by capacitive coupling. The pulses are traveling to both ends of the meander within a time determined by the hitting position. The average time at both ends of the meander relative to an external repetitive clock generates the time coordinate. Each hit position is encoded by a fast data acquisition unit, which can also detect the hit time referenced to an external clock in repetitive experiments. Delayline detectors are single counting devices; therefore the complete device works even at extremely low numbers of incoming electrons. At the TEMPO beamline, the Scienta SES 2002 electron energy analyzer was modified by replacing the CCD Camera by a delay line detector which can associate each detected photoelectron to the SOLEIL Clock. This configuration allows performing photoelectron spectroscopy experiments using the isolated bunch when SOLEIL is injected in hybrid mode.

b) Application of the P.U.N.D. train of pulse on the sample

As we can see schematically on Figure 4.1, the sample was electrically connected *in situ* using gold micro-wiring. A bias of ± 4V was applied on the top SRO electrode (through the Pd pad) following the P.U.N.D. voltage pulse sequence, described in section 2.1.

Figure 4.7 a) is a schematic of the P.U.N.D. train used for the experiments. It is as follows: At t = 0 sec, we set V = 0 V which corresponds to the $P^{\uparrow}$ state, as known from the C-V measurements showed in Figure 4.2. At t = 1 μs, an upward pulse V = +4 V is applied for 1 μs, and then V is fixed at 0 V for another period of 1 μs. This sequence is repeated a second time. Then at t = 5 μs, a downward pulse V = −4 V is applied during 1 μs before dropping to 0 V again for 1 μs and is then repeated a second time. Thus one P.U.N.D. train lasts overall 9 μs. Figure 4.7 b) is a photo of the voltage supply used to apply the bias on the sample. On the screen we can see the P.U.N.D. train used for the experiment.

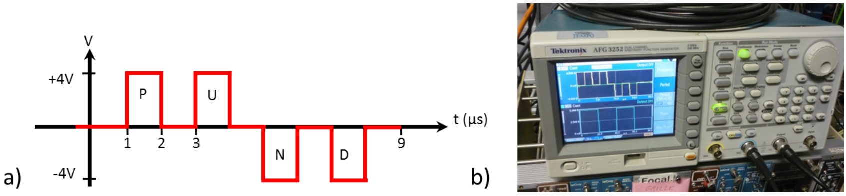

Figure 4.7 – *Schematic of the P.U.N.D. train of pulses used in situ on the SRO/BTO/SRO heterostructure. b) Photography of the voltage supply used to apply the wanted bias on the sample.*

Core level photoelectrons were measured during this process, with snapshot spectra acquired with a frequency of 50 MHz. A total of 450 successive snapshots were thus acquired in the 9 μs duration of one P.U.N.D train. Both the Pd *3d* and the Ba $3d_{5/2}$ core level spectra were recorded. The pulse train was repeated several times (7000 times for the Pd *3d* and 1030 times for the Ba $3d_{5/2}$), in order to acquire a sufficient photoemission signal/noise ratio. The electron dynamics being in the range of 10-100 fs [189], the response should be instantaneous for a bias applied in a few tens of nanoseconds, as made possible by the frequency generator used.

4.2.3 Pd *3d* core level spectra peak fitting

The first step of the time-resolved experiment is the Pd *3d* core level acquisition during the P.U.N.D. train of pulse. The palladium pad connected to the top electrode is probed. The aim is to verify if the response of the electrode follows the dynamic of the circuit used to apply the bias. Since the palladium is the topmost layer of the studied heterostructure, the Pd *3d* core level spectra give very good signal/noise ratio. This allowed us to develop an automatic peak fitting procedure to access the displacement of the Pd *3d* core level as a function of time. This procedure is also used on the less intense Ba core levels, where effects of the polarization switching are expected.

Figure 4.8 a) shows a Pd *3d* photoemission core level reference spectrum taken with both electrodes grounded before the application of the P.U.N.D. train. The energy window of the acquisition was chosen so that the Pd $3d_{5/2}$ peak was in the center of the window. The total width of the peak was about 4 eV (with a KE between about 760 eV and 764 eV), and we expected an energy shift of ± 4 eV since the applied bias is ± 4 V. The width of the snapshot window is 6% of the Pass Energy. Therefore, we used a pass energy of 200 eV giving a window of 12.54 eV. Figure 4.8 b) is an image of the Pd *3d* core level spectral intensity as a function of time; the color scale represents the intensity of the photoemission signal. One vertical line of this image corresponds to a Pd *3d* spectrum, similar to the one presented figure 4.8 a). The time abscissa between 0 and 9 μs corresponds to the duration of one P.U.N.D. train. As a single P.U.N.D. train pulse gives rise to spectra with low signal to noise ratio, the P.U.N.D. was repeated 7000 times. Therefore, each vertical line of the image is the average of seven thousands spectra. The P.U.N.D. signal can easily be identified on this image, as the Pd *3d* shifts along with the applied bias. In the upper part of the figure 4.8 b), we schematically represented the P.U.N.D. train.

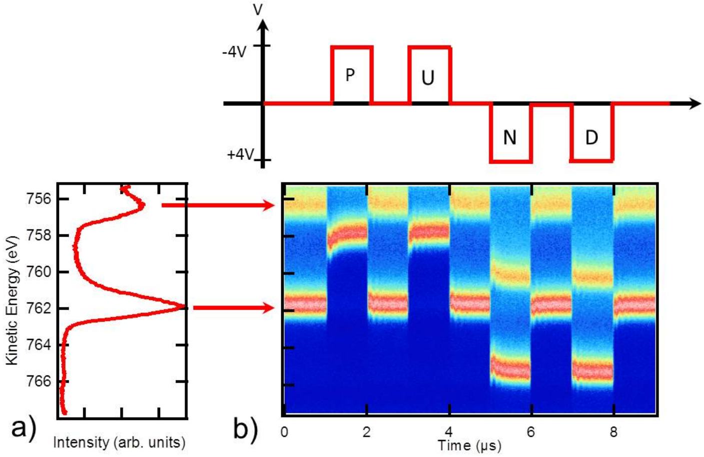

FIGURE 4.8 – *a) Pd 3d core level photoemission spectrum b) Image of the Pd 3d core level photoemission spectra as the function of time, following a PUND train. The color scale represents the intensity of the photoelectrons.*

We checked that the general shape for every recorded spectrum did not change with time. An automated fitting procedure was then developed to subtract the secondary electron background and to fit each spectrum of the image with a Gaussian function. A correct peak shape would consist in using the asymmetric Doniach-Sunjic function [190], best represetative of a metal. However, since in this study we are only interested in the position of each peak, and not to its exact shape, Gaussian functions were used to simplify and speed up the automatic fitting procedure. The width of each peak is kept constant after a preliminary fit procedure using one of the snapshot spectra. A typical 7000 shot averaged snapshot spectrum along with the corresponding Gaussian fit are presented in Figure 4.9. The FWHM of the Gaussian peak was 0.80 eV and was fixed at this value for the rest of the procedure (*i.e.* for the fit of all 450 Pd *3d* core level snapshot of the P.U.N.D train).

Figure 4.10 a) displays an image of the Gaussian peak fit as a function of time, resulting

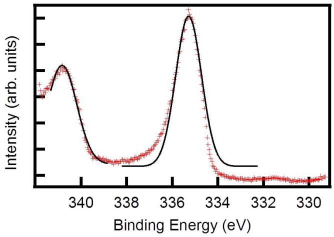

Figure 4.9 – *Snapshot of the Pd 3d core level acquired during the time-resolved experiment (red crosses) and Gaussian fit (black line).*

from the automatic peak fitting procedure (replacing the raw data in image Figure 4.8 a)). The Gaussian peaks are displayed in binding energy as a function of time. The energy shift measured with respect to the position at zero bias for each Gaussian peak is presented as a function of time in figure 4.10 b). This allows following the shift of core level due to the electrical excitation of the capacitor while it is going through the P.U.N.D. train.

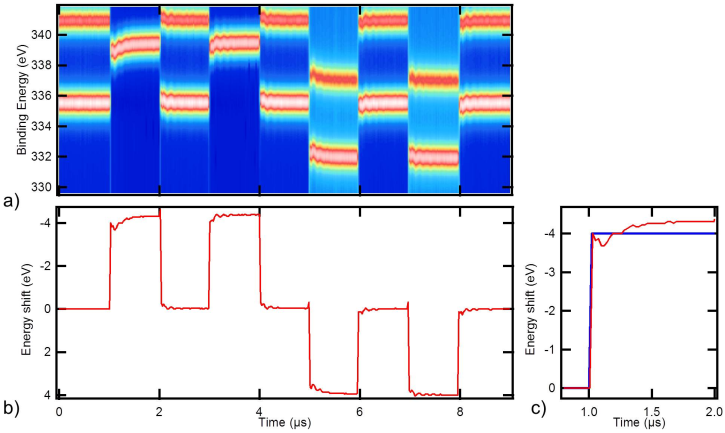

Figure 4.10 – *a) Map of the Pd $3d_{5/2}$ and $3d_{3/2}$ peaks, resulting by a systematic peak fitting for each spectrum of image Figure 4.8 b) with a Gaussian function. b) Energy shift of the Gaussian peaks from their energy at zero bias as a function of time.c) Zoom of the P pulse showing the energy shift spectra (red) and the applied bias (blue).*

When observing the energy shift of the Pd $3d_{5/2}$ core level as a function of time, we can directly notice that the shift does not exactly follow the shape of the P.U.N.D. train. Indeed, when looking closely at each one of the pulses, as presented on the zoom of the P pulse in figure 4.10 b), it gives a non-instantaneous response to the applied bias. This means that there is a time constant in the system slowing down the core level response to a bias pulse. We fitted the spectra 4.10 b) to access the time constants of the charges for the four pulses P, U, N and D. The resulting spectra along with these fits, and the values of the time constants are compiled in figure 4.11. In the case of the metallic palladium, the time constants for each pulses are expected to be identical, as they represent the electrical circuit. However, as we can see, they are different for the P and N pulses versus the U and D pulses. Furthermore, for both bias directions, the switching time constant is significantly different from the non-switching one. The circuit response is therefore quite complex. This behavior, different to the one expected for the palladium core level, will be discussed in section 4.2.5.

The ripples observed on the image obtained from the time resolved measurements are probably due to a finite impedance in the circuit. Indeed, the samples are connected via gold micro wiring to a copper plate, but silver paste was also used to connect this plate to the sample holder, which might provide imperfect connection with a residual impedance. To ensure that those ripples are indeed a characteristic of the electrical circuit and not the polarization switching, we checked that they disappear after subtracting the displacement measured during a non-switching pulse to the one measured during a switching pulse.

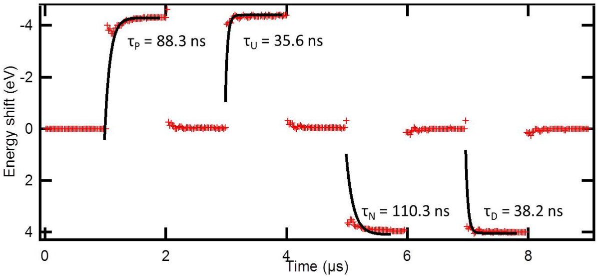

FIGURE 4.11 – *Energy shift of each Gaussian peak from its energy at zero bias as a function of time (red crosses), and fits of the charges and discharges of the P.U.N.D. circuit (black lines). The values of the characteristic times for each pulse,* τ_P, τ_U, τ_N *and* τ_D, *obtained from the fits are indicated on the figure.*

4.2.4 Ba $3d_{5/2}$ peak fitting

After having acquired the Pd signal, the Ba $3d_{5/2}$ core level spectra were measured, providing a signature of the BTO interface layer below the SRO. The same P.U.N.D. train of pulses was applied on the sample and the Ba $3d_{5/2}$ core level was recorded. The capacitor was exposed to a total of 1030 P.U.N.D. pulse trains. We used a smaller number of trains, as this sequence was planned to be repeated 10 times, to obtain results on a total number of 10300 pulse trains. Since the capacitor experienced a loss of FE (see section 4.3), the experiment was stoped after this first sequence. The Pass Energy chosen was again 200 eV, giving a 12.54 eV wide window. The automatic peak fitting procedure optimized on the Pd *3d* spectra was used to fit the Ba $3d_{5/2}$ core level. One of the averaged snapshots acquired during the P.U.N.D train of pulse was fitted using a Gaussian to access the value of the FWHM of the peak. This value was then fixed for the rest of the peak fitting procedure. The snapshot, along with its fit, is presented in Figure 4.12. We can note an increase of the signal on both sides of the spectrum. This is an artefact due to the detector. The core level presents two contributions, probably corresponding to a bulk and an interface contribution. Both were fitted using a Gaussian of a 0.9 eV FWHM. During the P.U.N.D. pulse train, both the interface and bulk peak responded in the same way to the applied bias, and thus in the rest of the study we will only consider the response of the bulk peak. The statistics of the Ba $3d_{5/2}$ core level snapshot is much lower than for the Pd *3d* (since the signal comes from a buried interface). However, this fit is sufficient to access the displacement of the core levels, which is the information that we are interested in.

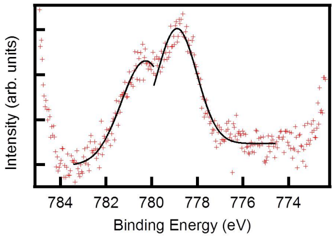

FIGURE 4.12 – *Snapshot of the Ba $3d_{5/2}$ core level acquired during the time-resolved experiment (red crosses) and Gaussian fit (black line).*

Figure 4.13 shows the results of the peak fitting obtained for the Ba $3d_{5/2}$ core level spectra. In figure 4.13 a) the raw Ba *3d* spectra as a function of time are shown, and in figure 4.13 b), the energy shift accessed by the automatic peak fitting as a function of time is presented. As expected from the low signal of the single averaged Ba $3d_{5/2}$ snapshot, the intensity of the map presented in Figure 4.13 a) is much lower than that of the Pd *3d* presented before. Indeed, the Ba atoms are from the BTO, measured below the 2 nm of the SRO top electrode, while the Pd is located on a thick connecting pad on top of the sample. Moreover, the intrinsic continuous background is also much higher for the Ba *3d* core level which BE is higher than the Pd *3d* one, which also contributes to the poorer statistics.

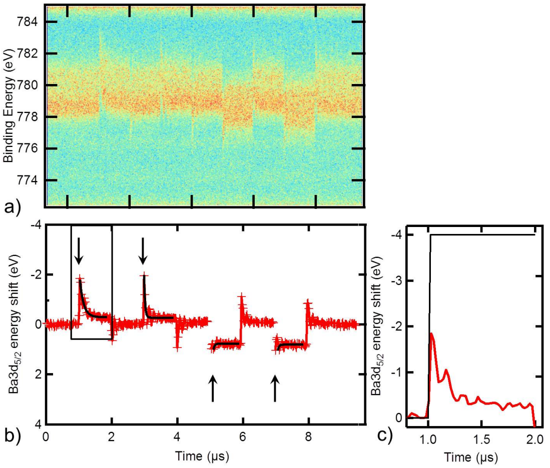

FIGURE 4.13 – *a) Map of the Ba $3d_{5/2}$ peak as a function of time b) Energy shift of each Gaussian peak (used to fit the Ba $3d_{5/2}$ core level peak presented in figure a)) from its value at zero bias as a function of time. c) Zoom of the P pulse showing the energy shift spectra (red) and the applied bias (black).*

The first noticeable aspect of the fitted peak positions presented in figure 4.13 b), is that the general shape is very different from the one of the P.U.N.D. pulse train. Close to the rise and fall of the bias pulses, we can notice spikes in the time-dependent binding-energy curves. When the first P pulse is applied on the sample, the Ba *3d* core level is almost immediately shifted to lower binding energies, and the capacitor then seems to relax. When looking closely at the Pd *3d* core level results, we can see that those spikes were already present before the charge and discharge of the capacitor. The image presented in figure 4.13 c) shows a zoom on the P pulse. The width of the spike is 20 ns. We can also notice that after those spikes, the Ba *3d* core level does not stay shifted by ± 4 eV for the entire duration of the pulse. Indeed as previously mentioned, the capacitor seems to relax directly after the spike. For the P pulse for example, the energy shift after relaxation is only − 0.2 eV instead of the − 4 eV expected. Finally, there are several differences between the positive and negative pulses, *i.e.* between the two polarization states. Indeed, neither the intensity of the spikes nor the value of the core level displacement after the relaxation are the same between the $P^{\uparrow}$ and $P^{\downarrow}$ states. These three results will be discussed in the next section.

4.2.5 Discussion of the time-resolved results

In the Ba *3d* response to the P.U.N.D. pulse train we observed that after a spike corresponding to an increase of the energy shift to the value of the pulse (± 4 V), the Ba *3d* core level relaxes to a smaller shift. We can conclude that those spikes are probably related to the polarization switching itself: when applying a bias on the sample, the polarization is immediately switched. The widths of these spikes (about 20 ns) gives us an idea of the time of the polarization switching. However, despite the applied bias, the shift is not maintained, the polarization does not hold and the Ba environment seems to relax towards that similar to the one before switching. In the HAXPES experiments conducted in chapter 3, the heterostructure could easily maintained the polarization under a bias of ± 1.1 V without showing any sign of leakage. In this case, the displacement never reaches the ± 4 V bias applied, indicative of the highly leaky behavior of the capacitor. The loss of the ferroelectricity can be observed in the time constant of the capacitor relaxation from the spikes to its minimum value. For the $P^{\uparrow}$ state, we obtain relaxation times of 0.52 μs, and of 0.23 μs for the $P^{\downarrow}$ polarization state.

We can notice that the general shape of the Ba*3d* core level displacement looks like the derivative of the Pd displacement curve showed in the previous section. This could be attributed to the fact that the capacitor first gets charged, which corresponds to the first displacement of the Ba*3d* core level to its maximum. Once the capacitor is fully charged, screening is taking place, reducing the displacement to a value close to 0 V in a screening time of 0.52 μs, and of 0.23 μs for the $P^{\downarrow}$ polarization state.

There are also differences between the response to the pulses for the two polarisation states. We would have expected a similar response in the case of identical Schottky barrier heights at the electrode/FE interface for $P^{\uparrow}$ and $P^{\downarrow}$. We are thus in a case where the height of the barrier varies with the polarization. Since the sample is leaky, it means that the some parts of the capacitor are conducting whereas some are not. The barrier height is also probably be inhomogeneous on the surface of the capacitor. Due to high leakage in the capacitor, it is impossible to access the charging time of each one of the P.U.N.D. train pulses and thus measure the entire kinetics of the polarization reversal.

When measuring the charging times of the 4 P, U, N and D pulses for the Pd *3d* core level shifts, we measured different values for the switching and the non-switching pulses. This is what would be expected for the response of a FE material, but not for this metallic pad. A hypothesis is that given the very low thickness of the SRO top electrode, this oxide behaves as the BTO ferroelectric itself, and the palladium actually gives information directly on the behavior of the ferroelectrics. Following this hypothesis, the Pd *3d* response gives access to the values of the time constants of the system. In this case, the difference between the non-switching and switching pulses equals the characteristic time of the polarization switching τ_{Pol}. More generally, the study of the paladium response can give us informations about the polarization switching times even without this hypothesis. For the $P^{\uparrow}$ to $P^{\downarrow}$ polarization switching, the characteristic time $\tau_{Pol_{P\downarrow}}$ is:

$$\tau_{Pol_{P\downarrow}} = \tau_P - \tau_U \tag{4.1}$$

$$\tau_{Pol_{P\downarrow}} = 88.3 - 35.6 = 52.7\ ns \tag{4.2}$$

For the $P^{\downarrow}$ to $P^{\uparrow}$ polarization switching, the characteristic time $\tau_{Pol_{P\uparrow}}$ is:

$$\tau_{Pol_{P\uparrow}} = \tau_N - \tau_D \tag{4.3}$$

$$\tau_{Pol_{P\uparrow}} = 110.3 - 38.2 = 72.1\ ns \tag{4.4}$$

We obtain a switching time of 52.7 ns for the $P^{\uparrow}$ to $P^{\downarrow}$ reversal, and of 72.1 ns for the $P^{\downarrow}$ to $P^{\uparrow}$ reversal. In the case of FE BTO based heterostruture, a study from Gruverman *et al.* [111] shows that characteristic times of switching of about tens of nanoseconds are expected, meaning that the polarization switching process is way faster than the response of the electrical circuit. These values are in the same order of magnitude as expected from the Gruverman *et al.* study [111].

The reason why the paladium core level does not exhibit the same leaky behaviour might be its metallic nature, allowing maintaining the ± 4 V in the capacitor. Moreover, the Pd *3d* response was measured several hours before the Ba *3d* response. For this second experiment, the capacitor might be undergoing some fatigue, weakening its ferroelectricity. In order to understand phenomena that could be responsible for the loss of ferroelectricity observed in the case of the Ba *3d* core level study, we now discuss the influence of the bias voltage amplitude and X-ray beam on the switching kinetics. This will be presented in section 4.3.

4.3 Fatigue

4.3.1 Influence of the switching on the capacitor fatigue

To understand the loss in FE, we performed electrical C-V measurements on the capacitor. The FE character of the capacitor was checked by recording C-V curves *in situ* at several times during the photoemission experiment. Figure 4.14 displays the C-V curves measured before a) and after b) the time-resolved experiment. Before the experiment, the C-V curve recorded *in situ* exhibits the classical butterfly loop, characteristic of the existence of FE polarization in the capacitor. However, the *in situ* C-V curve recorded immediately after the time-resolved experiment no longer shows any proof of a FE behavior of the capacitor. Since the curve did not exhibit the butterfly shape, symptomatic of a FE behavior, we stopped the recording of the C-V after only one sweep from -3 V to 0.5 V. This means that the BTO was no longer ferroelectric after the time-resolved experiments.

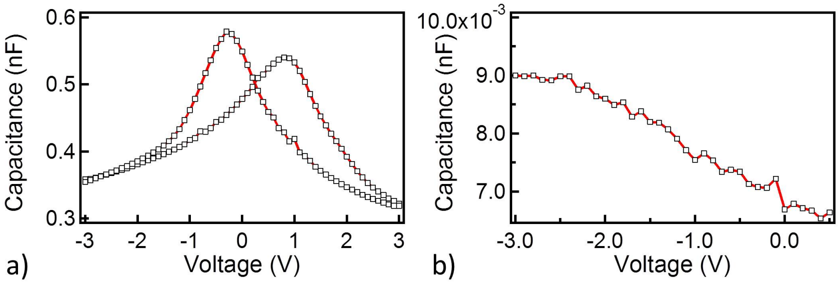

Figure 4.14 – *a) C-V curve recorded in situ from -3 V to $+3$ V before the time-resolved experiments and b) from -3 V to $+0.5$ V after the time-resolved experiments.*

Two main phenomena may explain this change in the C-V curve. This can either be due to the effect of a prolonged exposition to the high flux of the photon beam, or to the repeated switching process, as the capacitor was switched several thousand times. Indeed, the second C-V curve was recorded after a total of 11200 P.U.N.D train of pulse, *i.e.* the sample was switched a total of 22400 times from one FE state to the other. The total number of reversals (about 10^4) is way lower than the limit predicted by literature (between 10^6 and 10^9) before signs of fatigue are detected in the capacitor.

4.3.2 Influence of the synchrotron beam high flux on the capacitor fatigue

In order to distinguish if the loss of FE is caused by the synchrotron beam or by the switching process itself, we performed another experiment focused on the effect of the beam on the capacitor, on a similar SRO(2 nm)/BTO(60 nm)/SRO(35 nm) heterostructure. We recorded C-V curves of the capacitor exposed to the beam without applying a bias, *i.e.* with no FE polarization switching. Figure 4.15 presents the obtained C-V curves recorded *in situ* before exposure, during exposure (after a few minutes only under the beam), and after 4 hours of exposure to the beam. We can note that for this sample, used exclusively for the study of the influence of the beam high flux, the natural polarization imprint is different than for the similar sample of the main time-resolved study, probably due to differences in the growth parameters (with several months between the growth of these two samples).

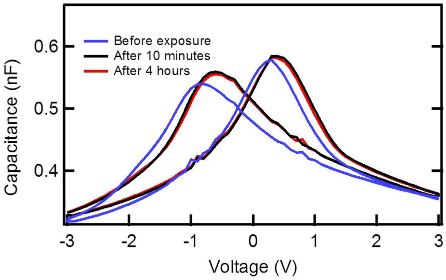

FIGURE 4.15 – *C-V curves recorded in situ on a SRO/BTO/SRO capacitor before exposure to the X-ray beam (blue line), during exposure (black line) and after 4 hours of exposure (red line).*

The general shapes of the three curves are unchanged and the beam has only very small effect on the C-V curve. Coercive voltages are slightly shifted toward higher voltages, but the maximum capacitance values are increased by less than 4 %. The reduction from the beam is expected to decrease the maximum capacitance values. This increasing by a very small percentage can be associated with a measurement artefact. Thus, the synchrotron beam has no detrimental effect on the FE.

4.4 Conclusion and Discussion

In this chapter, the dynamic process of polarization reversal of the ferroelectric BTO was studied by performing time-resolved XPS experiments on a SRO/BTO/SRO heterostructure. Studying the response of the Ba *3d* core level to a P.U.N.D. pulse train allowed exhibiting differences between the two polarization states $P^{\uparrow}$ and $P^{\downarrow}$. Mainly we found a difference in the Schottky barried height of the electrode/FE interface. However, leakage and fatigue in the capacitor prevented access to time constants of the polarization switching process. The study of Pd *3d* core level of the palladium pad connected to the SRO top electrode permitted observation of a difference between the characteristic time of the non-switching and switching pulses of the P.U.N.D. train. Due to the very small thickness of the top electrode, the latter behaves as the ferroelectric BTO itself. Thus, the displacement of the palladium core level can be used to access information on the FE polarization switching dynamic. Thanks to an automatic peak fitting of the core levels, the energy shift gave access to time constants of 52.7 ns for the $P^{\downarrow}$

to $P^{\uparrow}$ reversal and 72.1 ns for the $P^{\uparrow}$ to $P^{\downarrow}$ reversal. These values are in the same order of magnitude of the one predicted by literature [111].

When measuring the C-V curve of the capacitor after the time-resolved XPS experiment, a loss of ferroelectricity was observed due to probable fatigue disrupting the capacitor switching abilities. When studying fatigue in ferroelectric capacitors, Kim *et al.* [188] showed that no fatigue should be expected below 10^6 to 10^9 switches of the polarization. The studied capacitor was only switched 10^4 times during the experiment, *i.e.* several orders of magnitude below the predicted limit. We used pulses of ± 4 V to switch the capacitor, about 4 times larger than the coercive field. The value of the bias is known to contribute to fatigue in thin film capacitors [172]. The combination of a high number of switches with a high value of the applied bias, as well as eventual differences to Kim study (such as the quality of the heterostructure thin films) might thus be responsible for the fatigue in the measured capacitor and be at the origin of the loss of ferroelectricity in the SRO/BTO/SRO heterostructure.

To access further information on the polarization switching kinetics, samples of better quality, less prawn to fatigue, should be used. For example, a slightly thicker SRO top electrode could reduce leakage. A smaller bias to switch the sample from one polarization state to the other should also reduce risks of fatigue. Finally, the relationship between the interface electronic structure and the reversal kinetic could be obtained by an improved signal-to-noise ratio of the Ba *3d* core-level spectra. To do so, the use of hard X-ray photoemission combined with time-resolved measurements would improve the counting statistics, without having to increase the number of polarization reversals and risk creating fatigue in the capacitor. Such experiment could allow identification of interface versus bulk film contributions. However, access to Synchrotron beamlines combining time-resolved and hard X-ray is very reduced, making such experiment difficult to perform.

To further exhibit this time dependance to the process governing the polarization switching, such time-resolved measurements should be performed on differently sized capacitors. In our case, the spatial resolution is limited by the beam spot size ($\sim$30 × 100 μm^2), thus preventing the study of realistic microchips. Hard X-ray photoelectron emission microscopy with *in situ* bias application might pave the way for in operando chemical and electronic analysis of realistic devices. In the next chapter, a first step towards such study is presented, as we probe small capacitors using HAXPEEM.

Chapter 5

Spatially resolved study of polarization switching

The classical nucleation theory of Kolmogorov, Avrami and Ishibashi [90] described in chapter 1, considers the switching process as the phase transformation in infinite media. They introduced the influence of the process controlling the polarization reversal on its time characteristic. They state that in a large capacitor (> 1 μm in diameter), polarization is reversed first by domain nucleation then by domain wall motion, whereas in smaller capacitive structures (< 1 μm in diameter), nucleation limited switching has been found to provide a more accurate description [111].

HAXPES and time-resolved measurements performed in the previous chapter demonstrated the existence of a polarization dependent distortion at the FE/electrode interface, in the case of a SRO/BTO/SRO heterostructure. The studied capacitors dimensions were (300×300) μm^2, and consisted of devices where the polarization reversal is governed by the domains nucleation. We decided to study smaller capacitors (< 1 μm in diameter), to gain information on the interface response to polarization when the polarization reversal is governed by a second phenomenum: the domain wall migration [111]. In this chapter, we will present hard X-ray photoelectron emission microscopy measurements, conducted at the P09 beamline of the PETRA III synchrotron (Desy, Hambourg).

In 2012, Chanthbouala *et al.* [159] studied the polarization reversal process in BTO tunnel junctions in the case of small capacitors (< 1 μm in diameter). They reported transport measurements in ferroelectric tunnel junctions as a function of the amplitude, duration and number of voltage pulses applied on the capacitor, showing a resistance that can be continuously and reversibly tuned over more than two orders of magnitude, thus qualifying the studied FE tunnel junction as a memristive device. They modeled the resistive switching behaviour using a model of domain nucleation and growth, and derived an expression ruling the memristive response.

We decided to study a heterostructure similar to the ones used in Chanthbouala's study in terme of size and nature of the capacitors. The sample we prepared was a BTO thin film, with a bottom electrode of SRO deposited on a STO substrate. The top electrodes were 2 nm thick cobalt pads, capped by 4 nm of gold (600 nm in diameters). The goal of these experiments is to obtain spatially resolved information on the polarization switching proces. For this purpose, a set of three electrodes was switched *ex situ* using PFM. We then used HAXPEEM to study the effect of polarization on this BTO/Co interface.

5.1 Sample preparation

5.1.1 Sample design

In this study, we chose to work with smaller electrodes (< 1 μm in diameter) in order to study a different polarization reversal process than for the large electrodes presented in the previous chapters. Working with smaller electrodes, however, calls for the need of spatial resolution. Indeed, beam spot sizes are usually of the order of 100 μm^2, thus averaging signal over the entire beam spot would mean avering signal mostly from the surrounding areas around the capacitor. Moreover, the switching process takes place on the microscopic scale and would thus require such spatial resolution to be imaged. PEEM (see section 2.3) was thus used for this study. Moreover, working with smaller electrodes will limit the leakage current in the capacitors, thus providing a more direct access to information on the effect of polarization at the FE/electrode interface, as the FE is subjected to the exact applied bias throughout the entire capacitor.

The STO/SRO/BTO layers, i.e. substrate/bottom electrode/FE material, were prepared at the Institut d'Electronique Fondamentale (Orsay) using the exact same conditions as in the SRO/BTO/SRO heterostructures presented in chapter 3, and following the same lithography process as described in section 3.1.1.

In a collaboration with Unité Mixte de Physique CNRS/Thales, Co/Au top electrodes were deposited using the same lithography set and preparation conditions as in Chanthbouala's study. The Co electrodes were capped by a layer of gold in order to supress the high reactivity of Co with the atmosphere [159]. The electrodes were switched *ex situ* using piezo force microscopy prior to the experiment (see next section).

A schematic of a) the side and b) top view of the sample is presented in the figure 5.1. Using optical lithography, a set of 500 identical pads was deposited on the sample to act as the top electrode of the capacitor. These electrodes are circular (~600 nm in diameter) and made of

2 nm of cobalt capped by 4 nm of gold. In order to easily find the desired top electrodes, two Au patterns were also deposited to be used as markers.

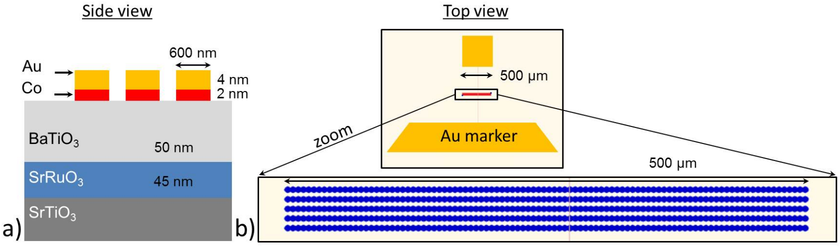

FIGURE 5.1 – *Schematic of a) the side view and b) the top view of the sample.*

Figure 5.1 b) is a top view of the samples. We can see the top gold markers in yellow, indispensable to localize the pads in the PEEM. Using the larger field of view of the PEEM, both gold patterns are visible, allowing to know the orientation of the sample and thus to localize the electrodes of interest. On the same figure a schematic of the 500 independent top electrodes is presented. They are distributed in 5 lines of 100 capacitors. The capacitors are separated from each other by 5 μm in the horizontal direction and 10 μm in the vertical direction. We fabricated a large number of capacitors to ensure that at least some of them have a low enough defect concentration for FE stability - intrinsic defects and/or oxygen vacancies in the BTO can locally affect the polarization - with an electrode of good quality, *i.e.* with a regular shape and a limited roughness. About 30 of the 500 electrodes were tested before choosing the ones that would be switched.

5.1.2 Piezo Force Microscopy characterization

Piezoelectric Force Microscopy in the writing mode (section 2.1) was used to switch the electrodes *ex situ*, prior to the HAXPEEM experiments. Three electrodes were switched, each one in one of the following different polarization states: $P^{\uparrow}$ pointing towards the top electrode, $P^{\downarrow}$ pointing towards the STO substrate, and $P^{\uparrow\downarrow}$. This last state results in a situation where the FE BTO previously in the naturally grown $P^{\downarrow}$ state was only partially switched towards a $P^{\uparrow}$ state.

We first performed AFM on the three selected pads, to characterize the shape, thickness, and quality of the electrodes. Figure 5.2 a) displays these AFM images. They show a homogenous background with the round electrode in the center. Along the red lines of Figure 5.2 a), we extracted a profile (Figure 5.2 b)) for each of the three pads, allowing to check that their thickness was indeed 6 nm. Finally we performed roughness measurements: we measured a RMN roughness[1] on the bare BTO of 0.152 nm, and on the electrodes of 0.951 nm, 1.021 nm and 0.997 nm for the pads A, B and C respectively.

The writing mode of the PFM was then used to switch the three selected electrodes as follow: one was switched in the $P^{\downarrow}$ state, one in the $P^{\uparrow}$ state, and one in the $P^{\uparrow\downarrow}$ state described above. Poling of the nano sized domains was performed by applying a d.c. voltage higher than the coercive voltage on the tip while the bottom electrode was grounded. Similarly as for the HAXPES measurements, we applied an electric field higher than the coercive field, of + or - 4 V, to make sure that the device was fully switched.

After switching, PFM imaging in the reading mode was carried out, at an excitation frequency of 4-7 kHz and an a.c. voltage of 4 V. Figure 5.2 c) displays the phase obtained by PFM images of the three electrodes. This value is closely related to the polarization state. Indeed, the measured phase is equal to zero when the field applied by the PFM tip and the polarization are in the same direction, whereas it is equal to 180° when they are of opposite signs. We see as expected that the $P^{\downarrow}$ electrode has a PFM image in which the phase is equal to 180°, opposite to the one in the $P^{\uparrow}$ state (and thus has a phase of 0°). Finally, the $P^{\uparrow\downarrow}$ electrode exhibits core-shell behavior with an outside ring of the same contrast, and thus in the same polarization state as $P^{\uparrow}$, and the inside of the pad of the same contrast and thus in the same polarization state as the $P^{\downarrow}$ state. It is worthwhile noticing that the PFM writing mode can significantly modify the surface; for example it can inject charges during the poling process [79]. This is a well-known problem in PFM-based experiments, and it can lead to a spatial variation of the surface potential, *i.e.* heterogeneity of the surface potential inside one electrode, which is not due to the remnant polarization. Therefore, all PEEM and PFM measurements were done several days after domain writing to ensure that injected charges have disappeared. Thus, we avoided any tip related screening by injected charges trapped in the top layers. After PFM was first used in the writing mode to switch the selected pads to the desired polarization state, we waited several days before checking these states using PFM in the reading mode. The polarization did not change from the one that was written. This could mean that the polarization imprint of the sample is in the same direction of the written one. However, the polarization is stable in both directions (upward and downward), contradicting this hypothesis. Is thus seems that the polarization imprint of the sample was too small to affect the polarization state of the pads. In this sample, the natural polarization is thus more randomly oriented than for the previous samples studied in chapter 3 and 4. This difference could be explained by the fact that

---

[1] RMS is one of the representations of surface roughness, calculated as the Root Mean Square average of a surfaces measured microscopic peaks and valleys, *i.e.* of the profile height deviations from the mean line, recorded within the evaluation length.

the growth of the layers was performed in a different oven, *i.e.* with slightly different growth parameters. However, it is more likely due to the nature of the top electrode (Co in the samples presented in this chapter against SRO in the previous ones) resulting in an different polarization imprint in the sample.

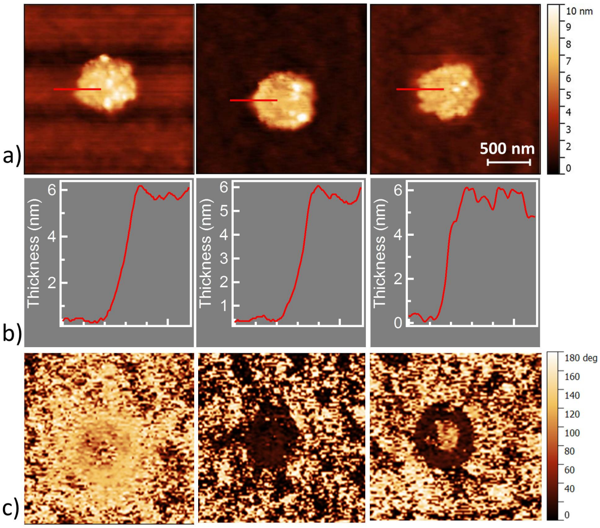

FIGURE 5.2 – *a) AFM, b) height profile (along the red line of figure a)), and c) PFM phase images for 3 pads on the Au/Co/BTO/SRO heterostructure of the pad in the* $P^{\downarrow}$ *state (left), the pad in the* $P^{\uparrow}$ *state (midle) and the pad in the* $P^{\uparrow\downarrow}$ *state (right).*

5.2 Hard X-ray photoelectron emission microscopy measurements

5.2.1 Experimental

For the HAXPEEM experiment, we used a photon energy of 3400 eV. After calibration using the Au *4f* core level, the exact photon energy was found to be 3401.6 eV. The choice of the photon energy value was made considering both the need to probe a buried interface (calling for higher photon energy values) and the fact that the core level cross sections and the transmission (section 2.3) are reduced when increasing the photon energy. To overcome the fact that the received signal is lowered by all three of those experimental issued, we worked with the slits of the analyzer opened to 2.0 mm. This increased the signal received, but lowered the energy resolution to 800 meV. We used the SESSA software [141] to simulate the survey spectrum measured at a photon energy of 3.4 keV, on this heterostructure. This survey is presented in figure 5.3. This simulation shows that the Ba *3d* core level gives a much more intense peak in comparison to other core levels from the BTO (as for example the Ba *4d* core level). The study of the Ba *3d* core level peaks thus appears as the logical choice to access information on the polarization dependence of the buried BTO.

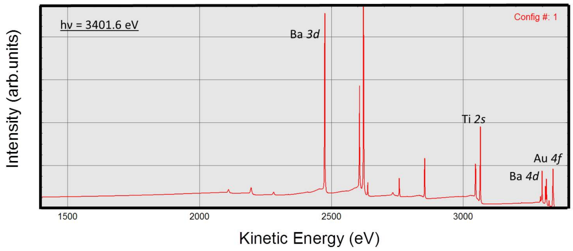

FIGURE 5.3 – *Survey spectra simulated by SESSA for a Au/Co/BTO/SRO heterostructure measured at a photon energy of 3.4 keV.*

Figure 5.4 is an image of the region of interest (ROI) containing the three desired electrodes. The field of view used is 37 μm, and the image was acquired at the photoemission threshold using the mercury lamp (hν = 4.9 eV). The electrodes appear bright on the dark background, which corresponds to the BTO layer.

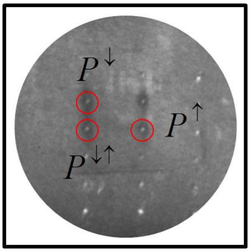

FIGURE 5.4 – *PEEM image of the ROI acquired using the mercury lamp (hν = 4.9 eV; field of view = 37μm). The three electrodes are contoured in red and are marked by their polarization states $P^{\downarrow}$, $P^{\uparrow\downarrow}$, and $P^{\uparrow}$.*

5.2.2 Localization of the three electrodes

When increasing the kinetic energy, the size of the field of view in the microscope slightly increases. This zoom is very small and does not affect the apparent size of the structures at the used FoV. However, due to the off-centering of optical elements in the NanoESCA setup on which experiment were performed, this zoom is not exactly centered in the field of view. This off-centering results in an apparent shift of the observed structure when going from imaging the secondary electrons (SE) to imaging the core level electrons (at higher energy). The apparent shift in position when going from SE to core level electrons is illustrated by figure 5.5. We can see in a) the corner of the gold marker imaged using secondary electrons, in b) the same image using the Au *4f* core-level. Images are acquired with a 115 μm field of view. We can clearly see shift in the position of the pad (3 μm in the x direction and 2 μm in the y direction).

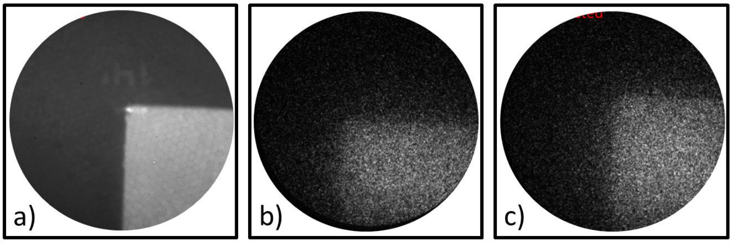

FIGURE 5.5 – *This figure shows 115 μm field of view images of the corner of the gold square marker, acquired using a) secondary electrons and b) Au 4f core-level electrons. In c) we see the same image as in b) after a correction in the sample position was applied.*

When we are imaging the secondary electrons, the quantity of received photoelectrons is the highest and thus the signal emitted by the small electrodes is sufficient to ensure good statistics. We can thus localize the electrodes even in large field of views, with acquisitions of just a few minutes (about 3 minutes). However, for core level images, the signal is much lower as less photoelectrons are emitted, especially since core level peaks from the BTO (as Ba *4d* and Ba *3d*) will appear on the entire surface of the sample and not just under the pads. This very low signal prevents us from using the live mode to localize the position of the pads. Indeed a ~15 minutes time is required to aquire an image permitting to distinguish the electrodes, by building up enough contrast. Since the electrodes are very small (600 nm in diameter) and separated from one another by only 5 μm in one direction (see description of the sample section 5.2.1). The shift of the structures, of the same order of magnitude as the 5 μm separating the electrodes, will thus make it impossible to keep track of the position of a given electrode when going from imaging the SE to the core levels. Both of these issues combined make it impossible to locate the studied electrodes when imaging directly at core-level energies.

As previously stated, the gold on top of the electrodes is needed to find their correct position. According to the SESSA simulation performed and previously presented in Figure 5.3, the cross-section is higher for the Ba *3d* core levels than the Ba *4d* at the used photon energy. However, the binding energy for the Au $4f_{5/2}$ (87.6 eV) core-level is very close to the one of the Ba $4d_{5/2}$ (89.9 eV) core-level, whereas the binding energy for the Ba *3d* is far from any gold or cobalt peak that we could use. When going from secondary electrons to core level electrons the shift in position will be similar at the Ba *4d* core level than at the Au *4f* core level. For this reason we thus recorded series for the Ba *4d* core level.

To overcome the issue of the localization of the electrodes due to the apparent shift of the structures, we proceeded to a correction of this shit, using the gold marker.

However, the intensity of the gold markers when imaged using Au *4f* core level electrons (figure 5.5 b) and c)) is quite low. The profile along the horizontal direction was plotted to determine the exact position of the edge of the marker for a proper shift correction. Figure 5.6 presents in a) the gold marker image acquired on a 115 μm field of view using Au *4f* core level, with the rectangular area from which the intensity profile was extracted. Figure 5.6 b) presents the said extracted profile. We can see the intensity as a function of the distance in μm, fitted with a sigmoid to access the position of the edge of the marker, marked by a dash black line on the figure.

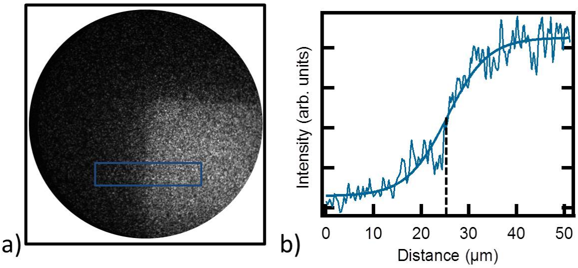

FIGURE 5.6 – *a) Image of the Au marker (FoV= 115 μm) using Au 4f core level. b) Intensity profile as a function of the distance in μm extracted along the blue rectangle in a), fitted with a sigmoid. The position of the edge of the gold pattern is marked by the black dash line.*

Once its exact position was determined, we moved the sample when imaged using core level electrons to reposition the corner of the gold pads at its initial position when imaged using SE electrons (as it appears on image 5.5 a)). The image after the correction of the shift is showed in figure 5.5 c). It was then possible to use to shift correction when imaging the electrode, and thus to properly identify the switched ones.

5.2.3 Dispersion correction

Once the switched pads have been precisely located, image series at the Ba *4d* core levels were recorded. This acquisition was made with the field of view of 37 μm which includes all three electrodes, at a photon energy of 3401.6 eV. Spectra were acquired with a step of 0.15 eV. A long acquisition time of 18 hours was required to attain sufficient counting statistics from the buried BTO below the top electrode. To make sure that an eventual beam drift was not impairing the acquisition, we separated this 18 hours acquisition in three scans of 6 hours. We checked for beam drift between subsequent scans, by readjusting the beam spot in the center of the field of view when necessary. Figure 5.7 shows the extracted Ba *4d* core-level spectra for the pads $P^{\uparrow}$, $P^{\downarrow}$ and $P^{\uparrow\downarrow}$.

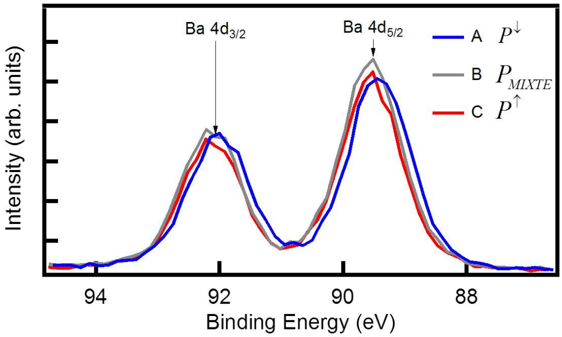

FIGURE 5.7 – *Ba 4d core-level spectra extracted for the three FE polarization states $P^{\uparrow}$ (in red), $P^{\uparrow\downarrow}$ (in grey) and $P^{\downarrow}$ (in blue), from an image series acquired with a field of view of 37 μm at a photon energy of $h\nu$=3.4 keV.*

The spectra for the three polarization states do not perfectly overlap, and a small shift in energy between the spectra is observed. To access quantitative information on the core level displacement, the image series needs to be further treated. The energy dispersion has to be determined and the image series has to be appropriately corrected. From the specificity of the instrument (the orientation of the hemisphere), the filtered images obtained by the NanoESCA have to be corrected for an intrinsic energy dispersion over the image in the vertical direction. In a given field of view, as a function of polarization along the vertical plane, non-isochromaticity occurs, as outlined by Zagonel *et al.* [155]: each horizontal line of the image taken at a kinetic energy E, corresponds to photoelectron with an kinetic energy $E+\Delta E$ where ΔE is calculated by:

$$\Delta E = E_p(\frac{M_1 y_0}{f})^2 \tag{5.1}$$

where E_p is the electron pass energy, M_1 is the magnification of the microscope in the image plane in front of the analyzer, y_0 is the vertical distance position with respect to the minimum in dispersion in the FoV (*i.e.* where $KE = E$), and f is the focal length of the extractor (29 mm for the NanoESCA [150]).

16 ROIs of the same size where chosen on the surface to be regularly separated from one another, along a vertical line in the center of the FoV. We also made sure that all spectra were extracted from homogeneous BTO area, i.e. not on a Au/Co top electrode, to avoid changes in the core levels energy. The pads positions are marked by a red circle on the figure 5.8 a). Spectra were then extracted from the chosen ROIs. The corresponding results are presented in Figure 5.8.

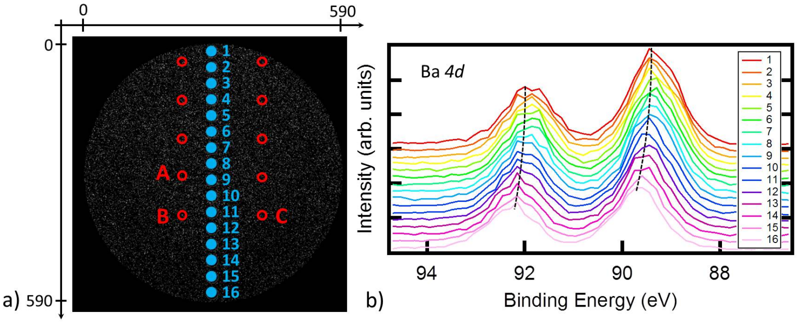

FIGURE 5.8 – *a) Position of the ROIs used for the estimation of the vertical energy dispersion and b) Ba 4d spectra extracted from those ROIs.*

In the vertical direction, as expected, there is a clear shift in energy from the top to the bottom of the FoV. Each spectrum was fitted using a combination of two Gaussian peaks, for the spin orbit coupling Ba $4d_{3/2}$ and Ba $4d_{5/2}$. The Gaussians position in binding energy was plotted as a function of the ROI positions. Figure 5.9 presents the Ba $4d_{5/2}$ core level peak BE as a function of the vertical position (in number of pixel) of the ROI in the FoV. The obtained curve was then fitted using a parabola following equation 5.1.

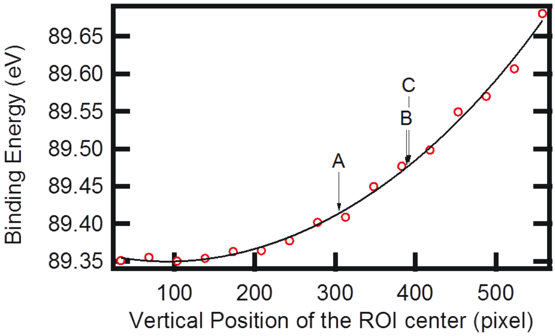

FIGURE 5.9 – *Binding energy of the Ba $4d_{5/2}$ core-level peak of spectra extracted for each ROI as a function of the position of said ROI, in number of pixel, in the field of view. The vertical positions of the electrodes of interest are indicated on the graph.*

From this curve, the energy dispersion was estimated for each one of the three electrodes depending on their vertical position in the FoV. After this treatment, the residual shift would represent a real effect in the sample due to the different polarization states.

We checked in the horizontal direction, that there is no dispersion due to other parameters (such as a microscope optics misalignment). To do so, we proceeded the same way as for determination of the the vertical dispersion, but we used a smaller amount of ROIs (7) regularly separated from one to another in the horizontal direction and located in the center of the FoV. Figure 5.10 a) presents an image from the recorded energy series, on which we indicate the position of the top electrodes (red circles), and the regions of extraction (blue discs). For representation purpose, the area of the discs and circles marking the position of the electrode and ROIs are larger on the figure than they actually are. On figure 5.10 b) spectra for each of the 7 ROIs are displayed.

The extracted spectra on the horizontal direction are all perfectly superimposable, which confirms that there are no energy shifts of the core level in the horizontal direction due to the experimental set up.

5.3 Results

Following energy dispersion correction, the Ba $4d$ core-level spectra were fitted using pseudo-Voigt functions, with a 70 : 30 ratio of Gaussian to Lorentzian, after subtraction of the back-

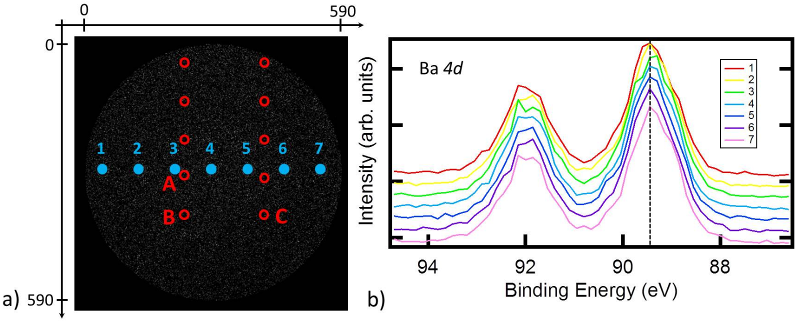

FIGURE 5.10 – *a) Position of the region of extraction for the estimation of the horizontal energy dispersion and b) extracted Ba 4d spectra for the 7 considered regions.*

ground using a Shirley algorithm [128]. Each peak is fitted with a pseudo Voigt function of 0.8 eV FWHM. Spectra show two peaks, corresponding to the double contribution due to the Ba $4d_{5/2}$ and Ba $4d_{3/2}$ spin-orbit splitting. Branching ratio and spin-orbit coupling were found to be 2.6 eV and 1.5, in perfect agreement with litterature prediction and previous results from chapter 3. The three fitted spectra are presented in figure 5.11. The binding energies of the Ba $4d_{3/2}$ components are presented in table 5.1 for the three spectra, along with the value of energy shifts between them.

Electrode	A ($P^{\downarrow}$)	B ($P^{\uparrow}$)	C ($P^{\uparrow\downarrow}$)
Binding Energy (eV)	91.990	92.141	92.012
ΔE (eV)	0.000	0.150	0.022

TABLE 5.1 – *Binding Energy of the Ba $4d_{3/2}$ components for the three polarization states.*

From the value presented in table 5.1, the presence of a shift of 0.150 eV between the core levels of the $P^{\uparrow}$ and $P^{\downarrow}$ states is evidenced. In our previous HAXPES experiment at remanence, the shift between the core level at the two polarization states was found to be almost zero, suggesting that ionic relaxation and free charges had efficiently screened the internal field. For the measurements at saturation, however, we observed the existence of a shift of 0.37 eV at the interface and concluded that 1.3 (2.6) unit cells of BTO were altered in the $P^{\uparrow}$ ($P^{\downarrow}$) state at the SRO/BTO interface.

The difference in the value of the energy shifts between the HAXPES and HAXPEEM

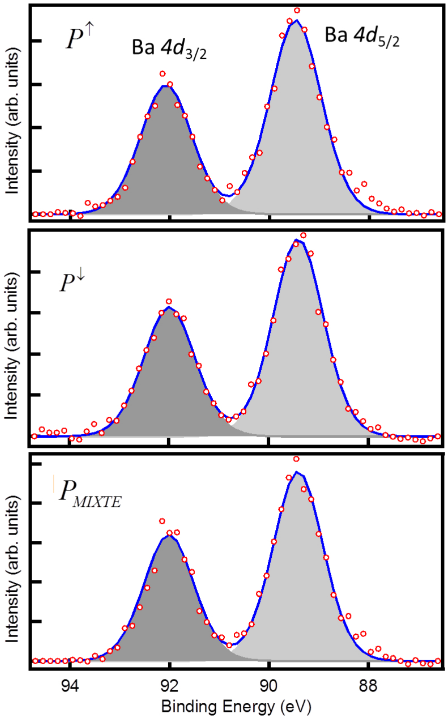

FIGURE 5.11 – *Peak fitting of the Ba 4d core-level spectra extracted for the three electrode switched in three different state of polarization* $P^{\uparrow}$ *(top)* $P^{\downarrow}$ *(middle) and* $P^{\uparrow\downarrow}$ *(bottom).*

experiments can simply be due to the fact that the nature of the samples top electrode, and thus of the measured interface is different (indeed we used a SRO top electrode in the HAXPES experiment, and a Co/Au electrode here). For this reason, the screening by the top electrode will be different, leading to a difference in the resulting polarization-induced shift.

The Ba *4d* core level study does not seem to reveal any interface contribution, contrary to what was observed in the previous HAXPES and time-resolved experiments. The hypothesis is that this contribution exists, but cannot be directly observed, because it is too small in comparaison to the bulk contribution, and/or that the statistics of the HAXPEEM measurement might simply not allow us to resolve the interface component. We tried several fitting procedures including an interface contribution. These tests revealed that the presence of the interface contribution is possible, but its area and exact energy position cannot be precisely obtained. A possibility could have been to use the same fitting parameters than the ones found for the HAXPES study, however, the different nature of the top interface (Co/BTO instead of SRO/BTO) makes any interface comparison between those two experiments impossible. Thus, even if the existence of the interface contribution could be proven, data would still be too scarce to obtain reliable information on the thickness of the interface and its polarization. Follow-up experiments are thus mendatory to clarify this issue.

The results also suggest the existence of a shift between $P^{\uparrow\downarrow}$ and the other two states of polarization. The PFM images showed, in section 5.1.3, that the $P^{\uparrow\downarrow}$ pad has a core shell like behavior, with an external ring in the $P^{\uparrow}$ state and the inside of the pad in the $P^{\downarrow}$ state. This core-shell structure comes from the way the capacitor is switched. This is representated schematically in figure 5.12. As we can see, the tip of the PFM cantilever is applied in the center of the initially $P^{\downarrow}$ capacitor representated in figure 5.12 a). From the position of the tip, the capacitor switches radially to the $P^{\uparrow}$ state, resulting in the $P^{\uparrow\downarrow}$ capacitor, as seen in figure 5.12 b).

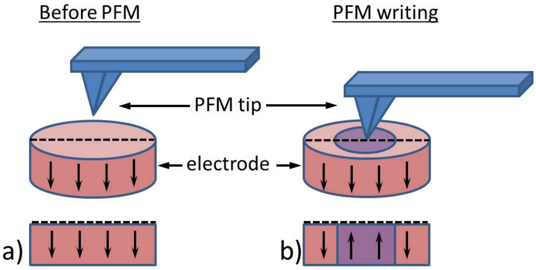

Figure 5.12 – *PFM writing of an electrode from a) the $P^{\downarrow}$ state to b) the $P^{\uparrow\downarrow}$ state.*

We estimated the percentage of each polarization states by calculating from the PFM image the area of the pad related to $P^{\uparrow}$ and $P^{\downarrow}$. The pad is shaped as a circle so we can write the area for $P^{\uparrow}$, $A(P^{\uparrow})$ and $P^{\downarrow}$, $A(P^{\downarrow})$ as:

$$A(P^{\downarrow}) = \pi r_1^2 \tag{5.2}$$
$$A(P^{\uparrow}) = \pi r_2^2 - \pi r_1^2 \tag{5.3}$$

where r_1 is the radius of the inner circle and r_2 the radius of the total pad, as schematized on Figure 5.13.

Assuming a linear relationship, the calculation of $A(P^{\uparrow})$ and $A(P^{\downarrow})$ gives 21.4 % of $P^{\downarrow}$ (and 78.6 % of $P^{\uparrow}$). We now calculated the $P^{\uparrow}$ to $P^{\downarrow}$ repartition from the core level shifts. To do

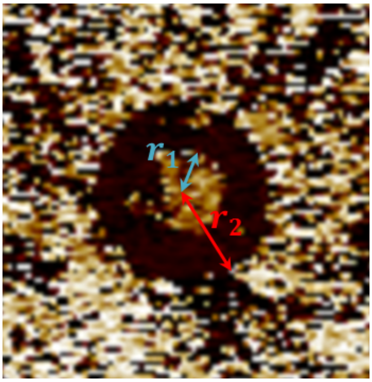

FIGURE 5.13 – *PFM image of the electrode B switched in the* $P^{\uparrow\downarrow}$ *polarization state. The blue arrow indicates* r_1 *the radius of the inner circle in the* $P^{\downarrow}$ *state and the red arrow indicates the radius* r_2 *of the total pad.*

so, we calculated the ratio of the shift between the $P^{\uparrow\downarrow}$ and $P^{\downarrow}$ states (0.022 eV) over the total shift between $P^{\uparrow}$ and $P^{\downarrow}$ (0.150 eV). We found a ratio of 14.6 %. These two values (21.4 % and 14.6 %) are very close given the approximations taken for the calculation of the ratio in PFM (determination of the edge between the $P^{\uparrow}$ and $P^{\downarrow}$ regions, approximation of the domain shapes to perfect circles...). We can thus assume that the energy shift for the electrode in the $P^{\uparrow\downarrow}$ state is symptomatic of the separation of the pad in two regions in the $P^{\uparrow}$ and $P^{\downarrow}$ states.

The binding energy for the Au $4f_{5/2}$ (87.6 eV) core-level is very close to the one of the Ba $4d_{5/2}$ (89.9 eV). However, in the Ba $4d$ core level spectra showed above, the signal coming from the gold is so low with respect to the one coming from the Barium that it is indistinguishable on the spectra. This is incoherent with the relative intensity expected as seen on the SESSA simulation. This leads us to believe that the ROI chosen to performe the analysis probably include part of the bare BTO around the capacitor. To be complete, this study will thus have to be repeated with slightly larger electrodes to avoid this kind of errors.

5.4 Conclusion

In the HAXPEEM experiments, the existence of a shift between $P^{\uparrow}$ and $P^{\downarrow}$ core-level suggests a polarization dependent alteration of the BTO below the electrode. The observation of such a shift in the core levels of a buried interface and on such small electrodes (600 nm in diameters) is a first and great step towards further insight on the behaviour of electrode/FE interfaces using HAXPEEM. However, even if the images were acquired for a total of 18 hours, the number of points by scan had to be limited in order to have a sufficient acquisition time for each point, with acquisition steps of 0.15 eV. Moreover, the statistics of the images is low. When extracting the Ba *4d* spectra from under the electrodes, it is possible that we include part of the bare BTO which is thus not switched in a state of polarization. This could also impair the correct interpretation of the results.

To overcome this limitation due to the low measured signal, new experiments have to be performed with even longer acquisition times. Increasing the number of points per graph would permit a better energy resolution of the graph, thus allowing us to further characterize the interface between the electrode and the ferroelectric. Another possibility to increase the statistics of the experiment would consist in increasing the photon flux. This could be done, for example, by moving the NanoESCA to a different synchrotron beamline with higher flux. However, an increase of the flux comes with the risk of a modification of the sample's polarization properties. In the HAXPES measurements presented in chapter 3, a study of the influence of the beam on the sample's C-V characteristic was performed before the experiment, to ensure that the flux used had no effect on the sample's polarization. Such precaution would be mandatory before considering working with higher photon flux. However, even if increasing the photon flux could be a solution, we should state that it cannot be increased infinitely due to a space charge limitation.

These experiments were a good first step in the study of the BTO/electrode interface using HAXPEEM imaging. We obtained results in agreement with the HAXPES study performed, confirming the alteration of the electrode/BTO interface under the effect of the polarization state. Moreover, we were able to directly link the core level energy shift to the polarization state, using an intermediaite polarization state, $P^{\uparrow\downarrow}$. After the preparation of new samples, the experiments will be repeated, using thicker and thinner top electrodes. However, to remain in the polarization reversal process of "small" electrodes of the theory of Kolmogorov, Avrami and Ishibashi [90–92], their size will have to remain below 1 μm in diameter. On the other hand, decreasing the thickness is possible, but calls for difficult lithography processes that will have to be carefully designed. We should then be able to observe and fully characterize the effect of the polarization on the interface between the FE BTO and the top electrode. Finally, another important aspect of the switching kinetics is the influence of the electrode thickness on the domain wall motion velocity. Indeed, a recent study performed by McGilly *et al.* [191] on $PbZr_{0.1}Ti_{0.9}O_3$ samples showed that in the case of large electrodes, their thickness can influence the velocity of the domain walls up to 7 orders of magnitude. For electrodes of about 100 nm, the study reports a standard velocity of about 1 m/s, whereas is can be as slow as 1 nm/s for 2 nm thick electrodes. The thickness of the electrode must thus also to be carefully taken into account for any switching kinetic studies.

To study the polarization switching kinetics, time-resolved measurements as the ones presented in chapter 4 should be performed on such small sized capacitors. However, HAXPEEM is a very time consuming technique, making these experiments difficult to perform. Moreover, *in situ* bias application in PEEM is possible [192] but has yet to be combined with time-resolved experiment and hard X-ray. Such experiments thus remain a challenge.

Conclusion

The main objective of this work was to further understand the properties of the interface between the ferroelectric and electrodes, as a function of polarization. Indeed, with the increasing necessity for device-like heterostructure in the research field, screening phenomena at the interface of an electrode and a ferroelectric layer comprise a rich topic in material science. In this thesis, the chosen FE was $BaTiO_3$,a prototypical FE. Both the metallic oxide $SrRuO_3$ and the Cobalt were used as electrodes and the screening mechanism has been investigated on BTO thin films.

At the interface between a metallic oxide electrode ($SrRuO_3$) and a BTO thin film, we observed a binding energy shift in the electronic bands for the different polarization states. At the electrode/ferroelectric interface, imperfect screening creates an interface dipole, leading to this shift. The quantitative estimation of the band shift allows an evaluation of the screening capabilities of the given electrode. The $SrRuO_3$ electrodes provide screening via free carriers. Moreover, in the electrode and the ferroelectric, ionic distortion called rumpling is taking place at the interface and helps further screening of the polarization. We measured that the rumpling leads to a modification of the interface in the ferroelectric over 2 to 3 unit cells, and this distortion was observed by transmission electron microscopy. These results are in good agreement with previous theoretical work performed using first principle calculations on the same heterostructure. The ionic relaxation of the SRO interface layer is crucial for the screening of the BTO polarization charges. This is the reason for such a good polarization screening in SRO.

The dynamical process of the polarization switching of such heterostructure was studied using time resolved photoemission spectroscopy, coupled with a P.U.N.D. train of pulses applied *in situ* to our sample. This technique allowed measure the characteristic time of switch from one polarization state to the other to about 50 ns. However, the studied capacitor experience fatigue, leading to a loss of the ferroelectricity due to the high number of polarization switches applied to the sample, and the high bias with respect to the value of the coercive field.

In the case of smaller electrode, i.e. limited to 1 μm in size, the polarization switching process is different than that of larger capacitor (more than 5 μm) [90]. Samples with electrodes of cobalt samller than 1 μm in sizewere studied and the same effect of binding energy shifts is observed.

This thesis shows the potential of photoemission-based techniques for the investigation of ferroelectric materials. Operando photoemission spectroscopy, *i.e.* with in-situ bias, is experimentally challenging to do, and involved designing special sample via several steps of optical lithography. Such measurements give access to electronic and chemical information of an interface in operating conditions. The electron microscopy techniques provide full field, non-contact, spatially-resolved information on the work function, which can be directly related to polarization magnitude, a key quantities for ferroelectric-based devices. These are unique techniques to quantitatively measure such quantity in thin films.

Further work will be carried on by using photoemission microscopy and spectroscopy on other heterostructures, to quantify the dead-layer thickness in FE films. New samples will be designed to answer to limitations based on the used techniques, such as low signal from the studied interface or fatigue in the device. Thinner ferroelectric films will also be used to get to tunneling behavior. Monitoring polarization magnitude in heterostructure with different ferroelectric materials, such as the $PbTiO_3$, would also be interesting to compare the obtained results with other techniques found in the literature.

French Summary

Les dispositifs ferroélectriques sont particulièrement intéressants pour une large gamme d'applications, pour les technologies de l'information. En effet, leur nature non-linéaire peut être utilisée pour fabriquer des condensateurs de capacitance ajustable, avec une haute permittivité en valeur absolue, à des températures proches de la transition de phase. La combinaison de ces propriétés révélées à de petites échelles permet de fabriquer des dispositifs ferroélectriques pour la microélectronique. La polarisation spontanée des matériaux ferroélectriques entraine un effet d'hystérésis pouvant être utilisé comme fonction mémoire, et de tels condensateurs peuvent ainsi être intégrés pour fabriquer des mémoires non volatiles (Random Access Memories).

Dans le cas des films minces, le champ électrique nécessaire pour faire basculer la polarisation d'un état à l'autre peut être atteint à un voltage modéré, typiquement de quelques volts. L'intégration des films minces dans des dispositifs nécessite une attention particulière sur le choix des électrodes, les effets d'interface, et la qualité des échantillons. Basculer la polarisation dans de tels films nécessite un contact métallique, soulevant des problèmes fondamentaux sur le comportement de l'interface entre la couche ferroélectrique et l'électrode. Des expériences *operando*, au cours desquelles la polarisation est basculée *in situ* d'un état à l'autre pendant les mesures, permettent d'étudier cette interface.

Ce manuscrit présente l'étude du film mince ferroélectrique de $BaTiO_3$ par des techniques principalement basées sur la photoémission. Le coeur de cette thèse repose sur l'étude de la structure chimique et électronique de l'interface d'une hétérostructure électrode/$BaTiO_3$/électrode.

Chapitre 1

Le premier chapitre présente les principaux concepts de la ferroélectricité. Les principales propriétés sont illustrées à l'aide d'un matériau ferroélectrique typique, le $BaTiO_3$ (BTO), de structure pérovskite ABO_3. Les différentes théories portant sur la polarisation (la théorie Moderne et celle de Landau) y sont décrites. Comme le besoin de nouveaux dispositifs à l'échelle nanométrique se fait ressentir, de nouvelles problématiques émergent ; ainsi, les concepts d'écrantage du champ dépolarisant, nécessaire au maintien de la polarisation dans le film mince, y sont expliqués. Dans les matériaux ferroélectriques (FE), le champ dépolarisant, qui compense voire supprime la polarisation au sein du matériau, doit être écranté afin de maintenir la polarisation dans les films minces. Divers mécanismes, intrinsèques ou extrinsèques peuvent écranter ce champ dépolarisant, commme l'ajout d'électrodes de part et d'autre du FE. Un état de l'art sur les diverses considérations des hétérostructures électrode/FE/Electrode est donc présenté. Le choix des électrodes, dans le cadre de cette thèse, s'est porté d'une part sur l'oxyde $SrRuO_3$ (SRO), et d'autre part sur le cobalt, l'électrode inférieure étant toujours le SRO.

Chapitre 2

Dans le chapitre 2, les différentes techniques expérimentales utilisées pour caractériser l'interface FE/électrode sont présentées. Tout d'abord, une sélection de techniques souvent utilisées pour caractériser les matériaux ferroélectriques sont décrites, telles que les mesures C-V, I-V, P.U.N.D et la microscopie à force piézoélectrique. Les mesures de C-V et I-V permettent d'obtenir des informations cruciales sur les échantillons, telles que les valeurs de champs coercitifs (*i.e.* la tension nécessaire pour basculer la polarisation d'un état à l'autre), ou la polarisation "built-in" (*i.e.* la direction par défaut de la polarisation, en l'absence de champ électrique, telle qu'induite par les conditions de croissance du matériau considéré).

Le coeur de ce travail repose sur l'utilisation de techniques de photoémission, qui permettent d'obtenir des informations sur l'interface électrode/BTO pour chaque état de polarisation. Ces techniques, basées sur le principe de l'effet photoélectrique donnent des informations chimique et électronique du matériau. Dans le cadre de cette thèse, la Spectroscopie de Photoélectrons est utilisée pour deux régimes : excités par rayons X mous (XPS), et excités par rayons X durs (HAXPES). La microscopie d'électrons photoémis (pour PEEM) est également présentée. La PEEM présente la particularité de conserver la résolution spatiale des photoélectrons. Pour accéder à l'interface électrode/ferroélectrique enfouie, on utilise le PEEM avec, à nouveau, des hautes énergies de photons, dans le régime rayons X durs (HAXPEEM). Certaines de ces techniques ont été utilisées en mode *operando*, ce qui a nécessité l'élaboration d'échantillons spécifiques afin de pouvoir appliquer *in situ* une tension entre les deux électrodes.

Chapitre 3

Une des solutions permettant de stabiliser, ou même d'augmenter la ferroélectricité dans les films d'épaisseurs nanométrique a été apportée par des calculs théoriques. Ces calculs prédisent que l'interface peut impacter de façon significative l'état ferroélectrique initial. Dans cette perspective, pour les films ferroélectriques minces, les métaux purs - qui semblent apparaitre comme le choix le plus logique pour les électrodes - sont souvent remplacés par des oxydes métalliques conducteurs, de sorte à réduire la fatigue dans les dispositifs et améliorer l'épitaxie. Dans le cas d'électrodes permettant des distorsions ioniques, telles que les oxydes conducteurs, un décentrement ionique dans l'électrode, proche de son interface avec le BTO, crée un mécanisme d'écrantage supplémentaire. Les distorsions ioniques et les charges libres de l'électrode se combinent alors pour écranter les charges de polarisation. Comprendre les propriétés électroniques et la structure chimique de l'interface est donc d'une importance majeure dans l'élaboration et l'optimisation des dispositifs. Nous avons utilisé une combinaison d'HAXPES en mode *operando*, de microscopie à effet tunnel (TEM), et de mesures électriques, pour étudier les propriétés de l'interface entre l'électrode supérieure et le film FE (telles que la hauteur de la barrière de Schottky, la modification de l'environnement chimique ou électronique près de l'interface) dans une hétérostructure de SRO/BTO/SRO. Des mesures *operando* sont donc indispensables pour mesurer précisément les différences dans la structure électronique de l'interface en remanence/saturation, où les courants de fuite peuvent jouer un rôle important.

Les résultats montrent que les niveaux de coeur à la rémanence sont quasiment identiques entre les deux états de polarisation, ce qui suggère que la polarisation "built-in" de notre échantillon (dirigé vers la surface) nous empêche d'observer l'état de polarisation $P^{\downarrow}$. Les mesures en saturation montrent que 1,3 (2,6) cellules unitaires dans le BTO sont altérées dans l'état de polarisation $P^{\uparrow}$ ($P^{\downarrow}$) à l'interface SRO/BTO. Les résultats d'HAXPES et les mesures TEM à haute résolution suggèrent tous deux l'hypothèse d'une distorsion atomique se propageant dans le SRO. Une barrière de Schottky pour les électrons de 2,75 (2,15) eV est mesurée à saturation pour l'état de polarisation $P^{\uparrow}$ ($P^{\downarrow}$), ce qui est cohérent avec les mesures électriques macroscopiques. Il n'y a pas d'indication de fuite d'électrons dans le ferroélectrique. Cependant, lorsque la barrière de Schottky est mesurée à l'interface, le décalage de la bande de valence est abaissée à 2,08 (1,49) eV pour l'état de polarisation $P^{\uparrow}$ ($P^{\downarrow}$). Dans le cas d'une polarisation complètement écrantée, nous devrions observer une distorsion ferroélectrique des atomes dans le BTO stabilisée par un écrantage du champ dépolarisant ou des charges de polarisation de surface. Il semble que nos résultats convergent vers l'existence d'une couche d'interface dans le condensateur, où le déplacement des ions Ti est plus faible, entrainant une polarisation plus faible.

Nos résultats expérimentaux sur l'épaisseur de la couche d'interface dans le BTO à l'interface SRO/BTO mesurés par TEM et HAXPES sont en accords avec les calculs théoriques réalisés sur une hétérostructure asymétrique de SRO/BTO/SRO.

Chapitre 4

Dans une seconde étude, la spectroscopie de photoémission résolue en temps, avec application d'une tension *in situ*, a permis l'étude dynamique du basculement de la polarisation dans le SRO/BTO/SRO. Durant cette analyse, l'hétérostructure a été soumise à un train de pulsation "Positive Up Negative Down" (ou P.U.N.D.), et les mesures des niveaux de coeur à l'interface réalisées.

L'étude des niveaux de coeur de Pd *3d* du pad connecté à l'électrode supérieure de SRO a permis d'observer une différence entre le temps caractéristique d'un pulse non-basculant, et d'un pulse basculant du train PUND. L'électrode supérieure étant très fine, on suppose que cette dernière se comporte comme le BTO FE lui-même. Ainsi les déplacements des niveaux de coeur du palladium peuvent être utilisés pour accéder aux informations sur la dynamique de la polarisation du FE. Les déplacements en énergie des niveaux de coeur donnent accès à une constante de 52,7 ns pour le basculement de $P^{\downarrow}$ vers $P^{\uparrow}$ et de 72,1 ns de $P^{\uparrow}$ vers $P^{\downarrow}$. Ces valeurs sont du même ordre de grandeur que celles prédites dans la littérature.

Lors des mesures des courbes C-V réalisées sur le condensateur après les expériences d'XPS résolues en temps, une perte de réponse ferroélectrique a été observée. Elle est probablement due à un phénomène de fatigue diminuant l'amplitude du basculement de la polarisation. La structure étudiée n'a été soumis qu'à 10^4 basculements durant les expériences, soit plusieurs ordres de grandeurs en dessous de la limite habituellement observée. Nous avons utilisé des pulses de 4V pour basculer le condensateur, 4 fois plus grand que le champ coercitif. La combinaison du nombre de basculement et d'une haute valeur de tension appliquée dans nos expériences peut être responsable de la fatigue dans le condensateur étudié et être à l'origine de la perte de ferroélectricité. Pour accéder à davantage d'informations sur la cinétique du basculement de la polarisation, d'autres échantillons, moins sujets à la fatigue, devront être analysés.

Chapitre 5

La théorie classique de nucléation de Kolmogorov, Avrami et Ishibashi considère le basculement de polarisation comme une transition de phase dans un médium infini. Ils introduisent les influences du procédé contrôlant le basculement de polarisation sur son temps caractéristique : dans un grand condensateur (> 1 μm de diamètre), la polarisation est basculée d'abord par la nucléation de nouveau domaines puis par le mouvement des parois de domaines, tandis que pour les plus petites structures ($< 1\ \mu$m de diamètre), le basculement est gouverné par la migration des parois.

Dans ce chapitre, nous nous sommes concentrés sur de petits condensateurs ($< 1\ \mu$m de diamètre), afin d'obtenir des informations sur la réponse de l'interface à la polarisation, dans le cas où son basculement est gouverné par la migration des parois de domaines. Pour cet échantillon, les électrodes supérieures de cobalt faisaient 600 nm de diamètre. Trois condensateurs ont été étudiés : l'un dont la polarisation avait été préalablement basculées vers le bas $P^{\downarrow}$, l'un de polarisation vers le haut $P^{\uparrow}$, et enfin un condensateur dans un état intermédiaire $P^{\uparrow\downarrow}$, où la polarisation préalablement dirigée vers le haut a commencé son basculement vers le bas, de façon incomplète. Pour ces trois condensateurs, l'imagerie HAXPEEM des niveaux de coeur du BTO a été comparée.

L'existence d'un déplacement entre les niveaux de coeur du Ba *3d* $P^{\uparrow}$ et $P^{\downarrow}$ suggère une altération du BTO sous l'électrode dépendant de la polarisation. L'observation d'un tel déplacement en énergie des niveaux de coeur d'une interface enterrée sur de si petites électrodes (600 nm de diamètre) est un premier pas vers une meilleure compréhension du comportement des interfaces électrode/FE. Malgré le long temps d'acquisition (15 minutes par image), la statistique des images est faible. Afin de surpasser les limitations dues au faible signal, de nouvelles expériences devront être réalisées avec des durées d'acquisition encore plus longues. Augmenter le nombre de points par spectre permettrait une meilleur résolution en énergie, permettant donc de mieux caractériser l'interface entre électrode et le ferroélectrique.

Nous avons obtenu des résultats en accord avec les mesures d'HAXPES, confirmant l'existence d'une altération de l'interface électrode/BTO sous l'effet de la polarisation. De plus, nous avons pu lier directement le déplacement en énergie des niveaux de coeur à l'état de polarisation, en utilisant un état intermédiaire, $P^{\uparrow\downarrow}$.

Conclusion

L'objectif principal de ce travail était de mieux connaitre et comprendre les propriétés de l'interface entre le matériau FE et l'électrode en fonction de l'état de polarisation. En effet, avec le besoin croissant de dispositifs performants, les phénomènes d'écrantage à l'interface sont un sujet riche pour les potentielles avancées dans l'utilisation de ces matériaux. A l'interface entre le SRO et le BTO, nous avons pu observer un déplacement en énergie de liaison des bandes électroniques pour les différents états de polarisation.

A l'interface, l'écrantage imparfait entraine un dipôle créant ce déplacement, dont l'estimation quantitative permet d'évaluer la capacité d'écrantage de l'électrode. L'électrode de SRO permet un écrantage grâce aux charges libres et aussi par distorsion ionique à l'interface. On a pu mesurer que cette distorsion ionique entraine une modification à l'interface dans le matériau FE sur 2 à 3 cellules unitaires. Cette distorsion a également pu être observée par TEM. L'étude par HAXPEEM des hétérostructures avec une électrode supérieure de cobalt a montré, à nouveau, l'existence d'un déplacement en énergie de liaison des niveaux de coeur entre les deux états de polarisation, confirmant les résultats obtenus dans le cas d'une électrode de métal pur.

La dynamique du procédé de basculement de la polarisation sur les mêmes hétérostructures a été étudiée par spectroscopie de photoémission résolue en temps, couplée à l'application *in situ* d'un train de pulse de type P.U.N.D. sur notre échantillon. Cette technique nous a permis de mesurer un temps caractéristique de basculement d'un état de polarisation à l'autre d'environ 50 ns. Cependant le condensateur étudié a montré de la fatigue très rapidement au cours de ces premières expériences.

Cette thèse, en cotutelle entre l'Université de Duisburg et l'Université de Paris Saclay, a été réalisée en collaboration entre le Commissariat à l'Energie Atomique et aux Energies Alternatives (CEA) au sein du Service de Physique de l'Etat Condensé (SPEC), et le Peter Grunberg Institut - 6 du centre de recherche de Jülich en Allemagne. Ce travail a également nécessité nombreuses collaborations. Ainsi, le développement du procédé de micro-fabrication et la croissance par déposition par laser pulsé ont été réalisés conjointement avec l'Institut d'Electronique Fondamentale (Université Paris Sud, France). La préparation des électrodes de l'hétérostructure étudiée par PEEM et leur polarisation par PFM ont été réalisées par le groupe de l'Unité Mixte de Physique CNRS/Thales (Palaiseau, France). Enfin, les expériences de spectroscopie de photoémission avec application de tension *in situ* ont été réalisées au synchrotron SOLEIL (Saint-Aubain, France) sur les lignes de lumières TEMPO et GALAXIES, tandis que les expériences de microscopie de photoémission de rayons X durs sur la ligne de lumière P09 du synchrotron PETRA III (Hambourg, Allemagne).

Bibliography

[1] J. F. Scott, *Ferroelectric Memories*, vol. 3 of *Springer Series in Advanced Microelectronics*. Berlin, Heidelberg: Springer Berlin Heidelberg, 2000.

[2] M. Y. Zhuravlev, R. F. Sabirianov, S. S. Jaswal, and E. Y. Tsymbal, "Giant Electroresistance in Ferroelectric Tunnel Junctions," *Physical Review Letters*, vol. 94, p. 246802, June 2005.

[3] M. Dawber, K. M. Rabe, and J. F. Scott, "Physics of thin-film ferroelectric oxides," *Reviews of Modern Physics*, vol. 77, pp. 1083–1130, Oct. 2005.

[4] J. Valasek, "Piezo-Electric and Allied Phenomena in Rochelle Salt," *Physical Review*, vol. 17, pp. 475–481, Apr. 1921.

[5] R. Comès, M. Lambert, and A. Guinier, "Désordre linéaire dans les cristaux (cas du silicium, du quartz, et des pérovskites ferroélectriques)," *Acta Crystallographica Section A: Crystal Physics, Diffraction, Theoretical and General Crystallography*, vol. 26, pp. 244–254, Mar. 1970.

[6] B. Ravel, E. A. Stern, R. I. Vedrinskii, and V. Kraizman, "Local structure and the phase transitions of $BaTiO_3$," *Ferroelectrics*, vol. 206, pp. 407–430, Feb. 1998.

[7] W. Cochran, "Crystal stability and the theory of ferroelectricity," *Advances in Physics*, vol. 9, pp. 387–423, Oct. 1960.

[8] K. M. Rabe, C. H. Ahn, and J.-M. Triscone, "Physics of ferroelectrics - a modern perspective," *Springer*, 2007.

[9] R. Resta, "Macroscopic polarization in crystalline dielectrics: the geometric phase approach," *Reviews of Modern Physics*, vol. 66, pp. 899–915, July 1994.

[10] R. D. King-Smith and D. Vanderbilt, "Theory of polarization of crystalline solids," *Physical Review B*, vol. 47, pp. 1651–1654, Jan. 1993.

[11] J. Zak, "Berry's phase for energy bands in solids," *Physical Review Letters*, vol. 62, pp. 2747–2750, June 1989.

[12] W. Zhong, D. Vanderbilt, and K. M. Rabe, “Phase Transitions in $BaTi0_3$ from First Principles,” *Physical Review Letters*, vol. 73, pp. 1861–1864, Sept. 1994.

[13] W. Zhong, D. Vanderbilt, and K. M. Rabe, “First-principles theory of ferroelectric phase transitions for perovskites: The case of $BaTi0_3$,” *Physical Review B*, vol. 52, pp. 6301–6312, Sept. 1995.

[14] N. Choudhury, L. Walizer, S. Lisenkov, and L. Bellaiche, “Geometric frustration in compositionally modulated ferroelectrics,” *Nature*, vol. 470, pp. 513–517, Feb. 2011.

[15] I. C. Infante, J. Juraszek, S. Fusil, B. Dupé, P. Gemeiner, O. Diéguez, F. Pailloux, S. Jouen, E. Jacquet, G. Geneste, J. Pacaud, J. Iñiguez, L. Bellaiche, A. Barthélémy, B. Dkhil, and M. Bibes, “Multiferroic Phase Transition near Room Temperature in $BiFeO_3$ Films,” *Physical Review Letters*, vol. 107, p. 237601, Nov. 2011.

[16] B. Wul, “Dielectric Constants of Some Titanates,” *Nature*, vol. 156, p. 480, Oct. 1945.

[17] G. H. Kwei, A. C. Lawson, S. J. L. Billinge, and S. W. Cheong, “Structures of the ferroelectric phases of barium titanate,” *The Journal of Physical Chemistry*, vol. 97, pp. 2368–2377, Mar. 1993.

[18] E. A. Stern, “Character of Order-Disorder and Displacive Components in Barium Titanate,” *Physical Review Letters*, vol. 93, p. 037601, July 2004.

[19] P. V. Lambeck and G. H. Jonker, “Ferroelectric domain stabilization in $BaTiO_3$ by bulk ordering of defects,” *Ferroelectrics*, vol. 22, pp. 729–731, Jan. 1978.

[20] T. Shimada, T. Ueda, J. Wang, and T. Kitamura, “Hybrid Hartree-Fock density functional study of charged point defects in ferroelectric $PbTiO_3$,” *Physical Review B*, vol. 87, p. 174111, May 2013.

[21] Y. Wang, X. Liu, J. D. Burton, S. S. Jaswal, and E. Y. Tsymbal, “Ferroelectric Instability Under Screened Coulomb Interactions,” *Physical Review Letters*, vol. 109, p. 247601, Dec. 2012.

[22] R. Moos and K. H. Hardtl, “Defect Chemistry of Donor-Doped and Undoped Strontium Titanate Ceramics between 1000°Cand 1400°C,” *Journal of the American Ceramic Society*, vol. 80, pp. 2549–2562, Oct. 1997.

[23] Y. Mi, G. Geneste, J. E. Rault, C. Mathieu, A. Pancotti, and N. Barrett, “Polarization dependent chemistry of ferroelectric $BaTiO_3$ (001) domains,” *Journal of Physics: Condensed Matter*, vol. 24, no. 27, p. 275901, 2012.

[24] R. V. Wang, D. D. Fong, F. Jiang, M. J. Highland, P. H. Fuoss, C. Thompson, A. M. Kolpak, J. A. Eastman, S. K. Streiffer, A. M. Rappe, and G. B. Stephenson, “Reversible Chemical Switching of a Ferroelectric Film,” *Physical Review Letters*, vol. 102, p. 047601, Jan. 2009.

[25] J. E. Rault, G. Agnus, T. Maroutian, V. Pillard, P. Lecoeur, G. Niu, B. Vilquin, M. G. Silly, A. Bendounan, F. Sirotti, and N. Barrett, "Interface electronic structure in a metal/ferroelectric heterostructure under applied bias," *Physical Review B*, vol. 87, p. 155146, Apr. 2013.

[26] J. Seidel, P. Maksymovych, Y. Batra, A. Katan, S.-Y. Yang, Q. He, A. P. Baddorf, S. V. Kalinin, C.-H. Yang, J.-C. Yang, Y.-H. Chu, E. K. H. Salje, H. Wormeester, M. Salmeron, and R. Ramesh, "Domain Wall Conductivity in La-Doped $BiFeO_3$," *Physical Review Letters*, vol. 105, p. 197603, Nov. 2010.

[27] S. R. Gilbert, L. A. Wills, B. W. Wessels, J. L. Schindler, J. A. Thomas, and C. R. Kannewurf, "Electrical transport properties of epitaxial $BaTiO_3$ thin films," *Journal of Applied Physics*, vol. 80, pp. 969–977, July 1996.

[28] B. Matthias and A. von Hippel, "Domain Structure and Dielectric Response of Barium Titanate Single Crystals," *Physical Review*, vol. 73, pp. 1378–1384, June 1948.

[29] P. W. Forsbergh, "Domain Structures and Phase Transitions in Barium Titanate," *Physical Review*, vol. 76, pp. 1187–1201, Oct. 1949.

[30] T. Mitsui and J. Furuichi, "Domain Structure of Rochelle Salt and KH_2PO_4," *Physical Review*, vol. 90, pp. 193–202, Apr. 1953.

[31] M. J. Highland, T. T. Fister, D. D. Fong, P. H. Fuoss, C. Thompson, J. A. Eastman, S. K. Streiffer, and G. B. Stephenson, "Equilibrium Polarization of Ultrathin $PbTiO_3$ with Surface Compensation Controlled by Oxygen Partial Pressure," *Physical Review Letters*, vol. 107, p. 187602, Oct. 2011.

[32] M. J. Highland, T. T. Fister, M.-I. Richard, D. D. Fong, P. H. Fuoss, C. Thompson, J. A. Eastman, S. K. Streiffer, and G. B. Stephenson, "Polarization Switching without Domain Formation at the Intrinsic Coercive Field in Ultrathin Ferroelectric $PbTiO_3$," *Physical Review Letters*, vol. 105, p. 167601, Oct. 2010.

[33] S. V. Kalinin and D. A. Bonnell, "Local potential and polarization screening on ferroelectric surfaces," *Physical Review B*, vol. 63, p. 125411, Mar. 2001.

[34] C.-L. Wu, P.-W. Lee, Y.-C. Chen, L.-Y. Chang, C.-H. Chen, C.-W. Liang, P. Yu, Q. He, R. Ramesh, and Y.-H. Chu, "Direct spectroscopic evidence of charge reversal at the $Pb(Zr_{0.2}Ti_{0.8})O_3/La_{0.7}Sr_{0.3}MnO_3$ heterointerface," *Physical Review B*, vol. 83, p. 020103, Jan. 2011.

[35] J. Junquera and P. Ghosez, "Critical thickness for ferroelectricity in perovskite ultrathin films," *Nature*, vol. 422, pp. 506–509, Apr. 2003.

[36] M. Stengel, D. Vanderbilt, and N. A. Spaldin, "Enhancement of ferroelectricity at metalâĂŞoxide interfaces," *Nature Materials*, vol. 8, pp. 392–397, May 2009.

[37] I. Ponomareva, I. I. Naumov, I. Kornev, H. Fu, and L. Bellaiche, "Atomistic treatment of depolarizing energy and field in ferroelectric nanostructures," *Physical Review B*, vol. 72, p. 140102, Oct. 2005.

[38] B.-K. Lai, I. Ponomareva, I. Kornev, L. Bellaiche, and G. Salamo, "Thickness dependency of 180° stripe domains in ferroelectric ultrathin films: A first-principles-based study," *Applied Physics Letters*, vol. 91, p. 152909, Oct. 2007.

[39] I. Kornev, H. Fu, and L. Bellaiche, "Ultrathin Films of Ferroelectric Solid Solutions under a Residual Depolarizing Field," *Physical Review Letters*, vol. 93, p. 196104, Nov. 2004.

[40] C. B. Eom, R. J. Cava, R. M. Fleming, J. M. Phillips, R. B. vanDover, J. H. Marshall, J. W. P. Hsu, J. J. Krajewski, and W. F. Peck, "Single-Crystal Epitaxial Thin Films of the Isotropic Metallic Oxides $Sr_{1-x}Ca_xRuO_3$ ($0 \leq x \leq 1$)," *Science*, vol. 258, pp. 1766–1769, Dec. 1992.

[41] D. G. Schlom, L.-Q. Chen, C.-B. Eom, K. M. Rabe, S. K. Streiffer, and J.-M. Triscone, "Strain Tuning of Ferroelectric Thin Films," *Annual Review of Materials Research*, vol. 37, no. 1, pp. 589–626, 2007.

[42] C. B. Eom, R. B. V. Dover, J. M. Phillips, D. J. Werder, J. H. Marshall, C. H. Chen, R. J. Cava, R. M. Fleming, and D. K. Fork, "Fabrication and properties of epitaxial ferroelectric heterostructures with $SrRuO_3$ isotropic metallic oxide electrodes," *Applied Physics Letters*, vol. 63, pp. 2570–2572, Nov. 1993.

[43] J. Wang, H. Zheng, Z. Ma, S. Prasertchoung, M. Wuttig, R. Droopad, J. Yu, K. Eisenbeiser, and R. Ramesh, "Epitaxial $BiFeO_3$ thin films on Si," *Applied Physics Letters*, vol. 85, pp. 2574–2576, Sept. 2004.

[44] T. Kojima, T. Sakai, T. Watanabe, H. Funakubo, K. Saito, and M. Osada, "Large remanent polarization of $(Bi,Nd)_4Ti_3O_{12}$ epitaxial thin films grown by metalorganic chemical vapor deposition," *Applied Physics Letters*, vol. 80, pp. 2746–2748, Apr. 2002.

[45] K. Takahashi, M. Suzuki, T. Kojima, T. Watanabe, Y. Sakashita, K. Kato, O. Sakata, K. Sumitani, and H. Funakubo, "Thickness dependence of dielectric properties in bismuth layer-structured dielectrics," *Applied Physics Letters*, vol. 89, p. 082901, Aug. 2006.

[46] Q. Gan, R. A. Rao, C. B. Eom, L. Wu, and F. Tsui, "Lattice distortion and uniaxial magnetic anisotropy in single domain epitaxial (110) films of $SrRuO_3$," *Journal of Applied Physics*, vol. 85, pp. 5297–5299, Apr. 1999.

[47] C. W. Jones, P. D. Battle, P. Lightfoot, and W. T. A. Harrison, "The structure of $SrRuO_3$ by time-of-flight neutron powder diffraction," *Acta Crystallographica Section C Crystal Structure Communications*, vol. 45, pp. 365–367, Mar. 1989.

[48] B. J. Kennedy and B. A. Hunter, "High-temperature phases of $SrRuO_3$," *Physical Review B*, vol. 58, pp. 653–658, July 1998.

[49] K. J. Choi, S. H. Baek, H. W. Jang, L. J. Belenky, M. Lyubchenko, and C.-B. Eom, "Phase-Transition Temperatures of Strained Single-Crystal $SrRuO_3$ Thin Films," *Advanced Materials*, vol. 22, pp. 759–762, Feb. 2010.

[50] M. Izuha, K. Abe, and N. Fukushima, "Electrical Properties of All-Perovskite Oxide ($SrRuO_3/Ba_xSr_{1-x}TiO_3/SrRuO_3$) Capacitors," *Japanese Journal of Applied Physics*, vol. 36, pp. 5866–5869, Sept. 1997.

[51] V. Nagarajan, J. Junquera, J. Q. He, C. L. Jia, R. Waser, K. Lee, Y. K. Kim, S. Baik, T. Zhao, R. Ramesh, P. Ghosez, and K. M. Rabe, "Scaling of structure and electrical properties in ultrathin epitaxial ferroelectric heterostructures," *Journal of Applied Physics*, vol. 100, p. 051609, Sept. 2006.

[52] P. A. Cox, R. G. Egdell, J. B. Goodenough, A. Hamnett, and C. C. Naish, "The metal-to-semiconductor transition in ternary ruthenium (IV) oxides: a study by electron spectroscopy," *Journal of Physics C: Solid State Physics*, vol. 16, no. 32, p. 6221, 1983.

[53] P. B. Allen, H. Berger, O. Chauvet, L. Forro, T. Jarlborg, A. Junod, B. Revaz, and G. Santi, "Transport properties, thermodynamic properties, and electronic structure of $SrRuO_3$," *Physical Review B*, vol. 53, pp. 4393–4398, Feb. 1996.

[54] D. J. Singh, "Electronic and magnetic properties of the 4d itinerant ferromagnet $SrRuO_3$," *Journal of Applied Physics*, vol. 79, pp. 4818–4820, Apr. 1996.

[55] V. J. Emery and S. A. Kivelson, "Superconductivity in Bad Metals," *Physical Review Letters*, vol. 74, pp. 3253–3256, Apr. 1995.

[56] I. P. Batra, P. Wurfel, and B. D. Silverman, "Depolarization Field and Stability Considerations in Thin Ferroelectric Films," *Journal of Vacuum Science & Technology*, vol. 10, pp. 687–692, Sept. 1973.

[57] R. Ramesh and N. A. Spaldin, "Multiferroics: progress and prospects in thin films," *Nature Materials*, vol. 6, pp. 21–29, Jan. 2007.

[58] D. G. Schlom, L.-Q. Chen, X. Pan, A. Schmehl, and M. A. Zurbuchen, "A Thin Film Approach to Engineering Functionality into Oxides," *Journal of the American Ceramic Society*, vol. 91, pp. 2429–2454, Aug. 2008.

[59] K. J. Choi, M. Biegalski, Y. L. Li, A. Sharan, J. Schubert, R. Uecker, P. Reiche, Y. B. Chen, X. Q. Pan, V. Gopalan, L.-Q. Chen, D. G. Schlom, and C. B. Eom, "Enhancement of Ferroelectricity in Strained $BaTiO_3$ Thin Films," *Science*, vol. 306, pp. 1005–1009, Nov. 2004.

[60] M. Bibes, "Nanoferronics is a winning combination," *Nature Materials*, vol. 11, pp. 354–357, May 2012.

[61] J. F. Scott, "Applications of modern ferroelectrics," *Science (New York, N.Y.)*, vol. 315, pp. 954–959, Feb. 2007.

[62] V. Garcia, S. Fusil, K. Bouzehouane, S. Enouz-Vedrenne, N. D. Mathur, A. Barthélémy, and M. Bibes, "Giant tunnel electroresistance for non-destructive readout of ferroelectric states," *Nature*, vol. 460, pp. 81–84, July 2009.

[63] R. R. Mehta, B. D. Silverman, and J. T. Jacobs, "Depolarization fields in thin ferroelectric films," *Journal of Applied Physics*, vol. 44, pp. 3379–3385, Aug. 1973.

[64] V. Garcia and M. Bibes, "Ferroelectric tunnel junctions for information storage and processing," *Nature Communications*, vol. 5, p. 4289, July 2014.

[65] N. Sai, A. M. Kolpak, and A. M. Rappe, "Ferroelectricity in ultrathin perovskite films," *Physical Review B*, vol. 72, p. 020101, July 2005.

[66] Y. Umeno, B. Meyer, C. Elsässer, and P. Gumbsch, "*Ab initio* study of the critical thickness for ferroelectricity in ultrathin Pt/$PbTiO_3$/Pt films," *Physical Review B*, vol. 74, p. 060101, Aug. 2006.

[67] B. Meyer and D. Vanderbilt, "*Ab initio* study of $BaTiO_3$ and $PbTiO_3$ surfaces in external electric fields," *Physical Review B*, vol. 63, p. 205426, May 2001.

[68] B. Meyer and D. Vanderbilt, "*Ab initio* study of ferroelectric domain walls in $PbTiO_3$," *Physical Review B*, vol. 65, p. 104111, Mar. 2002.

[69] S. Prosandeev, S. Lisenkov, and L. Bellaiche, "Kittel Law in $BiFeO_3$ Ultrathin Films: A First-Principles-Based Study," *Physical Review Letters*, vol. 105, p. 147603, Sept. 2010.

[70] E. Almahmoud, "Dependence of Curie temperature on the thickness of an ultrathin ferroelectric film," *Physical Review B*, vol. 81, no. 6, 2010.

[71] D. D. Fong, G. B. Stephenson, S. K. Streiffer, J. A. Eastman, O. Auciello, P. H. Fuoss, and C. Thompson, "Ferroelectricity in Ultrathin Perovskite Films," *Science*, vol. 304, pp. 1650–1653, June 2004.

[72] H. Béa, S. Fusil, K. Bouzehouane, M. Bibes, M. Sirena, G. Herranz, E. Jacquet, J.-P. Contour, and A. Barthélémy, "Ferroelectricity Down to at Least 2 nm in Multiferroic $BiFeO_3$ Epitaxial Thin Films," *Japanese Journal of Applied Physics*, vol. 45, pp. L187–L189, Feb. 2006.

[73] G. Catalan, H. Béa, S. Fusil, M. Bibes, P. Paruch, A. Barthélémy, and J. F. Scott, "Fractal Dimension and Size Scaling of Domains in Thin Films of Multiferroic $BiFeO_3$," *Physical Review Letters*, vol. 100, p. 027602, Jan. 2008.

[74] Y. H. Chu, T. Zhao, M. P. Cruz, Q. Zhan, P. L. Yang, L. W. Martin, M. Huijben, C. H. Yang, F. Zavaliche, H. Zheng, and R. Ramesh, "Ferroelectric size effects in multiferroic $BiFeO_3$ thin films," *Applied Physics Letters*, vol. 90, p. 252906, June 2007.

[75] V. Garcia, M. Bibes, L. Bocher, S. Valencia, F. Kronast, A. Crassous, X. Moya, S. Enouz-Vedrenne, A. Gloter, D. Imhoff, C. Deranlot, N. D. Mathur, S. Fusil, K. Bouzehouane, and A. Barthélémy, "Ferroelectric Control of Spin Polarization," *Science*, vol. 327, pp. 1106–1110, Feb. 2010.

[76] D. H. Kim, H. N. Lee, M. D. Biegalski, and H. M. Christen, "Effect of epitaxial strain on ferroelectric polarization in multiferroic $BiFeO_3$ films," *Applied Physics Letters*, vol. 92, p. 012911, Jan. 2008.

[77] C. Lichtensteiger, J.-M. Triscone, J. Junquera, and P. Ghosez, "Ferroelectricity and Tetragonality in Ultrathin $PbTiO_3$ Films," *Physical Review Letters*, vol. 94, p. 047603, Feb. 2005.

[78] P. Maksymovych, M. Huijben, M. Pan, S. Jesse, N. Balke, Y.-H. Chu, H. J. Chang, A. Y. Borisevich, A. P. Baddorf, G. Rijnders, D. H. A. Blank, R. Ramesh, and S. V. Kalinin, "Ultrathin limit and dead-layer effects in local polarization switching of $BiFeO_3$," *Physical Review B*, vol. 85, p. 014119, Jan. 2012.

[79] T. Tybell, C. H. Ahn, and J.-M. Triscone, "Ferroelectricity in thin perovskite films," *Applied Physics Letters*, vol. 75, pp. 856–858, Aug. 1999.

[80] F. Rao, M. Kim, A. J. Freeman, S. Tang, and M. Anthony, "Structural and electronic properties of transition-metal/$BaTiO_3$(001) interfaces," *Physical Review B*, vol. 55, pp. 13953–13960, May 1997.

[81] H. Kohlstedt, N. A. Pertsev, J. Rodriguez Contreras, and R. Waser, "Theoretical current-voltage characteristics of ferroelectric tunnel junctions," *Physical Review B*, vol. 72, p. 125341, Sept. 2005.

[82] C.-G. Duan, S. S. Jaswal, and E. Y. Tsymbal, "Predicted Magnetoelectric Effect in Fe/$BaTiO_3$ Multilayers: Ferroelectric Control of Magnetism," *Physical Review Letters*, vol. 97, p. 047201, July 2006.

[83] G. Gerra, A. K. Tagantsev, N. Setter, and K. Parlinski, "Ionic Polarizability of Conductive Metal Oxides and Critical Thickness for Ferroelectricity in $BaTiO_3$," *Physical Review Letters*, vol. 96, p. 107603, Mar. 2006.

[84] N. Bergeard, M. G. Silly, D. Krizmancic, C. Chauvet, M. Guzzo, J. P. Ricaud, M. Izquierdo, L. Stebel, P. Pittana, R. Sergo, G. Cautero, G. Dufour, F. Rochet, and F. Sirotti, "Time-resolved photoelectron spectroscopy using synchrotron radiation time structure," *Journal of Synchrotron Radiation*, vol. 18, pp. 245–250, Mar. 2011.

[85] E. Bauer, “A brief history of PEEM,” *Journal of Electron Spectroscopy and Related Phenomena*, vol. 185, pp. 314–322, Oct. 2012.

[86] D. I. Bilc, F. D. Novaes, J. Iñiguez, P. Ordejón, and P. Ghosez, “Electroresistance Effect in Ferroelectric Tunnel Junctions with Symmetric Electrodes,” *ACS Nano*, vol. 6, pp. 1473–1478, Feb. 2012.

[87] M. Born, “Eine thermochemischemische anwendung der gittertheorie.,” *Verh Dutsch Physik Ges*, vol. 21, pp. 13–24, 1919.

[88] E. Bauer, “Low energy electron microscopy,” *Reports on Progress in Physics*, vol. 57, no. 9, p. 895, 1994.

[89] A. Pancotti, J. Wang, P. Chen, L. Tortech, C.-M. Teodorescu, E. Frantzeskakis, and N. Barrett, “X-ray photoelectron diffraction study of relaxation and rumpling of ferroelectric domains in $BaTiO_3$ (001),” *Physical Review B*, vol. 87, p. 184116, May 2013.

[90] Y. Ishibashi and Y. Takagi, “Note on Ferroelectric Domain Switching,” *Journal of the Physical Society of Japan*, vol. 31, pp. 506–510, Aug. 1971.

[91] A. Kolmogorov, “A statistical theory for the recrystallisation of metals, Akad Nauk SSSR, Izv,” *Izv. Akad. Nauk. SSSR*, vol. 3, 1937.

[92] M. Avrami, “Kinetics of Phase Change. I General Theory,” *The Journal of Chemical Physics*, vol. 7, pp. 1103–1112, Dec. 1939.

[93] M. Arenstein, “Instability in Crystals and Thermal Expansion Coefficients,” *Physical Review*, vol. 133, pp. A1034–A1037, Feb. 1964.

[94] A. K. Tagantsev, I. Stolichnov, N. Setter, J. S. Cross, and M. Tsukada, “Non-Kolmogorov-Avrami switching kinetics in ferroelectric thin films,” *Physical Review B*, vol. 66, p. 214109, Dec. 2002.

[95] D. J. Jung, M. Dawber, A. Ruediger, J. F. Scott, H. H. Kim, and K. Kim, “Dielectric loss peak due to platinum electrode porosity in lead zirconate titanate thin-film capacitors,” *Applied Physics Letters*, vol. 81, pp. 2436–2438, Sept. 2002.

[96] M. Dawber, D. J. Jung, and J. F. Scott, “Perimeter effect in very small ferroelectrics,” *Applied Physics Letters*, vol. 82, pp. 436–438, Jan. 2003.

[97] S. Tiedke, T. Schmitz, K. Prume, A. Roelofs, T. Schneller, U. Kall, R. Waser, C. S. Ganpule, V. Nagarajan, A. Stanishevsky, and R. Ramesh, “Direct hysteresis measurements of single nanosized ferroelectric capacitors contacted with an atomic force microscope,” *Applied Physics Letters*, vol. 79, pp. 3678–3680, Nov. 2001.

[98] S. Prasertchoung, V. Nagarajan, Z. Ma, R. Ramesh, J. S. Cross, and M. Tsukada, “Polarization switching of submicron ferroelectric capacitors using an atomic force microscope,” *Applied Physics Letters*, vol. 84, pp. 3130–3132, Apr. 2004.

[99] C. B. Sawyer and C. H. Tower, “Rochelle Salt as a Dielectric,” *Physical Review*, vol. 35, pp. 269–273, Feb. 1930.

[100] R. Bouregba, B. Vilquin, G. L. Rhun, G. Poullain, and B. Domenges, “Sawyer-Tower hysteresis measurements on micron sized Pb(Zr,Ti)O_3 capacitors,” *Review of Scientific Instruments*, vol. 74, pp. 4429–4435, Oct. 2003.

[101] J. F. Scott, “Ferroelectrics go bananas,” *Journal of Physics: Condensed Matter*, vol. 20, no. 2, p. 021001, 2008.

[102] S. D. Traynor, T. D. Hadnagy, and L. Kammerdiner, “Capacitor test simulation of retention and imprint characteristics for ferroelectric memory operation,” *Integrated Ferroelectrics*, vol. 16, pp. 63–76, Apr. 1997.

[103] K. Abe, N. Yanase, and T. Kawakubo, “Asymmetric Switching of Ferroelectric Polarization in a Heteroepitaxial $BaTiO_3$ Thin Film Capacitor,” *Japanese Journal of Applied Physics*, vol. 39, pp. 4059–4063, July 2000.

[104] H. Ishii, T. Nakajima, Y. Takahashi, and T. Furukawa, “Ultrafast Polarization Switching in Ferroelectric Polymer Thin Films at Extremely High Electric Fields,” *Applied Physics Express*, vol. 4, p. 031501, Mar. 2011.

[105] S. Zhukov, Y. A. Genenko, O. Hirsch, J. Glaum, T. Granzow, and H. von Seggern, “Dynamics of polarization reversal in virgin and fatigued ferroelectric ceramics by inhomogeneous field mechanism,” *Physical Review B*, vol. 82, p. 014109, July 2010.

[106] C. J. Brennan, “Characterization and modelling of thin-film ferroelectric capacitors using C-V analysis,” *Integrated Ferroelectrics*, vol. 2, pp. 73–82, Nov. 1992.

[107] L. Pintilie and M. Alexe, “Metal-ferroelectric-metal heterostructures with Schottky contacts. I. Influence of the ferroelectric properties,” *Journal of Applied Physics*, vol. 98, p. 124103, Dec. 2005.

[108] L. Pintilie, I. Boerasu, M. J. M. Gomes, T. Zhao, R. Ramesh, and M. Alexe, “Metal-ferroelectric-metal structures with Schottky contacts. II. Analysis of the experimental current-voltage and capacitance-voltage characteristics of Pb(Zr,Ti)O_3 thin films,” *Journal of Applied Physics*, vol. 98, p. 124104, Dec. 2005.

[109] L. Pintilie, I. Vrejoiu, D. Hesse, G. LeRhun, and M. Alexe, “Ferroelectric polarization-leakage current relation in high quality epitaxial Pb(Zr,Ti)O_3 films,” *Physical Review B*, vol. 75, p. 104103, Mar. 2007.

[110] E. Soergel, “Piezoresponse force microscopy (PFM),” *Journal of Physics D: Applied Physics*, vol. 44, no. 46, p. 464003, 2011.

[111] A. Gruverman, D. Wu, and J. F. Scott, “Piezoresponse Force Microscopy Studies of Switching Behavior of Ferroelectric Capacitors on a 100-ns Time Scale,” *Physical Review Letters*, vol. 100, p. 097601, Mar. 2008.

[112] B. B. Tian, J. L. Wang, S. Fusil, Y. Liu, X. L. Zhao, S. Sun, H. Shen, T. Lin, J. L. Sun, C. G. Duan, M. Bibes, A. Barthélémy, B. Dkhil, V. Garcia, X. J. Meng, and J. H. Chu, “Tunnel electroresistance through organic ferroelectrics,” *Nature Communications*, vol. 7, p. 11502, May 2016.

[113] H. Hertz, “Über einen einfluss des ultravioletten lichtes auf die electrische entladung.,” *Annalen der Physik*, vol. 267(8), pp. 983–1000, 1887.

[114] A. Einstein, “Über einen die Erzeugung und Verwandlung des Lichtes betreffenden heuristischen Gesichtspunkt,” *Annalen der Physik*, vol. 322, pp. 132–148, Jan. 1905.

[115] A. H. Compton, “A Quantum Theory of the Scattering of X-rays by Light Elements,” *Physical Review*, vol. 21, pp. 483–502, May 1923.

[116] C. Nordling, E. Sokolowski, and K. Siegbahn, “Precision Method for Obtaining Absolute Values of Atomic Binding Energies,” *Physical Review*, vol. 105, pp. 1676–1677, Mar. 1957.

[117] J. C. Woicik, *Hard X-ray Photoelectron Spectroscopy (HAXPES).* Springer, Dec. 2015. Google-Books-ID: yYlNCwAAQBAJ.

[118] P. H. Citrin and G. K. Wertheim, “Photoemission from surface-atom core levels, surface densities of states, and metal-atom clusters: A unified picture,” *Physical Review B*, vol. 27, pp. 3176–3200, Mar. 1983.

[119] R. Courths and S. Hüfner, “Photoemission experiments on copper,” *Physics Reports*, vol. 112, pp. 53–171, Oct. 1984.

[120] S. Hüfner, “Photoelectron spectroscopy,” *Springer, 3rd revised and enlarged edition*, 2003.

[121] C. S. Fadley, R. J. Baird, W. Siekhaus, T. Novakov, and S. A. L. Bergström, “Surface analysis and angular distributions in x-ray photoelectron spectroscopy,” *Journal of Electron Spectroscopy and Related Phenomena*, vol. 4, pp. 93–137, Jan. 1974.

[122] C. S. Fadley, “Angle-resolved x-ray photoelectron spectroscopy,” *Progress in Surface Science*, vol. 16, pp. 275–388, Jan. 1984.

[123] I. Adawi, “Theory of the Surface Photoelectric Effect for One and Two Photons,” *Physical Review*, vol. 134, pp. A788–A798, May 1964.

[124] J. B. Pendry, “Theory of photoemission,” *Surface Science*, vol. 57, pp. 679–705, July 1976.

[125] T. Koopmans, “Über die zuordnung von wellenfunktionen und eigenwerten zu den einzelnen elektronen eines atoms.,” *Physica*, vol. 1(1-6), pp. 104–113, 1934.

[126] J. J. Yeh and I. Lindau, "Atomic subshell photoionization cross sections and asymmetry parameters: $1 \leq Z \leq 103$," *Atomic Data and Nuclear Data Tables*, vol. 32, pp. 1–155, Jan. 1985.

[127] J. H. Hubbell, H. A. Gimm, and I. O/verbo, "Pair, Triplet, and Total Atomic Cross Sections (and Mass Attenuation Coefficients) for 1 MeV -Ř100 GeV Photons in Elements Z=1 to 100," *Journal of Physical and Chemical Reference Data*, vol. 9, pp. 1023–1148, Oct. 1980.

[128] D. A. Shirley, "High-Resolution X-Ray Photoemission Spectrum of the Valence Bands of Gold," *Physical Review B*, vol. 5, pp. 4709–4714, June 1972.

[129] F. Haber, "Theory of the heat of reaction," *Verhandl Deut Phys Ges*, vol. 21, pp. 750–768, 1919.

[130] L. T. Hudson, R. L. Kurtz, S. W. Robey, D. Temple, and R. L. Stockbauer, "Photoelectron spectroscopic study of the valence and core-level electronic structure of $BaTiO_3$," *Physical Review B*, vol. 47, pp. 1174–1180, Jan. 1993.

[131] G. M. Vanacore, L. F. Zagonel, and N. Barrett, "Surface enhanced covalency and Madelung potentials in Nb doped $SrTiO_3$ (100), (110) and (111) single crystals," *Surface Science*, vol. 604, pp. 1674–1683, Sept. 2010.

[132] L. Kornblum, J. A. Rothschild, Y. Kauffmann, R. Brener, and M. Eizenberg, "Band offsets and Fermi level pinning at metal-Al_2O_3 interfaces," *Physical Review B*, vol. 84, p. 155317, Oct. 2011.

[133] K. Horn, "Photoemission studies of barrier heights in metal/semiconductor interfaces and heterojunctions," *Applied Surface Science*, vol. 166, pp. 1–11, Oct. 2000.

[134] K. Horn, M. Moreno, M. Alonso, M. Höricke, R. Hey, J. L. Sacedon, and K. H. Ploog, "Photoelectron emission from heterojunctions with intralayers: band-offset changes vs. band-bending effects," *Vacuum*, vol. 67, pp. 115–123, Sept. 2002.

[135] L. Q. Zhu, N. Barrett, P. Jegou, F. Martin, C. Leroux, E. Martinez, H. Grampeix, O. Renault, and A. Chabli, "X-ray photoelectron spectroscopy and ultraviolet photoelectron spectroscopy investigation of Al-related dipole at the HfO_2/Si interface," *Journal of Applied Physics*, vol. 105, p. 024102, Jan. 2009.

[136] J. H. Lambert, "Photometria, sive de mensura et gradibus luminis, colorum et umbrae," *Augsburg*, 1760.

[137] C. R. Brundle, "Elucidation of surface structure and bonding by photoelectron spectroscopy?," *Surface Science*, vol. 48, pp. 99–136, Mar. 1975.

[138] G. Panaccione and K. Kobayashi, “Hard X-ray photoemission spectroscopy: Variable depth analysis of bulk, surface and interface electronic properties,” *Surface Science*, vol. 606, pp. 125–129, Feb. 2012.

[139] C. S. Fadley, “X-ray photoelectron spectroscopy: Progress and perspectives,” *Journal of Electron Spectroscopy and Related Phenomena*, vol. 178-179, pp. 2–32, May 2010.

[140] K. Kobayashi, “Hard x-ray photoemission spectroscopy,” *Nuclear Instruments and Methods in Physics Research A*, vol. 601, p. 32, 2009.

[141] W. Smekal, W. S. M. Werner, and C. J. Powell, “Simulation of electron spectra for surface analysis (SESSA): a novel software tool for quantitative Auger-electron spectroscopy and X-ray photoelectron spectroscopy,” *Surface and Interface Analysis*, vol. 37, pp. 1059–1067, Nov. 2005.

[142] S. Suzer, E. Abelev, and S. L. Bernasek, “Impedance-type measurements using XPS,” *Applied Surface Science*, vol. 256, pp. 1296–1298, Dec. 2009.

[143] T. Nagata, M. Haemori, Y. Yamashita, H. Yoshikawa, Y. Iwashita, K. Kobayashi, and T. Chikyow, “Oxygen migration at Pt/HfO_2/Pt interface under bias operation,” *Applied Physics Letters*, vol. 97, p. 082902, Aug. 2010.

[144] T. Nagata, M. Haemori, Y. Yamashita, H. Yoshikawa, Y. Iwashita, K. Kobayashi, and T. Chikyow, “Bias application hard x-ray photoelectron spectroscopy study of forming process of Cu/HfO_2/Pt resistive random access memory structure,” *Applied Physics Letters*, vol. 99, p. 223517, Nov. 2011.

[145] F. Chen and A. Klein, “Polarization dependence of Schottky barrier heights at interfaces of ferroelectrics determined by photoelectron spectroscopy,” *Physical Review B*, vol. 86, p. 094105, Sept. 2012.

[146] E. Brüche, “Elektronenmikroskopische abbildung mit lichtelektrischen elektronen.,” *Zeitschrift für Physik*, vol. 86, pp. 448–450, 1933.

[147] G. F. Rempfer and O. Hayes Griffith, “Emission microscopy and related techniques: Resolution in photoelectron microscopy, low energy electron microscopy and mirror electron microscopy,” *Ultramicroscopy*, vol. 47, pp. 35–54, Nov. 1992.

[148] W. Telieps and E. Bauer, “An analytical reflection and emission UHV surface electron microscope,” *Ultramicroscopy*, vol. 17, pp. 57–65, Jan. 1985.

[149] J. Stohr, Y. Wu, B. D. Hermsmeier, M. G. Samant, G. R. Harp, S. Koranda, D. Dunham, and B. P. Tonner, “Element-Specific Magnetic Microscopy with Circularly Polarized X-Rays,” *Science*, vol. 259, pp. 658–661, Jan. 1993.

[150] M. Escher, K. Winkler, O. Renault, and N. Barrett, “Applications of high lateral and energy resolution imaging XPS with a double hemispherical analyser based spectromicroscope,” *Journal of Electron Spectroscopy and Related Phenomena*, vol. 178-179, pp. 303–316, May 2010.

[151] E. Bauer, “Photoelectron spectromicroscopy: present and future,” *Journal of Electron Spectroscopy and Related Phenomena*, vol. 114-116, pp. 975–987, Mar. 2001.

[152] B. P. Tonner, D. Dunham, T. Droubay, and M. Pauli, “A photoemission microscope with a hemispherical capacitor energy filter,” *Journal of Electron Spectroscopy and Related Phenomena*, vol. 84, pp. 211–229, Mar. 1997.

[153] R. M. Tromp, J. B. Hannon, A. W. Ellis, W. Wan, A. Berghaus, and O. Schaff, “A new aberration-corrected, energy-filtered LEEM/PEEM instrument. I. Principles and design,” *Ultramicroscopy*, vol. 110, pp. 852–861, June 2010.

[154] M. Escher, N. Weber, M. Merkel, C. Ziethen, P. Bernhard, G. Schönhense, S. Schmidt, F. Forster, F. Reinert, B. Krömker, and D. Funnemann, “NanoESCA: a novel energy filter for imaging x-ray photoemission spectroscopy,” *Journal of Physics: Condensed Matter*, vol. 17, no. 16, p. S1329, 2005.

[155] L. F. Zagonel, N. Barrett, O. Renault, A. Bailly, M. Bäurer, M. Hoffmann, S.-J. Shih, and D. Cockayne, “Orientation-dependent surface composition of in situ annealed strontium titanate,” *Surface and Interface Analysis*, vol. 40, pp. 1709–1712, Dec. 2008.

[156] C. Mathieu, N. Barrett, J. Rault, Y. Y. Mi, B. Zhang, W. A. de Heer, C. Berger, E. H. Conrad, and O. Renault, “Microscopic correlation between chemical and electronic states in epitaxial graphene on SiC(000-1),” *Physical Review B*, vol. 83, p. 235436, June 2011.

[157] A. Damascelli, “Probing the Electronic Structure of Complex Systems by ARPES,” *Physica Scripta*, vol. T109, p. 61, 2004.

[158] M. Patt, C. Wiemann, N. Weber, M. Escher, A. Gloskovskii, W. Drube, M. Merkel, and C. M. Schneider, “Bulk sensitive hard x-ray photoemission electron microscopy,” *Review of Scientific Instruments*, vol. 85, p. 113704, Nov. 2014.

[159] A. Chanthbouala, V. Garcia, R. O. Cherifi, K. Bouzehouane, S. Fusil, X. Moya, S. Xavier, H. Yamada, C. Deranlot, N. D. Mathur, M. Bibes, A. Barthelemy, and J. Grollier, “A ferroelectric memristor,” *Nature Materials*, vol. 11, pp. 860–864, Oct. 2012.

[160] C. H. Ahn, R. H. Hammond, T. H. Geballe, M. R. Beasley, J.-M. Triscone, M. Decroux, O. Fischer, L. Antognazza, and K. Char, “Ferroelectric field effect in ultrathin $SrRuO_3$ films,” *Applied Physics Letters*, vol. 70, pp. 206–208, Jan. 1997.

[161] X. D. Wu, S. R. Foltyn, R. C. Dye, Y. Coulter, and R. E. Muenchausen, “Properties of epitaxial $SrRuO_3$ thin films,” *Applied Physics Letters*, vol. 62, pp. 2434–2436, May 1993.

[162] C. L. Chen, Y. Cao, Z. J. Huang, Q. D. Jiang, Z. Zhang, Y. Y. Sun, W. N. Kang, L. M. Dezaneti, W. K. Chu, and C. W. Chu, "Epitaxial $SrRuO_3$ thin films on (001) $SrTiO_3$," *Applied Physics Letters*, vol. 71, pp. 1047–1049, Aug. 1997.

[163] B. Chrisey and K. Graham, "Pulsed laser deposition of thin films," *John Wiley & Sons*, vol. 1, 1994.

[164] F. Granozio, "In situ investigation of surface oxygen vacancies in perovskites," *Materials Research Society Symposium Proceedings*, vol. E, 2006.

[165] G. J. H. M. Rijnders, G. Koster, D. H. A. Blank, and H. Rogalla, "In situ monitoring during pulsed laser deposition of complex oxides using reflection high energy electron diffraction under high oxygen pressure," *Applied Physics Letters*, vol. 70, pp. 1888–1890, Apr. 1997.

[166] M. Stengel, P. Aguado-Puente, N. A. Spaldin, and J. Junquera, "Band alignment at metal/ferroelectric interfaces: Insights and artifacts from first principles," *Physical Review B*, vol. 83, p. 235112, June 2011.

[167] A. K. Tagantsev, G. Gerra, and N. Setter, "Short-range and long-range contributions to the size effect in metal-ferroelectric-metal heterostructures," *Physical Review B*, vol. 77, p. 174111, May 2008.

[168] A. K. Tagantsev and G. Gerra, "Interface-induced phenomena in polarization response of ferroelectric thin films," *Journal of Applied Physics*, vol. 100, p. 051607, Sept. 2006.

[169] C. T. Black and J. J. Welser, "Electric-field penetration into metals: consequences for high-dielectric-constant capacitors," *IEEE Transactions on Electron Devices*, vol. 46, pp. 776–780, Apr. 1999.

[170] J. Shin, A. Y. Borisevich, V. Meunier, J. Zhou, E. W. Plummer, S. V. Kalinin, and A. P. Baddorf, "Oxygen-Induced Surface Reconstruction of $SrRuO_3$ and Its Effect on the $BaTiO_3$ Interface," *ACS Nano*, vol. 4, pp. 4190–4196, July 2010.

[171] M. Kawasaki, K. Takahashi, T. Maeda, R. Tsuchiya, M. Shinohara, O. Ishiyama, T. Yonezawa, M. Yoshimoto, and H. Koinuma, "Atomic Control of the $SrTiO_3$ Crystal Surface," *Science*, vol. 266, pp. 1540–1542, Dec. 1994.

[172] X. J. Lou, "Polarization fatigue in ferroelectric thin films and related materials," *Journal of Applied Physics*, vol. 105, p. 024101, Jan. 2009.

[173] E. Kröger, A. Petraru, A. Quer, R. Soni, M. Kalläne, N. A. Pertsev, H. Kohlstedt, and K. Rossnagel, "In situ hard x-ray photoemission spectroscopy of barrier-height control at metal/PMN-PT interfaces," *Physical Review B*, vol. 93, p. 235415, June 2016.

[174] P. Ghosez, J.-P. Michenaud, and X. Gonze, "Dynamical atomic charges: The case of ABO_3 compounds," *Physical Review B*, vol. 58, pp. 6224–6240, Sept. 1998.

[175] H. Lu, X. Liu, J. D. Burton, C.-W. Bark, Y. Wang, Y. Zhang, D. J. Kim, A. Stamm, P. Lukashev, D. A. Felker, C. M. Folkman, P. Gao, M. S. Rzchowski, X. Q. Pan, C.-B. Eom, E. Y. Tsymbal, and A. Gruverman, "Enhancement of Ferroelectric Polarization Stability by Interface Engineering," *Advanced Materials*, vol. 24, pp. 1209–1216, Mar. 2012.

[176] E. A. Kraut, R. W. Grant, J. R. Waldrop, and S. P. Kowalczyk, "Precise Determination of the Valence-Band Edge in X-Ray Photoemission Spectra: Application to Measurement of Semiconductor Interface Potentials," *Physical Review Letters*, vol. 44, pp. 1620–1623, June 1980.

[177] S. H. Wemple, "Polarization Fluctuations and the Optical-Absorption Edge in $BaTiO_3$," *Physical Review B*, vol. 2, pp. 2679–2689, Oct. 1970.

[178] S. Sze and K. Ng, "Physics of semiconductor devices.," *John Wiley & Sons*, 2006.

[179] D. Bagayoko, G. L. Zhao, J. D. Fan, and J. T. Wang, "Ab initio calculations of the electronic structure and optical properties of ferroelectric tetragonal $BaTiO_3$," *Journal of Physics: Condensed Matter*, vol. 10, no. 25, p. 5645, 1998.

[180] W. Wunderlich, H. Ohta, and K. Koumoto, "Enhanced effective mass in doped $SrTiO_3$ and related perovskites," *Physica B: Condensed Matter*, vol. 404, pp. 2202–2212, Aug. 2009.

[181] N.-H. Chan, R. Sharma, and D. Smyth, "Nonstoichiometry in Undoped $BaTiO_3$," *Journal of the American Ceramic Society*, vol. 64, pp. 556–562, Sept. 1981.

[182] P. Erhart and K. Albe, "Modeling the electrical conductivity in $BaTiO_3$ on the basis of first-principles calculations," *Journal of Applied Physics*, vol. 104, p. 044315, Aug. 2008.

[183] H. J. Chang, S. V. Kalinin, A. N. Morozovska, M. Huijben, Y.-H. Chu, P. Yu, R. Ramesh, E. A. Eliseev, G. S. Svechnikov, S. J. Pennycook, and A. Y. Borisevich, "Atomically Resolved Mapping of Polarization and Electric Fields Across Ferroelectric/Oxide Interfaces by Z-contrast Imaging," *Advanced Materials*, vol. 23, pp. 2474–2479, June 2011.

[184] M. J. Polking, M.-G. Han, A. Yourdkhani, V. Petkov, C. F. Kisielowski, V. V. Volkov, Y. Zhu, G. Caruntu, A. Paul Alivisatos, and R. Ramesh, "Ferroelectric order in individual nanometre-scale crystals," *Nature Materials*, vol. 11, pp. 700–709, Aug. 2012.

[185] D. Kan, R. Aso, H. Kurata, and Y. Shimakawa, "Research Update: Interface-engineered oxygen octahedral tilts in perovskite oxide heterostructures," *APL Materials*, vol. 3, p. 062302, June 2015.

[186] T. H. Kim, S. H. Baek, S. M. Yang, Y. S. Kim, B. C. Jeon, D. Lee, J.-S. Chung, C. B. Eom, J.-G. Yoon, and T. W. Noh, "Polarity-dependent kinetics of ferroelectric switching in epitaxial $BiFeO_3$(111) capacitors," *Applied Physics Letters*, vol. 99, p. 012905, July 2011.

[187] N. Balke, M. Gajek, A. K. Tagantsev, L. W. Martin, Y.-H. Chu, R. Ramesh, and S. V. Kalinin, "Direct Observation of Capacitor Switching Using Planar Electrodes," *Advanced Functional Materials*, vol. 20, pp. 3466–3475, Oct. 2010.

[188] Y. S. Kim, J. Y. Jo, D. J. Kim, Y. J. Chang, J. H. Lee, T. W. Noh, T. K. Song, J.-G. Yoon, J.-S. Chung, S. I. Baik, Y.-W. Kim, and C. U. Jung, "Ferroelectric properties of $SrRuO_3/BaTiO_3/SrRuO_3$ ultrathin film capacitors free from passive layers," *Applied Physics Letters*, vol. 88, p. 072909, Feb. 2006.

[189] S. Yamamoto and I. Matsuda, "Time-Resolved Photoelectron Spectroscopies Using Synchrotron Radiation: Past, Present, and Future," *Journal of the Physical Society of Japan*, vol. 82, p. 021003, Jan. 2013.

[190] S. Doniach and M. Sunjic, "Many-electron singularity in X-ray photoemission and X-ray line spectra from metals," *Journal of Physics C: Solid State Physics*, vol. 3, no. 2, p. 285, 1970.

[191] L. J. McGilly, L. Feigl, T. Sluka, P. Yudin, A. K. Tagantsev, and N. Setter, "Velocity Control of 180° Domain Walls in Ferroelectric Thin Films by Electrode Modification," *Nano Letters*, vol. 16, pp. 68–73, Jan. 2016.

[192] N. Barrett, D. M. Gottlob, C. Mathieu, C. Lubin, J. Passicousset, O. Renault, and E. Martinez, "Operando x-ray photoelectron emission microscopy for studying forward and reverse biased silicon p-n junctions," *Review of Scientific Instruments*, vol. 87, p. 053703, May 2016.

Erklärung

Hiermit erkläre ich, dass ich die vorliegende Arbeit selbstständig und ohne fremde Hilfe verfasst habe. Ausser den angegebenen Quellen habe ich keine Hilfsmittel benutzt. Alle wörtlich oder inhaltlich entnommenen Textpassagen oder Abbildungen habe ich in jedem Einzelfall kenntlich gemacht. Dieser Dissertation geht weder ein erfolgloser Promotionsversuch voraus, noch wurde sie in einem weiteren Promotionsverfahren eingereicht. Die Ergebnisse dieser Dissertation sind abgesehen von den angegebenen Publikationen unveröffentlicht.Diese Dissertation strebt den Doktorgrad "Dr. rer. nat." an und wurde von Prof. Dr. C. M. Schneider betreut.

Paris, den 2. September 2016

Sara Gonzalez

Band / Volume 161
Neurons on 3D polymer nanostructures
A. Belu (2018), vii, 135 pp
ISBN: 978-3-95806-296-2

Band / Volume 162
Tailoring and Characterisation of Bioelectronic Interfaces
A. Markov (2018), 75 pp
ISBN: 978-3-95806-298-6

Band / Volume 163
Epitaxy of group IV Si-Ge-Sn alloys for advanced heterostructure light emitters
N. von den Driesch (2018), viii, 149 pp
ISBN: 978-3-95806-300-6

Band / Volume 164
Impact and Regulatory Control of the CGP3 Prophage in *Corynebacterium glutamicum*
E. Pfeifer (2018), IV, 206 pp
ISBN: 978-3-95806-301-3

Band / Volume 165
Establishment of Bacterial Microcompartments in the Industrial Production Strain *Corynebacterium glutamicum*
I. Huber (2018), X, 114, XI-XXXIV pp
ISBN: 978-3-95806-302-0

Band / Volume 166
Current-Induced Magnetization Dynamics in Ferromagnetic Nanowires
M. I. Khan (2018), vi, 138 pp
ISBN: 978-3-95806-308-2

Band / Volume 167
Management of Electrophysiological Data & Metadata
Making complex experiments accessible to yourself and others
L. Zehl (2018), 182 pp
ISBN: 978-3-95806-311-2

Band / Volume 168
Investigation of GeSn as Novel Group IV Semiconductor for Electronic Applications
C. Schulte-Braucks, Christian (2018), xx, 165, XII pp
ISBN: 978-3-95806-312-9

Band / Volume 169
Tailoring the Electronic Properties of Epitaxial Oxide Films via Strain for SAW and Neuromorphic Applications
Y. Dai (2018), VI, 133 pp
ISBN: 978-3-95806-319-8

Band / Volume 170
The electronic structure of transition metal dichalcogenides investigated by angle-resolved photoemission spectroscopy
M. Gehlmann (2018), ii, 108, XVIII pp
ISBN: 978-3-95806-324-2

Band / Volume 171
Control of neuron adhesion by metal nanoparticles
A. Q. Tran (2018), viii, 108 pp
ISBN: 978-3-95806-332-7

Band / Volume 172
Neutron Scattering
Lectures of the JCNS Laboratory Course held at Forschungszentrum Jülich and at the Heinz-Maier-Leibnitz Zentrum Garching
edited by T. Brückel, S. Förster, G. Roth, and R. Zorn (Eds.) (2018),
ca 300 pp
ISBN: 978-3-95806-334-1

Band / Volume 173
Spin scattering of topologically protected electrons at defects
P. Rüßmann (2018), vii, 230 pp
ISBN: 978-3-95806-336-5

Band / Volume 174
Interfacing EuO in confined oxide and metal heterostructures
P. Lömker (2018), vi, 140 pp
ISBN: 978-3-95806-337-2

Band / Volume 175
Operando Chemistry and Electronic Structure of Electrode / Ferroelectric Interfaces
S. Gonzalez (2018), 172 pp
ISBN: 978-3-95806-341-9

Weitere ***Schriften des Verlags im Forschungszentrum Jülich*** unter
http://wwwzb1.fz-juelich.de/verlagextern1/index.asp

Schlüsseltechnologien / Key Technologies
Band / Volume 175
ISBN 978-3-95806-341-9

Mitglied der Helmholtz-Gemeinschaft

JÜLICH
Forschungszentrum